Alma Mater Studiorum – Università di Bologna

DOTTORATO DI RICERCA IN

Meccanica e Scienze Avanzate dell'Ingegneria (DIMSAI)

Ciclo XXXV

Settore Concorsuale: 09/B1

Settore Scientifico Disciplinare: ING-IND/16 TECNOLOGIE E SISTEMI DI LAVORAZIONE

Laser cladding and its potential to reduce particulate matter emissions from the automotive and locomotive sector

Presentata da: **Nashit Ali**

Coordinatore Dottorato

Prof. Lorenzo Donati

Supervisore

Prof. Luca Tomesani

Co-Supervisore

Prof. Lorenzo Donati

Esame finale anno 2023

ABSTRACT

Laser Cladding (LC) is an emerging technology which is used both for coating applications as well as near-net shape fabrication. Despite its significant advantages, such as low dilution and metallurgical bond with the substrate, the technology still faces issues such as process control and repeatability, which restricts the extension to its applications. The following thesis evaluates the laser cladding technology and tests its potential to be applied to reduce particulate matter emissions from the automotive and locomotive sector. The evaluation of LC technology was carried out for the deposition of multi-layer and multi-track coatings. 316L stainless steel coatings were deposited to study the minimisation of the geometric distortions in thin-walled samples. Laser power, as well as scan strategy, were the main variables to achieve this goal. The use of constant power, reduction at successive layers, a control loop control system, and two different scan strategies were studied. The closed-loop control system was found to be practical only when coupled with the correct scan strategy for the deposition of thin walls. Three overlapped layers of aluminium bronze were deposited onto a structural steel pipe for multitrack coatings. The effect of laser power, scan speed and hatch distance on the final geometry of coating were studied independently, and a combined parameter was established to effectively control each geometrical characteristic (clad width, clad height and percentage of dilution). The statistical analysis showed that when given parameters are varied, laser power had a negligible effect on the clad height. In contrast, the width and percentage of dilution were found to depend on all three varied parameters used for this experiment. Aluminium bronze coatings were crack-free, and the microhardness was greater than that of typically used values. LC was then applied to coat commercial GCI brake discs with tool steel. The optical micrography showed that even with preheating, the cracks that originated from the substrate towards the coating were still present. The applicability of LC was tested for brake discs. The commercial brake discs emitted airborne particles whose concentration and size depended on the test conditions used for simulation in the laboratory. From the early reported results, the emissions and wear rate were successfully reduced with tool steel overlayed laser cladded brake disc. The laser cladding applications were extended to reduce ultra-fine PM emissions from rail-wheel contact. Test pins from UIC60 900A rail carbon steels were in contact with three types of test discs surfaces: R7 wheel carbon steel, laser cladding overlayed martensitic stainless steel, and laser cladding overlayed Ni-based- 8% MnS self-lubricating alloy. Test results show about halving of the coefficient of friction, 0.42 to 0.22, and one ten-power lower specific pin and disc wear of discs with self-lubricating overlay compared to standard railway carbon steel contacts. Using stainless-steel overlayed discs also resulted in one ten-power lower specific disc wear, but pin wear is unchanged. Particle emission for the tests with discs with self-lubricating overlay is constant at almost 200 particles/cm^3, while running in distance is needed for the other tests. Almost all generated airborne wear particles were in the sub-100 nm range. The use of LC overlay reduced the number of airborne wear particles in the sub-100 nm range by more than a factor of 10.

(Intentionally left blank)

ACKNOWLEDGEMENTS

Thanks to Almighty God for giving me the strength to complete my PhD and everything.

I extend my wholehearted thanks to everyone who directly or indirectly helped me passionately and sincerely during my PhD journey.

My sincere thanks to my supervisor Prof. Luca Tomesani for his support, guidance, and advice throughout my PhD career. Thank you for patiently listening to me and letting me be affiliated with such a great research group. A special thanks go to my co-supervisor, Prof. Lorenzo Donati, who swiftly handled my requests. Thank you for providing me with the latest and brand-new laptop for my PhD and for your advice on the period abroad.

Profound gratitude to Prof. Alessandro Ascari for sharing his literature collection and the fantastic discussions near the coffee machine and at the lunch table. These discussions proved even more effective than the typical meeting room discussions. I thank Prof. Alessandro Fortunato for his support and advice on compiling the published papers.

I express my special gratitude to Prof. Ulf Olofsson, who allowed me to spend my research period with his research group in Machine Design at KTH Royal Institute of Technology, Stockholm, Sweden. I am grateful for all the contributions of Prof. Senad Dizdar from Halmstad University, Sweden, in formulating the research paper. A special thanks to Dr Minghui Tu and Engr. Mr Lucas Bard from KTH for supporting and guiding me in using the lab equipment and analysing data for the emission tests. Thank you for making me feel welcomed at KTH in every aspect and for giving me office space, the kth email, an access card, the office plant gift, and the opportunity to participate in your innovative and fantastic research.

I want to express my sincere thanks to Engr. Mr. Lorenzo Ceccon and Engr. Ms Giulia Baglieri. Their immense support during my PhD could not be summarised in words. Without the academic support of Lorenzo, I could not have been able to complete the PhD. Thank you very much for everything. I appreciate Nextema Srl and bi-rex: Big Data Innovation & Research Excellence, Bologna (Italy), for allowing me to use their latest equipment.

Finally, but by no means least, I thank my parents and sisters for believing in me and for their support.

TABLE OF CONTENTS

List of Tables

LIST OF FIGURES

List of Abbreviations

AM	Additive Manufacturing
BPP	Beam Parameter Product
CLAMIR	Control for Laser Additive Manufacturing with Infrared Imaging
CMOS	Complementary Metal Oxide Semiconductor
CTE	Coefficient of Thermal Expansion
DED	Direct Energy Deposition
DGI	Dekati Gravimetric Impactor
DOE	Design of Experiment
EHLA	High-Speed Laser Cladding (German Acronym)
ELPI	Electrical Low-Pressure Impactor
GCI	Grey Cast Iron
HPDL	High-Power Diode Laser
LC	Laser Cladding
MMC	Multi-Material Coatings
NE	Non-Exhaust
PID	Proportional-Integral-Derivative Controller
PM	Particulate Matter
SEM	Scanning Electron Microscopy

Chapter 1 - INTRODUCTION

Laser Cladding (LC) is an emerging technology applied for surface coatings and near-net shape manufacturing. The process has seen recent interest in further development due to its added advantages and the cost-effectiveness of the associated technologies. Specific process-associated challenges significantly hinder the technology's exploitation to its full potential.

This chapter introduces the research carried out and includes an introduction to LC technology by establishing aims and objectives for the problem statement devised for the research. The chapter concludes by presenting the thesis structure.

1.1 INTRODUCTION

Additive Manufacturing (AM) is successfully shifting from academic research to industry, and companies are highly interested in becoming part of the new era in manufacturing. AM is becoming more and more cost-effective as the technologies associated with the process are becoming more and more cheaper, and the process is getting much more reliable. For metals, industrialisation for coating applications by Laser Cladding (LC) has already begun, which is thought to be followed by near-net shape printing shortly.

Surface engineering, Volume 5, ASM handbook defines Surface Engineering as "Treatment of the surface and near-surface regions of a material to allow the surface to perform functions that are distinct from those functions demanded from the bulk of the material"[1]. This surface treatment is mainly done for functional purposes such as controlling wear, corrosion, and clearance or for dimensional restoration. Alternatively, these can be applied for economic reasons such as lower maintenance costs, longer component life, or using less-expensive substrates[2]. Various methods for such treatments span a wide range[3]. For instance, the modification of chemistry and properties of the existing surface to a depth of 0.001-1.0 mm is mainly done by implantation and nitriding, whereas weld hard facings and other cladding processes produce typical 1-20 mm thick coatings. Other techniques, such as mechanical bonding and deformation, change the properties without changing the composition. Other deposition processes, including thermal spraying, cold spraying, chemical vapour deposition and physical deposition, are also used for coatings. There is no definitive classification of coating processes in the international scientific community, although several authors have contributed to classifying the different technologies. One such type based on a scheme previously set by D. S. Rickerby and Allan Matthews[4] is shown in Figure 1[5].

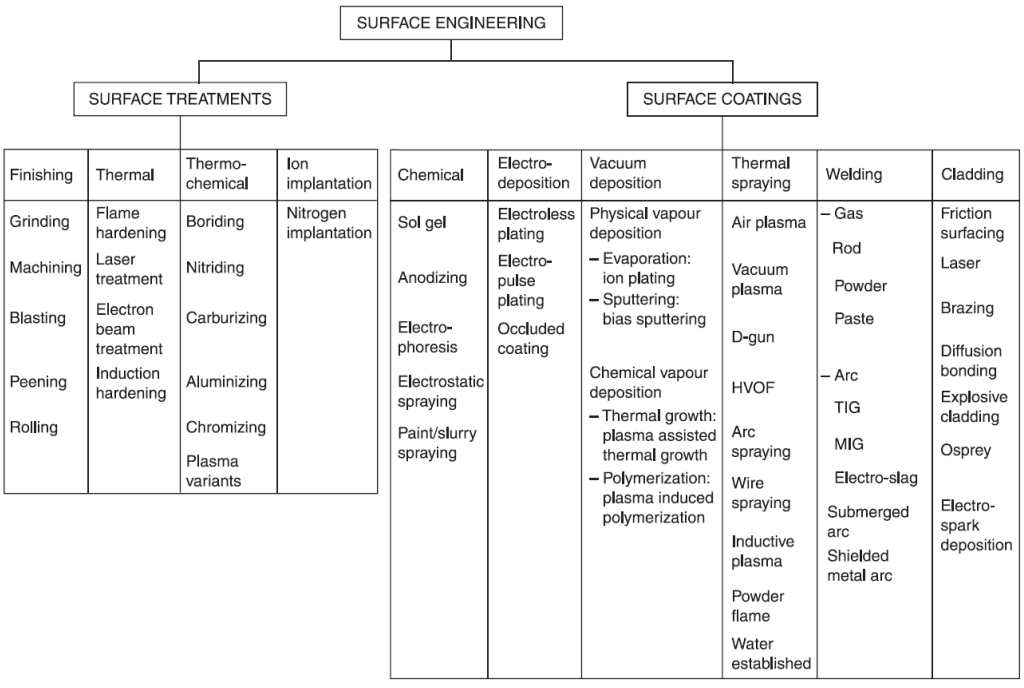

Figure 1 Classification of surface engineering technologies[5]

The proper selection of the coating is based on the component size and accessibility, the corrosive environment, the anticipated temperatures, component distortion and the coating thickness and most importantly, the costs[6].

The surface coating is essential because the lifecycle of engineering parts is mainly affected by wear along with corrosion and fatigue. The combined effect poses a more significant economic impact on the industries. LC has been applied for surface coating mainly for the repair and refurbishment of expensive parts and has proven advantages over conventional technologies, such as low dilution and the establishment of a true metallurgical bond. Due to defects and limitations in traditional techniques, solid-state processing technologies are gaining popularity and are now considered mature and reliable[7].

A high-power laser source melts powder alloys in LC and produces a coating on the processing substrate[8]. The concept of LC is very similar to arc welding[9]. Coaxial LC is one of the most common LC technologies[10] in which a liquid melt pool is created from the laser irradiation on the substrate and results in the formation of a cladding layer as the powder is fed to it via a carrier gas[11]. This results in a metallurgical bond with low dilution[12] with a fine microstructure[13].

LC is an excellent alternative to conventional techniques in surface treatment for metallic materials, especially for improving corrosion and wear resistance. This exception suitability is due to the intrinsic properties of laser radiation: high input energy, low distortion and avoidance of undesirable phase transformations, and the possibility to clad small areas[14]. The former improves quality and offers significant economic benefits[15].

Apart from improving materials' wear and corrosion, LC's potential has also been explored in the context of carbon footprint reduction. Non-Exhaust (NE) emissions from automobiles are one area that is getting substantial industrial interest as exhaust emission controls become stricter. Therefore, it implies that very soon, NE sources (especially brakes) will raise discussions on possible regulatory needs[16]. NE emissions from automobiles mainly include wear of brakes, tyres, road surfaces and resuspension of road dust. This emission contains airborne Particulate Matter (PM), and a growing body of evidence confirms the health hazards of this PM to humans. This PM emission from traffic sources is more significant than other PM emission sources in densely populated areas[17]. Brake wear significantly contributes to NE particulate emission sources, especially PM10 and PM2.5[16]. Braking technology has been through considerable development today; (2022); virtually all cars have a disc braking system. In disk brake, one brake lining presses the brake rotor from the inside and outside[18]. Grey Cast Iron (GCI) is the dominant material for both automotive brake drums and rotors[19]. GCI brake discs are preferred due to their excellent thermal stability and cost effectiveness[20] and will therefore continue to be a favourable material for brake discs in the near future[21].

Underground trains are considered a mode of green transportation. It has become an everyday part of millions of commuters to spend a portion of their time on subway trains. One of the major drawbacks of any underground transport system is that it operates in a confined space that may permit the accumulation

of unhealthy concentrations of airborne contaminants[22]. Therefore, it is essential to maintain excellent air quality in subway environments[23]. At rail subway platforms, extremely small (nanometric to a few microns in size) particle generations occur at the brake-wheel and wheel-rail interfaces that are highly ferruginous[24]. Such wear particles have the potential to be dispersed by air since they will have a terminal velocity slow enough to become airborne[25].

1.2 PROBLEM STATEMENT

Despite the LC coatings exhibiting superiority compared to traditional techniques, they pose difficulties limiting their use. Many drawbacks, such as poor surface finish, have been repressed by controlling and observing the operating parameters. Delamination and crack formation are some other issues that are intrinsic attributes of the process itself and the properties of materials employed[26]. The governing process parameters can be controlled to minimize such defects.

The lack of uniform and reliable properties of the coatings limits the applications of LC. In the case of depositing multi-layers on top of each other, the repetitive melting and remelting give rise to complex microstructures[27], which in turn fail to fabricate parts with desired geometrical aspects. Process monitoring and control have been employed to guarantee repeatability[28]. Much research is needed to study these control processes and to find and set boundaries within which such processes could operative effectively.

The numerous interactions in LC, such as laser beam powder, melt pool/substrate, and laser beam/substrate, along with the physical phenomenon, such as fluid flow and phase transformation, makes it much more complex to control and optimise[29]. Computational[30] and statistical models[31] have been developed to describe the relevant effect of the primary process parameters. Most of the time, the applicability of such models is system dependent as well as on the material or substrate being used. Therefore, more research is needed to cover as many materials as possible with experimental results and analyse them statistically. The combined effect of these parameters on a given geometrical aspect of the clad needs to be developed, which could be used as a reference and may improve the LC process's reliability and repeatability.

Environmental issues directly related to immediate health concerns need to be addressed. This includes the harmful PM emission from the automotive sector. By resolving the issues related to LC, at the same time, its wide range of applicability needs to be exploited further. The NE emissions from automobiles, such as brake discs, are studied concerning decreasing landfills (direct environmental concerns) and reducing PM emissions (direct health concerns). Further research on use of metallic powders that do not contain heavy or harmful metals need to be studied in context of LC.

1.3 APPROACH

In order meet the aforementioned research needs, firstly the effect of closed-loop control system will be studied with additional coupling with scan strategy to build multi-track thin walls from 316L stainless steel. This will create an understanding of the limitations and effectiveness of the melt pool control width type closed-loop control system.

The individual effect of main process parameters will then be studied for multi-track coating of aluminium bronze. Combined parameters will be developed statistically that have the potential to control a specific geometric parameter of the resultant coating. This will add to statistical data for aluminium bronze in the literature as well as act as a point of reference for industrial coatings.

The applicability of LC will be tested by coating tool steel onto a full-scale commercial car brake disc. The limitations and the challenges of coating GCI's will be presented. This will be concluded with applicable processing parameters for such coatings and their limitations.

Laser cladded discs will be then tested for PM emissions for brake disc/Cu-free pins. The rail-wheel contact will be studied in detail to further support the reasoning to apply LC in context of environmental concerns.

1.4 AIMS & OBJECTIVES

The research work aims to evaluate the LC process in detail and further test its applicability to reduce harmful PM emissions from the automotive and locomotive sector. The following objectives were then set out:

- Investigate the effect of scan strategy and closed-loop control system for multi-layer thin wall deposition via LC.
- Investigate the effect of main processing parameters on a multi-track deposition by LC and further statistically develop a combined parameter to control a specific geometric feature of the resultant coating.
- Apply LC to coat a full-scale GCI brake disc.
- Perform PM emission tests for GCI brake discs and LC cladded rail wheel contact and evaluate its possible applicability.

1.5 THESIS STRUCTURE

The thesis is structured according to the aim of the research by providing a detailed evaluation of LC technology followed by its applicability in reducing harmful PM emissions from two types of contacts in the automotive and locomotive sector. The core research of the thesis comes from three published papers with a common conclusion and further research sections.

Chapter 1 introduces LC technology, identifies the problem statement, and provides the aims and objectives of the research.

Chapter 2 contains a thorough review of the literature on LC technology. This includes historical background, principal components, types, processing parameters, geometrical characteristics, monitoring, and defects, followed by recent advancements in LC technology and its main applications.

Chapter 3 introduces all the equipment used to carry out the present research. For clarity, this has been divided into three parts job shop (LC equipment), a machine shop (equipment used for sectioning, preheating etc.) and laboratory equipment (microscopy, equipment for preparation of metallurgical samples etc.). This chapter also details the metallic powders and the substrates used for the experiments.

Chapter 4 and Chapter 5 consist of evaluation studies of LC technology. Chapter 4 discusses the experiment and main findings from the deposition of 316L stainless steel thin-walled features. Scan strategy and melt pool width control effect via a closed-loop control system are discussed. In Chapter 5, the experiment and principal findings from the deposition of aluminium bronze have been discussed. Combined parameters were developed. Statistically, that could control the geometric features of resulting coatings.

Chapter 6 contains the experiment of depositing tool steel on brake discs to further evaluate the subsequent chapter for PM emissions. The results are discussed, including the challenges and limitations of such depositions.

Chapter 7 focuses on LC technology's applicability in reducing harmful PM emissions from the automotive and locomotive sector. Lab experiments were performed to test and confirm the emission of PM from the brake disc / Cu-free pad. PM reduction effects from tool steel overlayed brake discs is presented, and another experiment to study LC's effectiveness in reducing PM emission from rail-wheel contact is discussed.

Chapter 8 draws the main conclusions from all the experiments performed, with a section on possible future work.

Chapter 2 - LITERATURE REVIEW

This chapter provides an in-depth analysis of the development of the LC process. The relevant work of various researchers is discussed. The historical background and principal components of LC technology are described in detail. Different laser sources suitable for LC are discussed, followed by the recent advancement of blue lasers, developed explicitly for LC of highly reflective metals (copper, gold etc.). Two-step and one-step LC are briefly discussed with a detailed description of the 1-step process. The 1-step process is further divided and explained based on feed materials such as wire, powder and strip, followed by hybrid processes. Internal Diameter (ID) cladding is described briefly for coating of internal surfaces. High-speed LC (EHLA) is briefly discussed as a recent development in LC technology. The process parameters and their influence on resulting geometric characteristics are described. An explanation of each process parameter is presented simply. Combined parameters typical in LC to control the resulting coating are described along with the findings and work of previous researchers. The coating defects are essential for monitoring, and adaptive control is detailed. The applications of LC are also discussed in this chapter.

2.1 HISTORY OF LC

LC was introduced within a decade[32] after the invention of the first working laser in the 1960s[33]. In 1971, a patent application[34] was filed that described a method later known as LC. This decade also saw an increase in publications related to LC[35]. Although the LC technology offered significant benefits over conventional hard-facing techniques, its industrial practice has lagged considerably behind other technologies such as laser welding, cutting, heat treating and drilling[36]. Later in the 1980s, some leading automotive and aircraft manufacturers were pioneers in commercialising LC technology. Since then, companies in various industries have started to demonstrate LC on fundamental components[37]. Unsurprisingly, even with this industrial recognition, LC could not keep up with competing for conventional hard-facing methods. The main reason for this low industrial recognition was the lack of development in laser technology, as CO_2 was the only type of laser available at the time. Also, the associated costs to integrate LC were higher than conventional methods. However, this changed in the mid-90s. During this time, near-net shaping was gaining more popularity. This is owed mainly to developing laser technology such as Nd:YAG and diode lasers[38]. Even a book published in 2005 reported a lack of industrialisation of the LC process. The issues, however, were more related to the process control and associated process parameters such as power , scanning velocity and powder feed rate[39]. Once again, this has been changed, and the development of closed-loop control systems now offers suitable measures for overcoming the effects of disturbances in the process. Extremely high-powered diode lasers (45 kW) and growth in high-speed cladding have played a vital role in this decade in the advancement of LC technology. Also, recent advances in lasers, such as blue diode lasers, revolutionised the processing of highly reflective metals such as copper and gold. The demands of wear and corrosion in extreme conditions have forced the industry to accept LC technology. Besides the wear and corrosion resistance, LC has also found its application in reducing environmental pollutants. The environmental impact of traditional technologies such as plasma spraying are well known. LC not only offers promising environmental operation but is now applied to reduce harmful PM emissions in the automobile sector.

2.2 LASERS IN LC

In the LC process, the effect of power density and beam-interaction time plays a vital role[40].

The power density, D, is a measure of the power supplied per unit area and is given by Equation 1:

Equation 1

$$D = \frac{Power}{\pi r^2} = \frac{W}{cm^2}$$

The power density depends on the laser power and the spot diameter.

Beam interaction time is the measure of the time that the laser beam interacts with the piece of base material to be treated and the area of the beam on its surface. It can be determined by the ratio of the velocity of

the laser beam over the material to be treated and the area of the beam on its surface. These two parameters are further interrelated. For example, the sliding velocity of the laser beam will govern the energy received by the piece in case of a constant power density. A very high sliding velocity will result in an insufficient energy transfer since the interaction time will be too small. Interaction time will be more significant in case of low speeds. An increased interaction times can also induce evaporation[41]. Figure 2 shows different laser material processing techniques' power density and interaction time range.

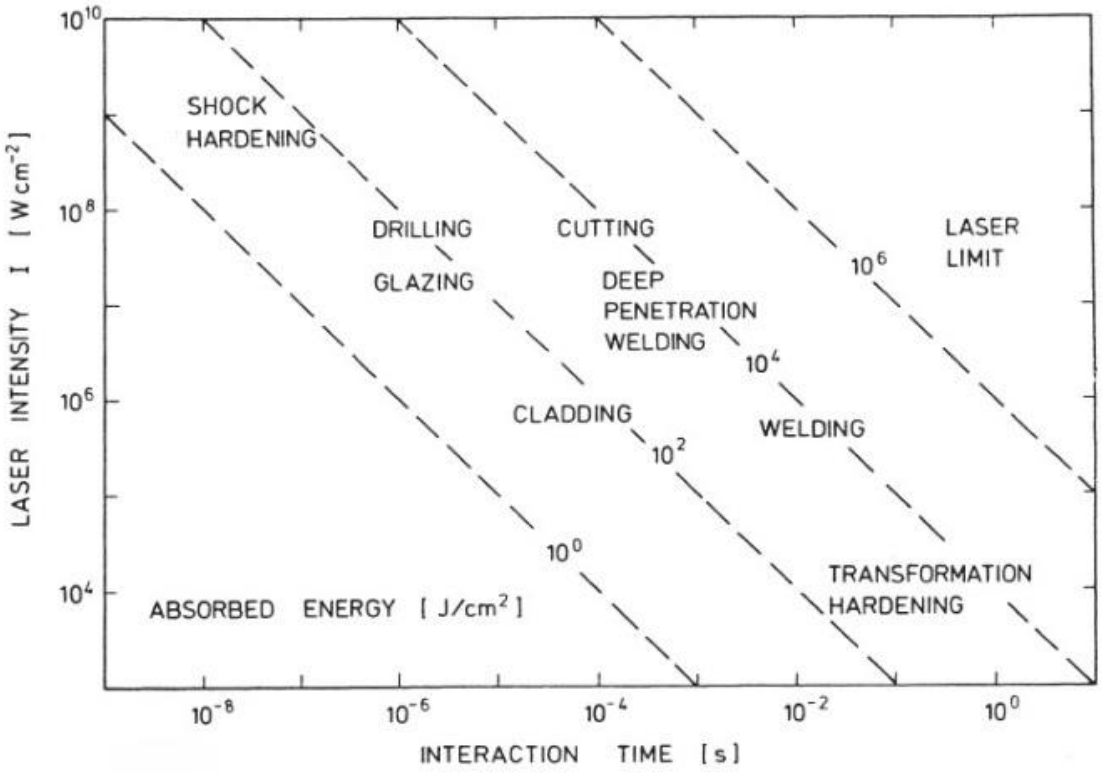

Figure 2 Power density vs Interaction time for different laser material processing[42]

The above figure shows that the LC process requires a power density of 70-100 W/mm² and an interaction time of 0.01-1 second. Thus, a small window of power density is eligible for producing a molten pool in the substrate material for metallurgical bonding with the deposited material. This limits the types of lasers that can be used for LC. The most used lasers in the industry include CO_2, Nd:YAG, diode lasers and diode lasers.

The parameters for these lasers are reported in Table 1.

Table 1 Parameters of suitable lasers for LC[39]

Laser	Wavelength (μm)	Mean power density (W/cm2)	Fiber Coupling	Service life (h)
CO2	10.6	$10^{6...8}$	No	1000 – 2000
Nd:YAG (lamp pumped)	1.06	$10^{5...7}$	Yes	200
Nd:YAG (diode pumped)	1.06	$10^{6...9}$	Yes	5000 – 10000
High Power Diode Laser	0.65 – 0.94	$10^{3...5}$	Yes	5000 – 10000

In laser material processing, absorption and reflection are other vital issues that need careful consideration. The reflection from the metal's surface is a function of laser wavelength, which varies from metal to metal. An absorptivity increase occurs if the process zone's temperature rises during this reflectivity. This indicates the potential for more energy absorption by the material[43]. During multi-material deposition, the change of absorptivity causes a significant difference in energy input combined with locally differing temperature conditions[44]. The laser absorption of different materials is shown in Figure 3.

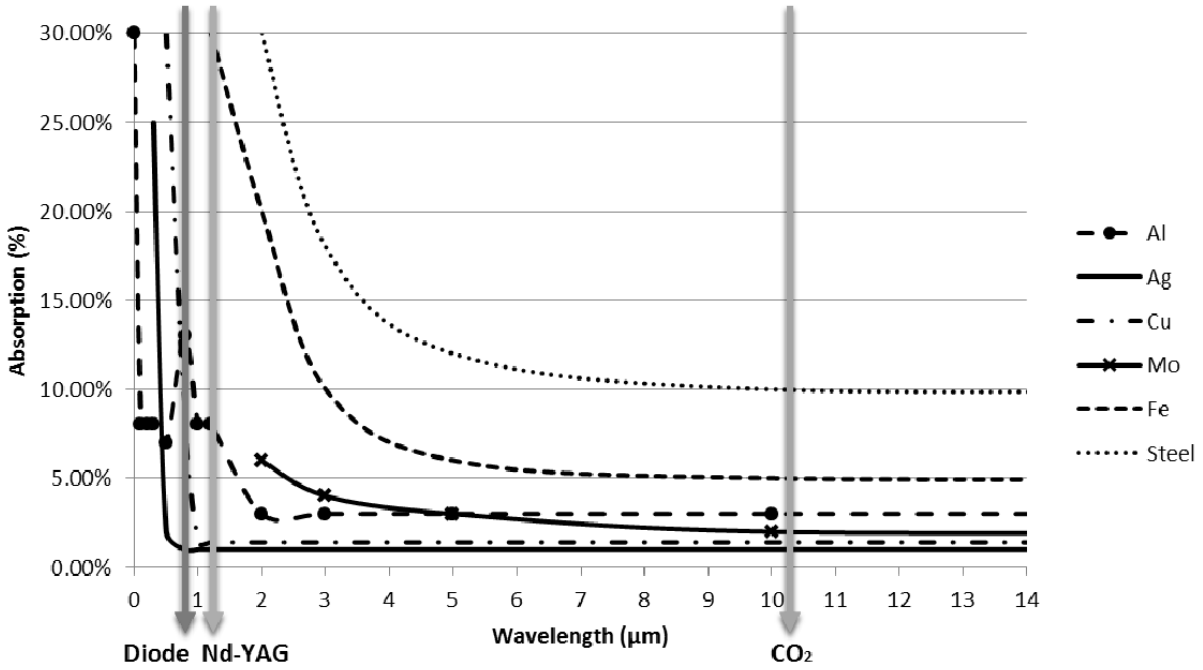

Figure 3 Laser absorption of different materials[39]

The Beam Parameter Product (BPP) is a parameter that is used to quantify the beam quality. It is the product of the beam divergence angle and the beam radius. Lower values of BPP mean higher beam quality. BPP for different types of lasers are presented in Figure 4.

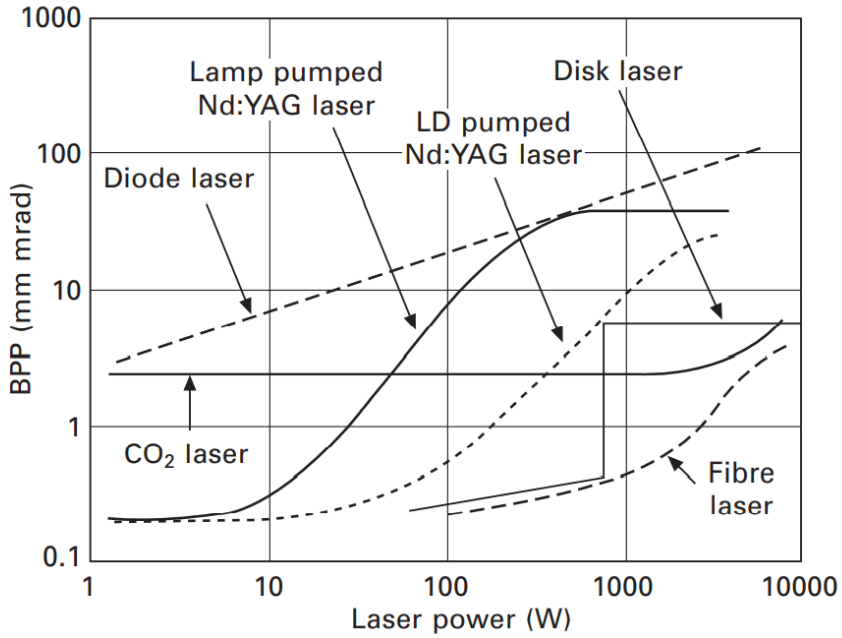

Figure 4 BPP of some lasers as a function of laser output power[45]

In CO_2 lasers, a mixture of carbon dioxide, nitrogen and helium is used as a laser medium. It is excited by direct current or high-frequency alternating current discharge to generate the laser beam. The wavelength of CO_2 laser beams is 10.6 μm. CO_2 lasers first saw development in high outputs, such as 50 kW industrial machines were available by the end of the twentieth century. CO_2 lasers have a high beam quality which decrease relatively in case of high power. High-beam quality CO_2 lasers cannot be delivered via optical fibres. This is due to the long wavelength of these lasers since glass and quartz are opaque to 10.6 μm[45].

Nd:YAG has much shorter wavelengths, usually near-infrared regions ranging from 1.03 – 1.07 μm. Therefore, these types of lasers can be transported with fibre. This gives Nd:YAG lasers a substantial industrial advantage over CO_2-type lasers, as most industrial cladding applications use anthropomorphic robots. The beam quality is also very high, reaching near the diffraction limit. These added qualities increase the price of such lasers, limiting the use of such laser sources to only high-value industries[45].

High-Power Diode Lasers (HPDL) are currently popular among industries and academia for LC applications[46]. The rectangular shape with top-hat intensity distribution makes it an ideal choice for cladding applications requiring ample area coverage[47]. Unlike CO_2 and Nd:YAG, HPDL are of small size and low weight, thus making it possible to build a mobile cladding system[46]. The most recent advancement in laser technologies is the development of fibre lasers[48].

Laser beam characteristics such as BPP, laser beam mode, energy distribution over the spot area, polarisation and focusability play an important role in laser material processing including LC[39]. A homogenous intensity distribution is normally favourable for LC since it results in low dilution of base material and the layer that is welded on to it. For example, the top-hat distribution fuses quite evenly and thus create very little dilution. In contrast Gaussian distribution has its peak in the middle so that the dilution of base material and the next layer would be relatively high (Figure 5)[49].

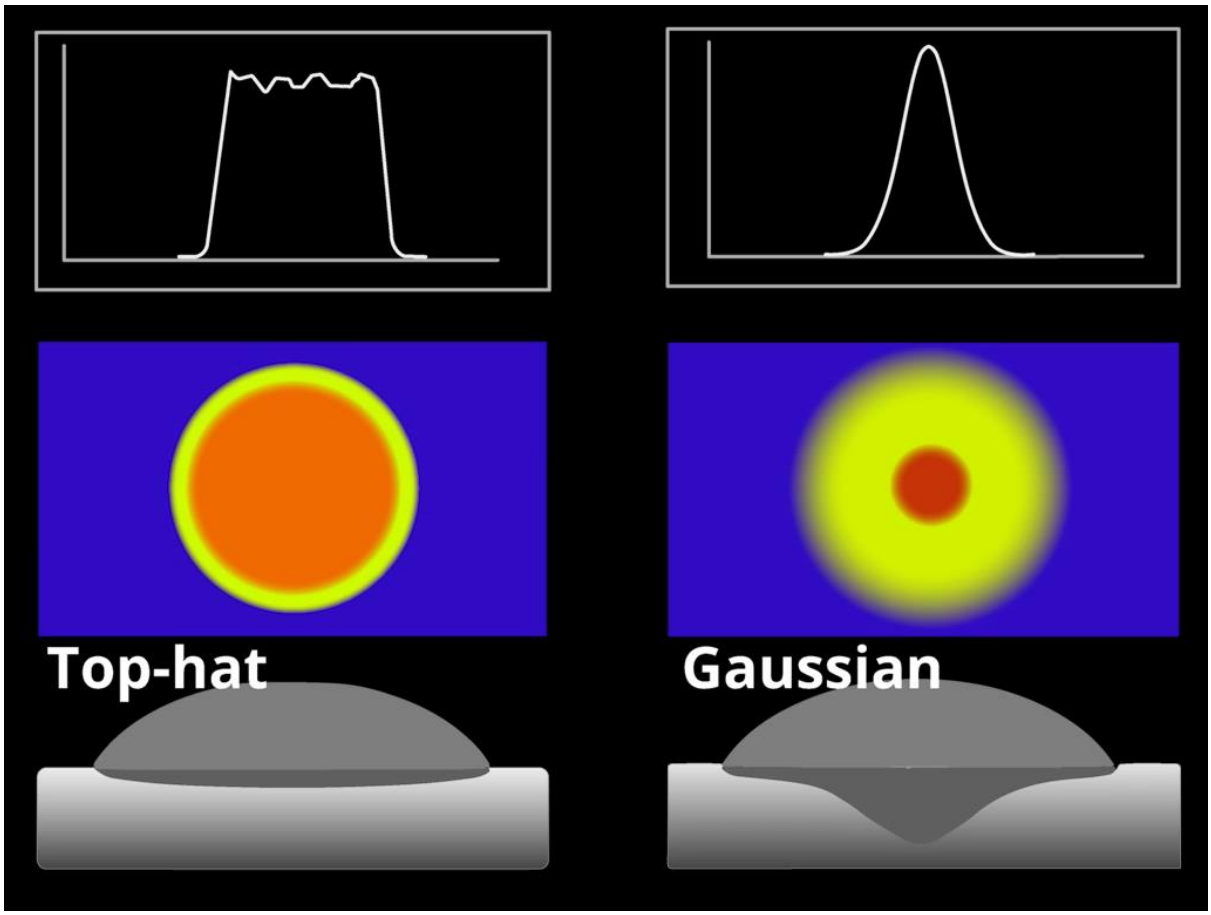

Figure 5 Comparison of two intensity distribution profiles of lasers[49]

Apart from the above, beam delivery is another issue in selecting a suitable laser for LC. For example, CO_2 lasers cannot be transported via fibre optic due to its wavelength and hence this limits the manoeuvrability of motion system along with it[39].

2.2.1 Recent Laser Advancement for LC

Much recent advancement of lasers for LC includes the development of blue lasers for processing non-ferrous metals. Highly reflective metals such as copper and gold absorb the blue light spectrum seven to twenty times better than the laser radiation in the infrared region, as can be seen from Figure 6[50].

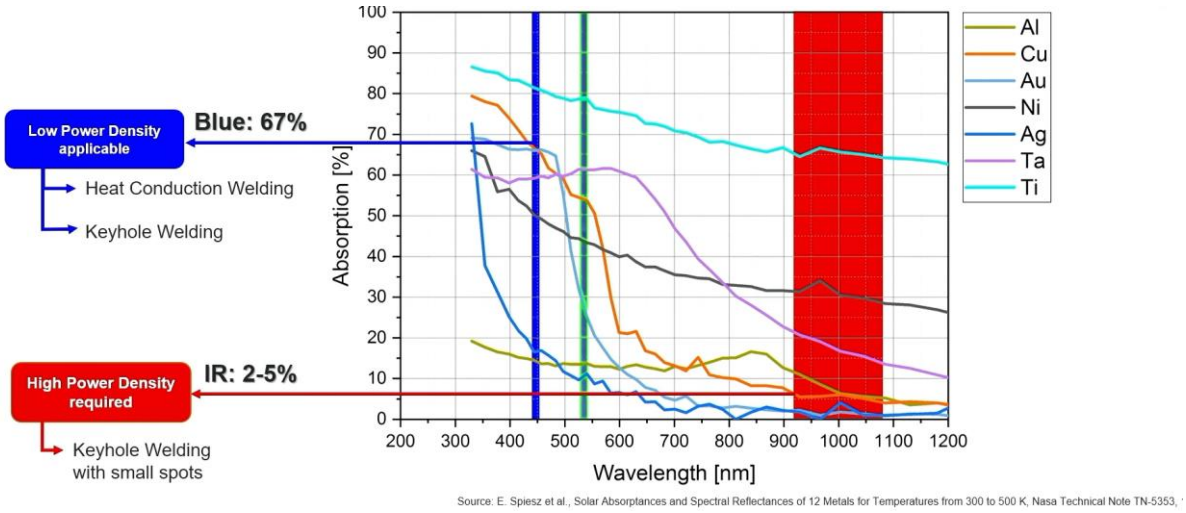

Figure 6 Laser absorption of different materials and blue lasers[50]

Nakaaze et al.[51] developed a fibre-coupled blue direct diode laser with a maximum power of 100 W and a wavelength of 445 nm (laser spot diameters of 580 nm). They used it to coat copper layers on stainless steel. Sengoku et al.[52] used a blue direct diode laser with a spot diameter of 400 μm to deposit a pure copper layer onto stainless steel 304 substrate and studied the temperature distribution by thermal imaging camera and suggested that the dilution of the copper layer can be reduced by cooling the substate. Hara et al.[53] coated a pure copper layer on a pure copper substrate using a multi-bean LC system coupled with a blue diode laser.

Blue diode lasers are available from suppliers with a maximum power of 3000 W and a 445 nm ± 20 nm wavelength.

2.3 TWO-STEP LC

As the name suggests, the two-step LC involves two main steps, i.e., pre-placing the powder onto the substrate and passing the laser beam on the placed powder. Conventional coating methods, such as thermal spraying, electroplating etc., are used for pre-placing the powder onto the substrate. The pre-placing can also be done simply by applying a layer of powder, wire, chip etc. To ensure cohesion between the substrate, the cladding powder to be placed is usually mixed with chemical binders. The melt pool is created when the laser passes over this preplaced powder layer, creating a fusion bonding. Several challenges also arise because of laser passage over the powder bed. The already placed powder is prone to be dispersed by the generation of gasses during melting. Due to this, it is essential to ensure that proper powder cohesion is achieved with the used binder. Furthermore, the cohesion among the powder particles could also be crucial since this can give rise to unnecessary porosity during the evaporation process[54]. The principle of two-step LC is shown in Figure 7.

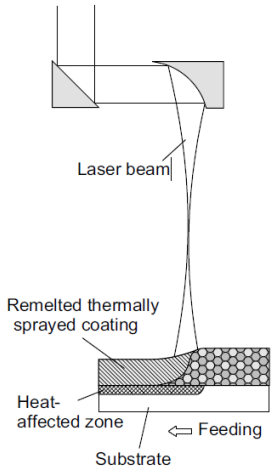

Figure 7 Principle of two-step LC process with previously deposited thermally sprayed coating[55]

The cladding of plasma-sprayed coatings can be technically called remelting. This remelting process may be necessary to improve the properties of plasma-sprayed layers since the microstructures of such coatings exhibit poor interparticle bonding, porosity, and extensive chemical inhomogeneity[56]. However, the laser remelting technique has been practically abandoned due to the improvement of thermal spray coating properties using High-Velocity Oxy-Fuel (HVOF) spraying, especially for hard metal coatings[55].

When the laser interacts with the already placed powder, it generates a melt pool on the surface of the coating material. This melt pool will only propagate to the interface with the substrate upon continued heating. The additional power ensures this continued heating. However, this heat input must be carefully controlled because it can result in severe dilution instead of creating a solid fusion bond. The dilution here means the deep melting of the substrate[57]. This phenomenon has been explained by a physical model developed by Powell[58]. The flow chart of the theory developed by Powell is shown in Figure 8.

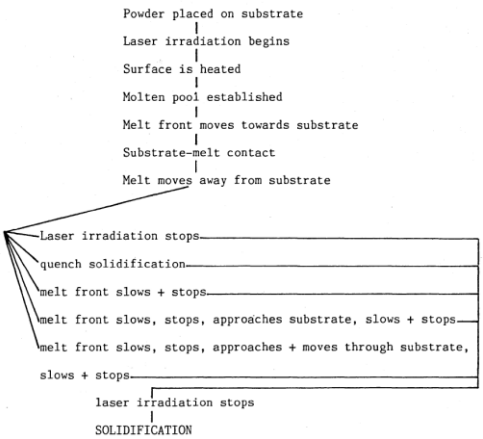

Figure 8 Flow chart of preplaced powder cladding process[58]

Creating several adjacent tracks via two-step LC results in more dilution. Therefore, this process is more common, where parts can be treated via a single-class track. The track where the laser passes over the

preplaced powder leaves behind a molten coating. This molten material then contracts due to the surface tension. This means that the part close to the molten track is no longer covered with the pre-placed powder. This non-covered part of the substrate is directly irradiated by a laser beam, causing deeper melting of the substrate[57]. Figure 9 shows this process.

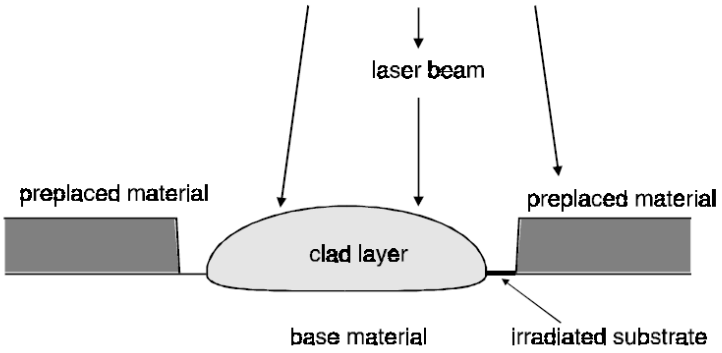

Figure 9 Phenomenon while placing adjacent tracks[57]

2.4 1-STEP LC

The 1-step LC can be described as the simultaneous action among laser-powder-substrate. In this process, the melt pool is generated by laser onto the substrate, and the coating material is fed directly to this melt pool. The laser preheats or melts the powder with a thin layer of substrate, resulting in a lowly diluted layer metallurgically bonded to the substrate. Large areas can be covered by creating several overlapping layers. Due to the nature of the feeding material, this process can also be used to generate three-dimensional structures.

The coating material can be in the form of powder, wire, or strip. The details of each process are presented as follows:

2.4.1 POWDER FEEDING

LC by powder feeding is the most common and preferred technique. The main advantage is the melting sequence of the process[59]. The one-step LC can be further classified based on the nozzle configuration off-axis and coaxial. In the off-axis system, the powder nozzle is positioned at a defined angle, whereas in the co-axial system, the powder nozzle is integrated around the optical system[60].

The off-axis powder feeding was developed mainly for the geometries where the deposition approach is unidirectional such as for coating shafts. This type of feeding is also helpful for cladding grooves and the channel's inner diameter. The nozzles in off-axis powder feeding are axisymmetric and have converging-diverging internal geometry. These nozzles are separated from the laser beam delivery system[61]. The off-axis feeding system is shown in Figure 10. The main drawback of off-axis feeding is its suitability only for 2D applications since the shape consistency of the deposited layer is usually only in one direction when the laser head moves along a straight line or upon the spinning of the substrate[62]. However, multidirectional

off-axis powder feeding can be integrated using a multiple-side feed system as the system developed by Fearon[63], as shown in Figure 11. This setup was designed mainly to control the layer height of deposited layers. The powder catchment efficiency of the off-axis feeding system is somewhat contradictory. Off-axis nozzle in the leading position is reported to be used because of improved powder catchment efficiency. This efficiency can be improved using a higher feeding angle between the horizontal and the nozzle. At the same time, [60] reported from their experiment that the catchment efficiency of the off-axis configuration showed lower performance than the coaxial configuration. The reason for this contradiction could be that the process parameters for the coaxial nozzle are not suitable for off-axis configuration.

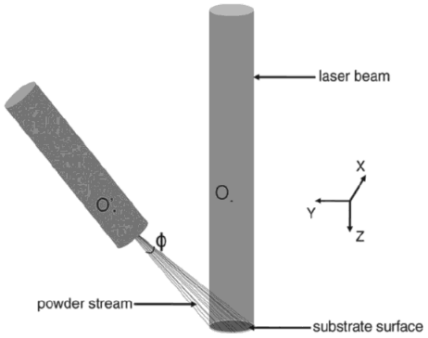

Figure 10 Off-axis blown powder LC[64]

Figure 11 Multidirectional off-axis LC nozzle[63]

A coaxial powder feed system was developed in response to overcoming the omnidirectional limitation of the off-axis feed configuration. Unlike the off-axis system, this system is composed of one nozzle that delivers both laser and powder to the substrate. In this process, the powder is blown out via the carrier gas from the annular zone surrounding the nozzle's central hole, which delivers the laser beam. The powder distribution in coaxial jet flow is Gaussian by experimental and numerical approaches. Inert gas is blown through the inner and outer nozzles that prevent the focusing lens and prevent power oxidation. The schematic of the co-axial nozzle design is shown in Figure 12.

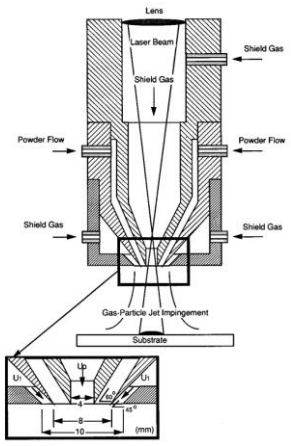

Figure 12 Coaxial nozzle design[65]

These coaxial feed systems have also seen developments where the shape of the powder stream could be adjusted to conform more to that of the laser beam, e.g., for a rectangular-shaped laser spot instead of a circular one. This was done using fixed and radially adjustable gas jets. The coaxial feeding system offers the advantage of more homogenous powder melting before it reaches the melt pool. This results from the effective energy transfer from the laser to the powder as it is dispersed more evenly as it passes through the laser beam[66].

The main drawback of the blown powder technique is its low coating material efficiency which remains its main disadvantage whereas it is reported to be increased by using finer-grade powder. The coating material efficiency refers to the amount of powder material that remains in the melt pool and contributes to coating. For instance, the powder particles that hit the solid surface will be dispersed away whereas the particles that impinge on the liquid surface will contribute to the melt pool surface. The typically recommended size LC is done by PTA grade powder (50 – 150 μm), whereas HVOF (10 – 60 μm) has also been used[67,68]. At the same time, particles could be as finer as 10-20 μm. The powder streams are shaped by the gas stream[69,70], and their diameter strongly depends on the particle size. The resulting screen opacity formed by the powder governs the absorption of photonic energy[71]. Reducing the particle size increased the laser absorption, resulting in better efficiency. This resulted from the dense screen with the appearance of multiple scattering phenomena that absorbed the incident laser beam[72] very efficiently. Due to the technical limits of the powder feeders and nozzles, using finer-grade powder would require modifications. Otherwise, this could cause powder agglomeration and resultant blocking of the nozzles, thus reducing efficiency[73]. The risk of vaporisation also increases with the use of finer-grade powders[74]. Powder material vaporisation is highly undesirable as it reduces the material delivery into the melt pool since it directs a more significant proportion of laser energy towards melting the substrate that would otherwise have been absorbed by the powder, increasing dilution[75]. Furthermore, in the blown powder technique, a high ratio of particles directly bounces off the deposited area by hitting the un-melted surface. This can reduce the efficiency ratio of trapped particles by up to 40%. This issue could partially be resolved by selecting an appropriate inclination angle, as reported in[76]. Carrol et al.[77] showed that the efficiency

could be improved by collecting the unutilised powder during the process and reusing it. The reused powder shown in successive reuse cycles did not show similar properties to the resulting class. The size distribution and composition also showed more significant variation. However, methods are reported for the reconditioning and later reusing of powder materials. Renderos et al.[78] suggested that the best procedure for treating used nickel-based powder involves sieving and separating magnetic phases without performing any other cleaning step. This can reduce the formation of agglomerations and clusters, reducing the risk of ulterior nozzle clogging. These practices involved extra steps and could become counterproductive instead of increasing efficiency. Another major drawback is the emissions that occur during the processing, which could cause more damage to the exposed person. Two primary manufacturing methods for metal powders are used for LC: water atomisation and gas atomisation[79]. Gas-atomised powders are spherical and contain lower oxygen content but are more expensive[80] than water-atomised that are irregular in form[81]. These powders contain alveolar as well as inhalable dust fractions. These emissions are currently not being studied much in literature. One study describes a method to characterise the nanoparticle emission during LC with stainless steel powder[82]. Noskov et al.[83] found that the nanoparticles are suspended in the gas phase closer to the processing surface. The primary pollutants found during manufacturing with powder metal are aggregated core-shell nanoparticles with an average particle size of 10 nm. Moreover, this core consists of iron, chromium and nickle atoms, and the "shell" is a thin oxide layer. The excessive powder also gets settled onto the equipment, such as the robotic arm or the connection tubes and wires. If the equipment is not covered correctly, this could result in losses. Direct Energy Deposition (DED) operations are usually carried out in enclosed cells, and after the processing, these are very challenging to clean.

2.4.2 WIRE FEEDING

Wire feeding, in principle, can be performed similarly to off-axis blown powder cladding. The only main difference is the feed material. The process was first used in the 1990s but failed to get much recognition due to several difficulties in control of the process and poor accuracy[84].

Wire feeding is also mainly characterised based on the melting of wire. In one case, the wire is melted in the form of droplets, and beads are formed on the substrate, which is irregular. In the other method, the wire is fed to the melt pool generated by the laser, resulting in solidification as the laser passes the melt pool[85].

The geometry-related parameters need to be controlled to achieve the desired dimensional accuracy. The stress-induced deformations in wire feeding are still a significant drawback. These cause the loss of dimensional accuracy, especially in large additively manufactured parts. Apart from the process parameters, the deposition pattern and sequences play an essential role in wire-feeding systems[86]. Significantly, the wire feeding location concerning the laser beam is critical since this process is more sensitive to misalignment[87]. The lack of material in the form of wire poses another limitation to the use of this method. Apart from the mentioned drawbacks, wire feeding provides greater material efficiency. Contrarily,

in the powder feed, almost no material is wasted. This also results in a much cleaner process and requires practically minimal post-cleaning.

2.4.3 STRIP FEEDING

The development of high-powered lasers has enabled wide strips as a feedstock material alongside powder and wire[88]. The requirement of high-powdered lasers could be a possible reason that this type of feed has not been studied widely. Yelistratov[89] used a 4-kW direct diode laser to laser-clad narrow (6 mm) strip of Alloy 625 and reported low diluted and uniform-clad deposits with a deposition rate of 1.9 kg/h. In 2004 Malin et al.[90] introduced the repair of military components via strip LC and demonstrated its use in filling pre-machined grooves. Jari Tuominen et al.[88] used a 10 kW high-power diode laser to clad 30 mm wide alloy 625 metal strips on various steel grades. They used a novel LASERstrip head designed specifically for strip LC and reported a deposition rate of 8 kg/h.

2.5 HYBRID LC

In hybrid LC, an additional energy source is utilised along with the laser source. This is done to supply extra energy to the process, which ideally should be more cost-effective and efficient than the energy from the laser source. Depending on the materials under treatment, additional power could be applied to the clad or base material. Combining other energy sources increases productivity and deposition rate[91,92]. An example of such a hybrid system is a combination of a CO_2 laser with a conventional arc machine[93]. Another study in which the core filler wires were heated before entering the melt pool reported that the process energy required to produce coatings was almost halved[94].

Preheating the base material is common and could be called hybrid LC. The efficient method of base material heating utilises induction[95]. Besides decreased laser energy usage during deposition and high deposition rates, it also provides geometric stability to clad layers. In most cases, this kind of procedure is carried out as a necessity. The preheating of substrates is beneficial in obtaining crack-free coatings[96] that result from the high thermal gradients[97].

LC and Plasma Transferred Arc welding, also known as PTA, has been used as a hybrid technology to improve the deposition rate by maintaining minimal heat input to the substrate[98]. Laser-assisted thermal spraying[99] also produced relatively thin and low-diluted layers[100].

Furthermore, a combination of LC and gas nitriding has been performed simultaneously as a hybrid process. The forced and localised cooling by nitrogen vapour stream under cryogenic conditions for WC-Ni powder has shown improved physical and mechanical properties of coatings[101].

2.6 ID CLADDING

In ID cladding, the miniaturised heads with integrated optics and powder feed nozzles are used to clad the inner diameters. These heads are specifically designed to reach the small internal diameters that would otherwise be impossible with other types of cladding procedures as described above. Figure 13 shows the

ID cladding head. An example of ID cladding is the ID deposition of Stellite21 on S235JR in a horizontal welding position with 3.5 kW Nd:YAG laser. This technology found its applications in the generative fabrication of inner 3D structures and repair of local damages in oil drilling tools[102].

These are also known as ID guns in the market. With recent development in these heads, it is now possible to reach internal diameters as small as 25 mm. The length of these heads is limited to 1500 mm, which can cover the interior surfaces of parts up to 3000 mm depth. This can be achieved by rotating the substrate via a roto-tilting table. A wide variety of these ID guns are available, and the dimensions and limits could vary a little depending on the supplier. But, with an increased length typically beyond 1500 mm, the process stability is compromised due to vibrations. One of the significant challenges of using these ID guns is process monitoring. Since it is not possible to integrate cameras in these ID guns, that could provide valuable information about the process. These are also mainly limited to internal diameters.

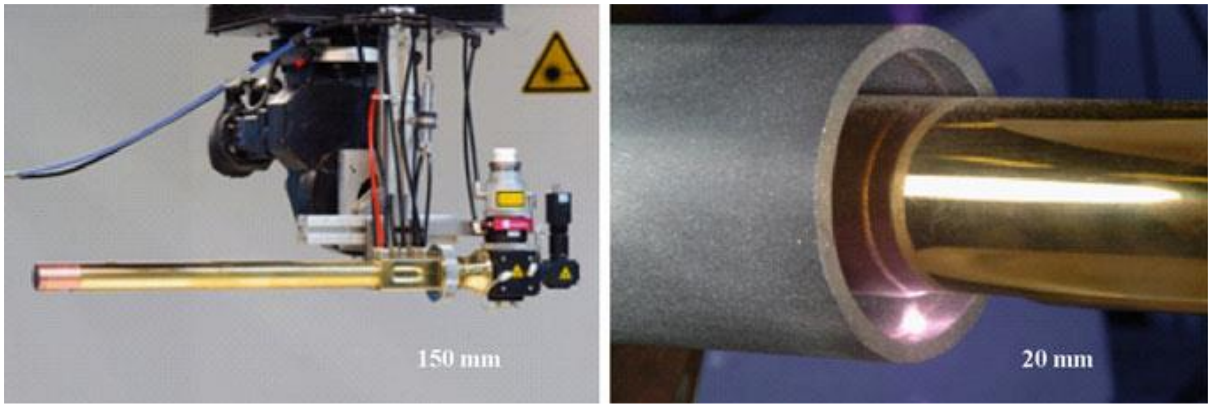

Figure 13 Internal cladding head[103]

2.7 RECENT ADVANCEMENTS IN LC

The LC process has been through many developments, as described in the section above. Recently, there has been an increase in the development of existing LC processes, which are summarised below:

2.7.1 HIGH-SPEED LC

The challenges in LC, such as substrate dilutions and thermal cracks, are associated with conventional LC. To overcome these issues, a variant of 1-step LC (coaxial) is developed by Fraunhofer ILT. It is termed High-Speed LC and is known in the literature by its German acronym EHLA. The typical feed rate of traditional LC is between 0.5 – 2 m/min, whereas EHLA can reach a remarkable 50 – 500 m/min. The layers could be as thin as 25 – 250 µm. Apart from mitigating the associated issues from its parent LC, this technology offers an alternative to hard chrome plating. Since hard chrome plating using chromium (VI) now requires special authorisations, EHLA brings an alternative to this problem. Unlike traditional LC, in EHLA, more than 80 % of the laser energy is absorbed by the powder for melting before reaching the substrate[104]. The schematic representation of the two processes is given in Figure 14. This idea is combined with high speeds, producing a relatively thin layer with low dilution and improved surface

roughness[105]. This occurs due to the reduced heat load to the substrate, further decreasing the nucleation of thermal cracks on the coating/substrate interface.

An example is the deposition of crack-free AISI 4340 onto the E355 substrate by EHLA[106]. The EHLA process has also been studied and tribologically tested for Metal Matrix Composite (MMC)[107]. The increased cooling rate is another advantage of EHLA. An example is the comparative study between traditional LC and EHLA of SS 431 steel on 27SiMn rod showed a reduction in grain size of dendritic microstructure for coatings produced by EHLA[108]. Also, EHLA coatings were found to be relatively higher corrosion resistant[109]. The coaxial nozzle technology is further modified to be used for EHLA. Adjustable powder gas beam caustic for the optimised injection of the powder into the laser beam is used to generate a dense powder gas jet[104].

Models have been developed to test this process's technological limits, such as limits of feed rate track formation[110] and for predicting residual stresses[111].

This process is currently available only for rotationally symmetrical components[112], such as shafts and washers for heavy and offshore industries[113]. It is now under research for its suitability for AM[114].

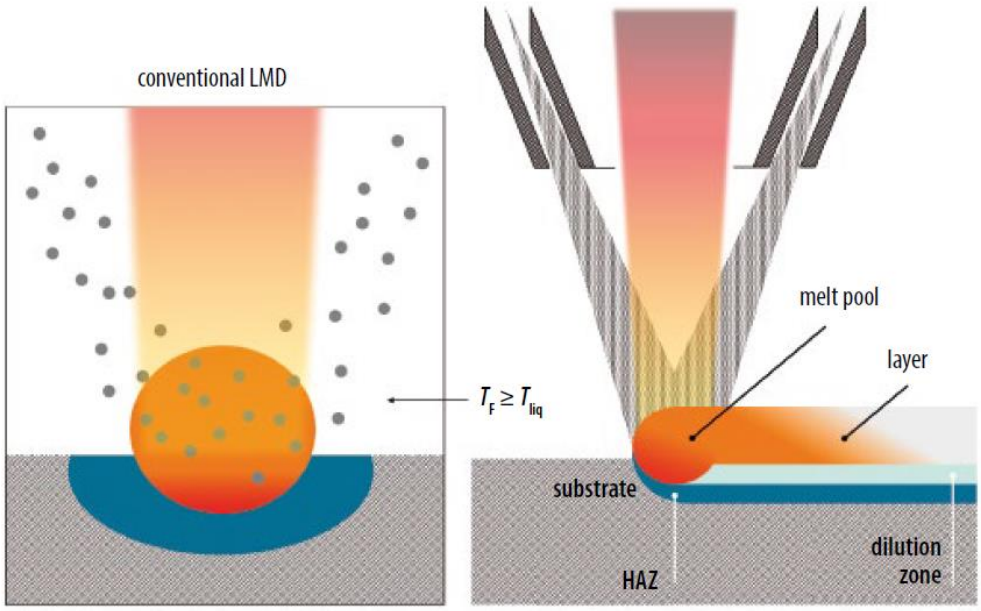

Figure 14 Comparison between traditional laser metal deposition (LMD) and EHLA[115]

The main components of a modern typical 1-step LC system are shown in Figure 15.

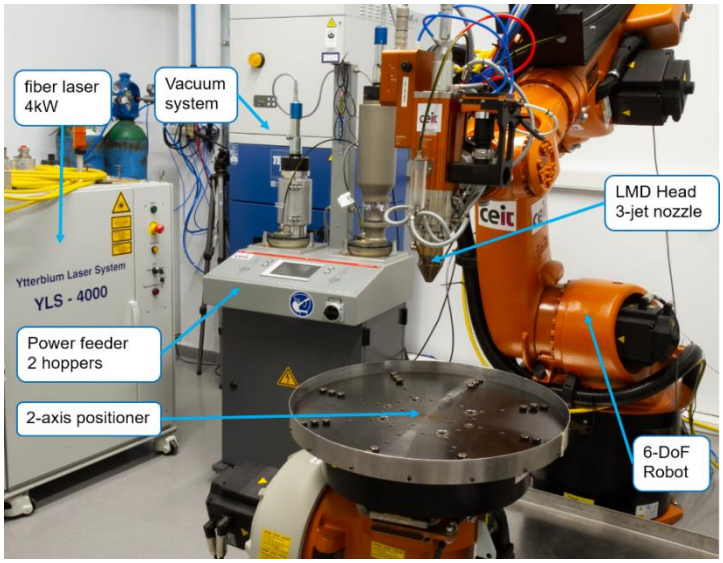

Figure 15 Main components of an LC system[116]

2.8 PROCESS PARAMETERS

The process parameters determine the quality of the coating and are crucial in the LC process. These parameters govern the chemical composition and functional properties of the resulting layer. Process parameters could be classified as variable and fixed parameters. Variable parameters are mainly operating parameters and need to be defined by the user before the start of the process. Fixed parameters are generally the characteristics of the machine and depend on the type of equipment used, such as the laser source, its wavelength, its maximum power etc. The user-controlled parameters could also be termed operating parameters. are shown in the chart. These parameters must be strictly defined before the start of the process and greatly influence the desired outcomes. The performance criterion of the resulting clad can be classified into geometrical, metallurgical, and mechanical characteristics. The operating parameters and performance criterion of the resulting clad are shown in the form of a flow chart in Figure 16.

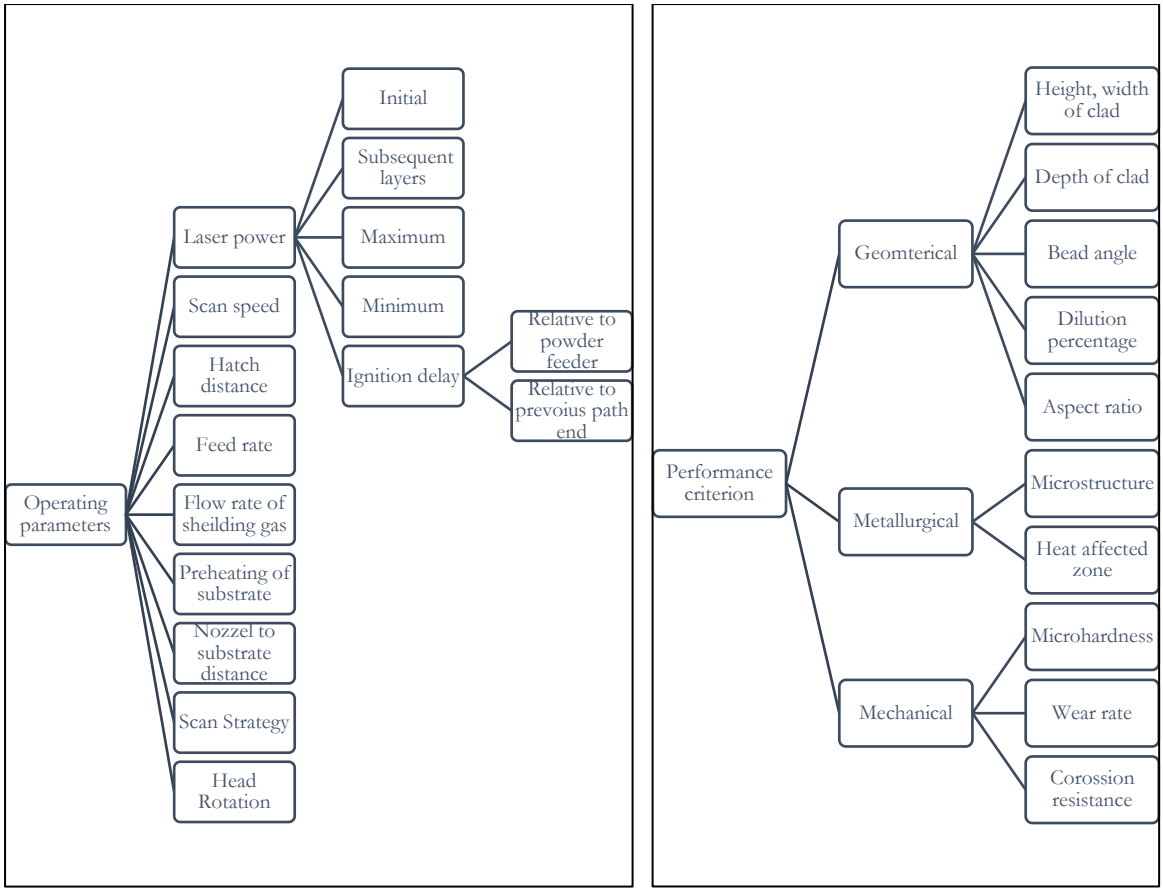

Figure 16 Flow chart of LC process parameters and characteristics of resulting clad

The chart of operating parameters includes some typical terms that are very important for the coaxial blown powder LC process. It is to be noted here that the individual effect of these parameters is presented for initial understanding only. As the process is complex, the parameters have a combined effect. Even if one parameter is changed while keeping all the other parameters constant, it could result in different results. This also depends on many other factors, such as materials and the physical phenomenon involved. The idea is to present a short definition of the terms used.

2.8.1 LASER POWER

This is the amount of energy introduced to the substrate's surface. It governs the amount of filler material that will be melted. An increase in laser power means melting more feed material.

2.8.1.1 Initial Power

It is the power directed at the start of the process. This value is essential when using variable power during the process to avoid excessive temperature.

2.8.1.2 Power at subsequent layers

The power at subsequent layers value is critical for free-form fabrication where several layers are to be deposited. However, in some cases, more than one coating layer is required to achieve the desired thickness. In most cases, the laser power must be reduced to avoid remelting since the temperature of the substrate is already too high.

2.8.1.3 Minimum Power

If the laser power must be reduced during the process, it is necessary to define the minimum power to avoid porosity and, in extreme cases, no melting at all.

2.8.1.4 Maximum Power

Maximum power is the full power and is also to be defined in the case of using variable power during subsequent layers to avoid excessive substrate melting.

2.8.2 IGNITION DELAYS

The feed material (powder) is delivered to the substrate via the carrier gas. When the powder feeder is turned on, there is a delay time for the powder to reach the nozzle. This delay is more significant at the start of the process if the delivery pipes are empty. Therefore, turning the laser on before the powder reaches the substrate could cause undesirable preheating. Since there will be no powder then, the laser will directly point at the substrate for some moments. Ignition delay is significant both during the start of the process and at the end of one laser scan. For example, in the case of linear scans, if the laser must be stopped to deposit the subsequent layer, then the delay between the feed start and laser start should be defined. It is to be noted here that the delay parameter (feed or laser) is decided by the user depending on the desired outcome.

2.8.3 Feed Rate

Feed rate refers to the amount of feed material delivered to the melt pool in time. This is typically controlled by the RPM of discs in the powder feeder and by adjusting the carrier gas flow rate. In modern powder feeders, the carrier gas is mass flow controlled.

2.8.4 Scan Speed

Scan speed is the speed of movement of the cladding head (for 1-step LC). An increased scan speed means less interaction time and therefore leads to lower melting of feed material.

2.8.5 Hatch Distance

Hatch distance is the distance between the centre lines of two successive laser scans. In the case of covering a large area, multiple amounts of beads need to be deposited. Regardless of the beam spot (circular or rectangular), the cross-section of the resulting bead will be a half-ellipse or a segment. Therefore, it is essential to overlap the dots to keep the desired overall thickness. The term "hatch distance" is also known as "step distance" and is often confused with overlapping. Overlapping is the measure of how much one bead interacts with the other. The difference could easily be understood from the schematic shown in Figure 17. Hatch distance along with overlapping controls the thickness and width of coating.

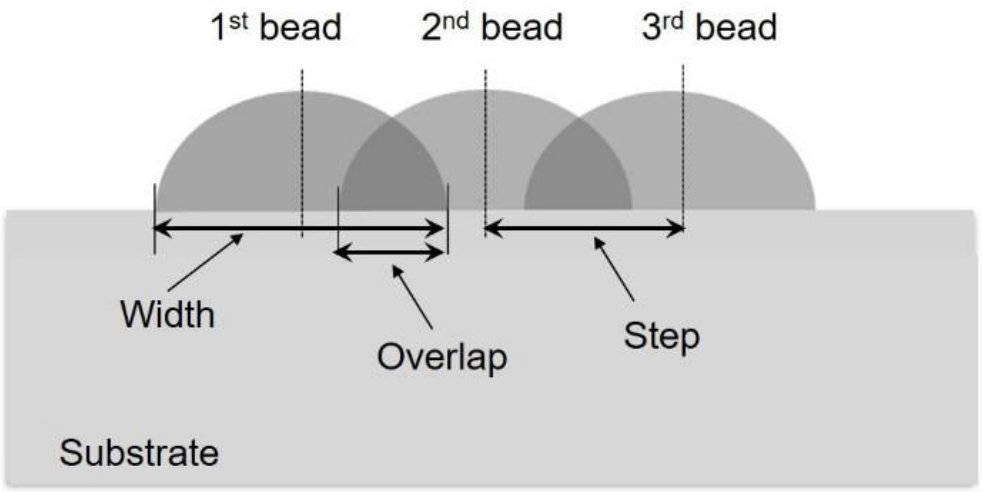

Figure 17 Graphical explanation of step and overlap in LC[117]

2.8.6 Flow Rate of Shielding Gas

The shielding gas prevents oxidation and aids cooling. The flow rate of this gas needs to be adjusted once before the process and is typically kept the same for most operations.

2.8.7 Preheating

Although preheating is performed by induction, it is possible to preheat the substrate by irradiating the laser on the substrate surface.

2.8.8 Layer Increment

The layer increment is the distance the cladding head must cover perpendicular to the substrate in case more than one layer is deposited. This value is also mainly used for freeform 3d fabrication but needs to be also defined for coating applications if more than one layer has to be deposited on top of the subsequent one. There is no standard way to determine the value of layer increment. The only way is by experimenting with different values. Depositing single beads and measuring their thickness could give an initial idea of these values.

2.8.9 Initial nozzle to substrate distance

The laser spot usually governs the distance between the nozzle endpoint and the substrate surface since moving it up and down could defocus the beam. Still, if necessary, these values must be defined before the start of the process.

2.8.10 Scan Strategy

The scan strategy is the path the laser beam must follow to create the coating. This is critical for 3d printing, for example, zigzag, bi-directional and raster etc. This strategy is relatively simple for coating applications, for example, cylindrical substrates. The cylinder rotates, and the cladding head is almost perpendicular to its surface.

2.8.11 Head rotation

The cladding head is not kept perpendicular to the substrate to avoid back reflection that could damage the laser. Therefore, the cladding head is rotated to certain degrees relative to the substrate. This rotation is also critical and could cause variations in the resulting class.

Material-related parameters include the powder and substrate material. The powders for LC are outsourced in most cases, and their properties include particle size, morphology, and chemical composition. The substrate's chemical composition, geometry and mass also govern the operating parameters.

Out of the stated operating parameters, laser power, scan speed and hatch distance are considered the main parameters since these have the most significant effect on the resultant coating. Nonetheless, other parameters such as carrier gas flow rate and shielding gas also considerably impact the final layer.

These parameters have an individual and a combined effect on the resultant coating. The numerous parameters and their mutual interaction make process optimisation quite challenging.

2.9 Influence of operating parameters and performance criterion for Clads

As shown in the chart, the quality of clads is mainly the measure of their geometrical, metallurgical, and mechanical characteristics, which partly depend on the process parameters. A brief discussion related to the

effect of the main operating parameters (laser power, scan speed and feed rate) on the quality of clads is presented below:

2.9.1 GEOMETRICAL CHARACTERISTICS

The schematic of a single bead is shown in Figure 18; the associated characteristics are:

- Clad height (h)
- Clad width (w)
- Clad aspect ratio
- Clad depth (b)
- Clad dilution percentage
- Clad bead angle (θ)

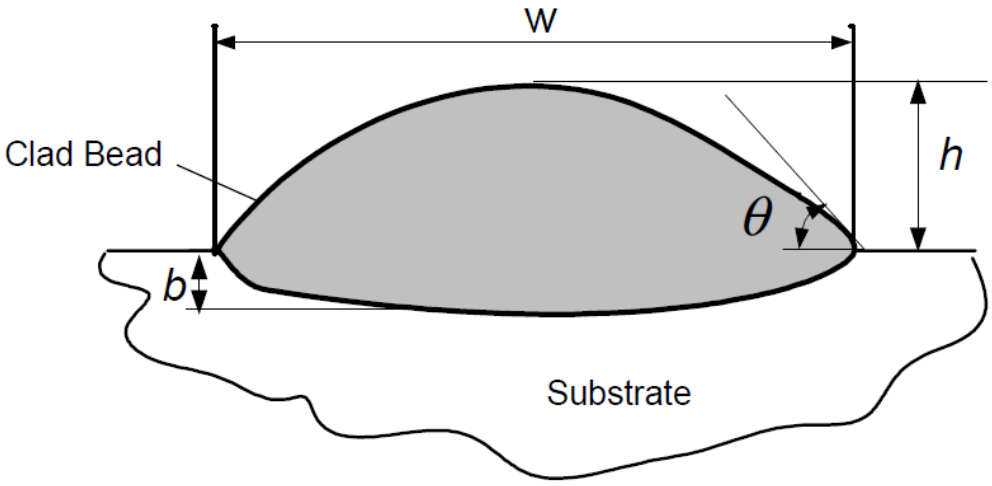

Figure 18 Geometric parameters of laser cladded single bead[39]

2.9.1.1 Clad Height

Clad height, in simple terms, could be described as the thickness of coating above the substrate. This is measured as the maximum distance between the substrate and the clad. Clad height generally increases with an increase in feed rate and therefore has an almost linear relationship with the feed rate[118,119]. Laser power, individually, has a minimal effect on the clad height. This is mainly true when other parameters primarily feed rate, are kept constant, as shown by reference[120]. The impact of laser power becomes more significant when combined with an increase in feed rate, as shown by many studies[121-123]. However, an increased clad height has also been reported while other parameters were kept constant[124,125]. Laser power has also been reported to decrease clad height[126]. Increasing laser power can lead to excessive melting and flow of the deposition track, thereby reducing clad height with power[127] and increasing the scan speed results in reduced height[128]. This is due to the reason that the laser-powder-substrate

interaction time reduces with increasing scan speed. The clad bead geometry mainly depends on the laser beam geometry and operating parameters. A circular laser beam results in a partially spherical clad cross-section. For a circular beam geometry, the single clad beam height can be estimated empirically according to Equation 2[129].

Equation 2

$$H_c = \alpha_c \frac{M}{V}$$

where,

H_c is the single clad beam height, a_c is an experimentally determined parameter, depending on materials and laser power, M is the powder feed rate, and V is the transverse speed.

The overlapped clad thickness for partially spherical single clad beads can be estimated empirically according to Equation 3[129].

Equation 3

$$h_c = -1.8 H_c \ln(i)$$

where,

h_c is the overlapped clad thickness, H_c is the single clad beam height., ln(i) is the logarithmic value of the degree of overlap.

2.9.1.2 Clad Width

The laser's spot size principally governs the initial track width on the substrate, given that the heat flux is sufficient to induce melting, especially in the case of a single bead[127]. For multiple overlaps, the clad width is mainly dependent on hatch distance. For single beads, wider clads can be obtained using low scanning speed and high laser power. Mathematical models and experimental studies have also proved this linear width decrease with transverse speed for multiple-layer structures. The width of multiple layered thin walls increases with an increase in laser power[130]. This occurs mainly due to the transition from three-dimensional to two-dimensional heat flow and has been quantified by three-dimensional process maps[131,132]. The powder mass flow rate has little effect on the clad width. For a circular laser beam geometry, the single-clad beam width can be determined from Equation 4[129].

Equation 4

$$W_c = D(1 - b_c V)$$

W_c is the single-clad beam width, D is the beam spot diameter, b_c is an experimentally determined parameter depending on materials and laser power and V is the transverse speed.

2.9.1.3 Clad Aspect Ratio

The aspect ratio is the ratio between the width and height of clad[39]. The aspect ratio depends mainly on the scan speed and feed rate. The effect of scan speed is more significant than the feed rate, as shown in[133], where the aspect ratio increased with scan speed. This ratio decreased with the mass flow, but the influence was lower than the scan speed. In the case of overlapped tracks, the minimum recommended aspect ratio is 5 to avoid the porosity between the clad tracks[129].

2.9.1.4 Clad depth

The clad depth refers to the amount of substrate that is melted and added to the cladding. It is measured as the maximum linear distance from the interface to the starting point of HAZ.

2.9.1.5 Clad bead angle

The clad bead angle is between the substrate surface and the tangent to the covered surface.

2.10 DILUTION

Dilution is a critical quality index in LC. Dilution is measured as the ratio between the mass of the original substrate or previously deposited tracks to the sum of the combined group of the substrate and the added material[127]. The former method of measuring dilution is mainly based on the dimensional and geometric features of the clad. Dilution can also be estimated by measuring the iron content. Another non-destructive method to measure dilution is using a dual-frequency electromagnetic sensor to measure the changes in the material's reluctance[134].

The dilution amount is a critical factor and may have a detrimental effects on the properties of coatings[135]. A minimum dilution is required to achieve a good metallurgical bond between the substrate and coating, whereas an excessive dilution can affect the properties of the coating negatively. A too-low dilution value indicates an incomplete fusion bond due to insufficient melting of the previous surface, whereas a too-high value can indicate excessive remelting[127].

Injected powder flux governs the amount of dilution. The dilution increases and decreases mass deposition[83] for a lower powder flux. For LC with single-layer cladding tracks, the dilution is independent of laser intensity and transverse speed for specific energy. Specific energy is the ratio between laser power to the product of beam diameter and transverse speed[136].

2.11 COMBINED PARAMETERS:

The complete description of injecting powder into the melt pool in LC is rather complex due to numerous interactions (laser beam/powder, melt pool/substrate, laser beam/substrate etc.) and physical phenomena (fluid flow, phase transformations etc.). However, a couple of primary process parameters can be controlled to achieve the desired results. These include laser power, scan speed, feed rate and hatch distance. Other factors, such as laser spot size, shielding, and carrier gas rate, are also important. Considering these numerous parameters and their mutual interactions, optimisation of the process is still challenging.[137].

Improved computational models have been proposed to describe the relevant effect of these process parameters[30]. These models are not very advantageous since they require high computational costs and highly qualified labour [138]. The combined effect of these parameters on different geometrical aspects of resulting clads has been studied statistically. Such models provide helpful information in narrowing down and selecting process windows at no additional cost. The empirical statistical models correlate the influence of combined processing parameters to the geometrical features of the clads. These models can be utilised for successful coating without the need to analyse the complex interactions of the process. The contributions of various authors in terms of relating the main processing parameters to the geometrical characteristics of co-axial LC are compiled and presented below in Table 2.

Table 2 Empirical statistical relationship of main processing parameters with clad geometric characteristics

Authors	Laser Type	Substrate	Powder	Height	Width	Dilution
Wu et al.[139]	CO2	A3 Steel	Co-based alloy	VF^{-1}	-	-
De Oliveria et al.[137]	Nd:YAG	C45 low-alloyed steel	nickel–chromium-based alloy powder	$V^{-1}F$	$PV^{-1/2}$	$P^{1/2}V^{1/2}F^{1/2}$
Paulo Davim et al.[140]	CO2	100Mn Cr W4-DIN	Diamalloy 2022 – Ni-based	P, V, F	P, FV, F	-
El Cheikh et al.[141]	Fibre Laser	Low carbon steel	316L stainless steel	$P^{1/4}V^{-1}F^{3/4}$	$P^{3/4}V^{-1/4}$	$\ln(P^{4/5}F^{-1/4})$
Sun et al.[142]	Nd:YAG	Ti6Al4V	Ti6Al4V	V, F, PF, P^2	P, V, F, PV, V2	P, F, P^2
Saqib et al.[143]	Not mentioned	Cold-rolled structural steel	P420 Stainless Steel	V, F	P, V	-
Barekat et al.[144]	Nd:YAG	γ-TiAl	Co–Cr–Mo alloy	$V^{-5/4}F$	$PV^{-2/3}$	$P^{2/3}V^{1/2}F^{1/2}$
Ansari et al.[31]	Nd:YAG	Inconel 738	NiCrAlY	$P^2V^{-3/2}F^1$	$P^{3/2}V^{-1/3}$	V^1F^{-1}

Erfanmanesh et al.[145]	Nd:YAG	AISI 321 stainless steel	WC-12Co	$P^{2}V^{-2}F^{1/4}$	$P^{1}V^{-1/2}$	$P^{1/2}V^{2}F^{-1}$
Nabhani et al.[146]	Nd:YAG	Ti6Al4V	Ti6Al4V	$PV^{-1}F^{1/4}$	$PV^{-1/3}$	$VF^{-1/2}$
Bax et al.[147]	Diode laser	S235JR	Inconel 718	VF^{-1}	$PV^{-1/2}$	PF^{-1}
Li et al.[148]	Wave semiconductor laser	Ti/TiBCN composite	7075 aluminium alloy	$P^{1/4}V^{-4/5}F$	$P^{1/3}V^{-1/3}$	$P^{1/8}V^{1/5}F^{-1/2}$
Aghili et al.[149]	Transverse-flow fibre laser	NiCr-chromium carbides	titanium aluminide	$PV^{1}F^{17/20}$	$PV^{-1}F^{-7/10}$	$V^{4/5}F^{-4/5}$
Alizadeh-Sh et al.[150]	Nd:YAG	Inconel 718	A-286 Fe-based superalloy	$P^{2}V^{-2}F^{2}$	$P^{3/2}V^{1}/_{2}F^{-1/2}$	$P^{-1/4}V^{1/2}F^{-1/2}$
Jelvani et al.[151]	Nd:YAG	Inconel 718	Inconel 718 cast superalloy	$P^{2}V^{-1}F^{-1}$	$P^{2}V^{-1/4}$	$V^{1}F^{-1}$
Ali et al.[152]	Diode laser	S235JR pipe	Aluminium bronze	$V^{-1.5}H.D^{-1.1}$	$P^{2/5}V^{1/4}HD^{1}$	$P^{1.1}V^{1.25}HD^{1.2}$

2.12 COATING DEFECTS

The improper selection of processing parameters can lead to coating defects. The coating defects mainly include porosity, cracks, and voids. Excessive dilution and detachment from the base material are also very common[153].

The cracks caused by LC can be divided into brittle and liquation cracks. These brittle cracks are like welding hot cracks and are formed during the cooling stage of the coating when it tries to undergo shrinkage but is prevented by the relatively cooler substrate. Preheating has been known to be an effective solution in preventing the formation of such cracks. The liquation cracks are like welding hot cracks, which are caused due to the difference in melting temperature of phases or impurities present. These usually appear near the fusion zone between the substrate and the coating. Low dilution and high solidification rates can significantly reduce the problem of hot cracking[154,155].

The porosity in the clad layers can be caused due to several reasons which dictate their position of occurrence. These pores and void formations can be divided into inter-track, inter-layer, and intra-layer, as shown in Figure 19.

Figure 19 Porosity in laser cladded layers[127]

The inter-track voids are formed near the base of deposited tracks. They are caused due to incompatible aspect ratios from horizontally aligned tracks[156]. The inter-layer porosity results from a lack of fusion between vertical tracks. Intra-layer is the most common type of porosity and can result from the formation of gas bubbles entrapped into the solidifying melt pool[127]. The spherical shape voids result in the gas evolution or degassing in the melt pool[157] due to the typical chemical reaction between carbon and oxygen that results in carbon dioxide or carbon monoxide gas. If the solidification proceeds in different directions, this results in the enclosed region of the melt pool. Upon solidification, the tensile stresses are generated due to the contraction of such enclosed areas, which could also cause internal porosity. The porosity at clad/substrate region can be due to the poor surface conditions of the substrate, such as grease, impurities at the surface etc. This may affect the surface tension, resulting in a poor bond between the coating material and substrate.

Porosity in coating negatively influences mechanical properties and therefore needs to be eliminated[158]. However, in some instances, porosity can be advantageous, such as in lubricated conditions. The pores then act as pockets for lubricating oil[159].

2.13 RESIDUAL STRESSES

The residual stress arises due to constrained thermal expansion and contraction in LC. Transient thermal gradients cause this due to the track-by-track cooling nature of the process[160]. The hot molten clad layer and the relatively rigid solid substrate, previously deposited layer, or adjacent bead results are the reason for these large thermal gradients. Upon initial cooling, the clad tends to shrink, restricted by the substrate and the adjoining bead, resulting in tensile stress formation[161]. The magnitude of the shrinkage can be estimated by Equation 5[162].

Equation 5

$$\sigma_{th} = E\alpha_{CTE}\Delta t_1$$

where,

σ_{th} = shrinkage or thermal stress (MPa)

E = Young's modulus (GPa)

α_{CTE} = CTE (K^{-1})

ΔT_1 = difference between melting temperature and the base material during processing (K).

The residual stresses are often undesirable from a performance point of view[161]. Residual stresses may result in unforeseen in-service breakdowns depending on their magnitude and type (i.e., whether they are tensile or compressive)[163]. The tensile residual stresses can have a detrimental effect on the effective fatigue[164], corrosion[165] and tensile properties. The compressive residual stresses, on the other hand, are often considered favourable. For instance, increasing compressive residual stresses can improve fatigue resistance[166]. Post-heat treatment has also been applied to induce compressive stress. Since the yield strength of fabricated parts is not isotropic and thus the resulting residual stresses may also vary in x and z directions[167], both tensile and compressive residual stresses are often considered undesirable[168]. The former assumption is mainly applied for near net-shape manufacturing via LC. Therefore, predicting the distribution of these stresses in the deposited structure is essential[168]. The magnitude and direction of these stresses depend on many factors. These can be divided into the material (high elastic modulus and Coefficient of Thermal Expansion (CTE)) and processing parameters (transverse speed, component clamping, pre-heating, and post-treatment). The estimation of tensile residual stresses via CTE is straightforward. For instance, if the CTE of the coating material is larger than the CTE of the substrate, a more significant difference in CTE corresponds to higher tensile stress in the coating layer. A vice versa of CTE values tends to almost dimmish the tensile residual stresses. The shrinkage caused during cooling is counteracted if the solid-state transformation involves volumetric expansion, diminishing the tensile residual stresses[169]. A slower transverse speed showed decreased tensile stresses when the CTE mismatch was not present[162].

By neglecting the deformation of base material and volume changes due to phase transformations Equation 6 can be used to estimate the sign and magnitude of resultant stresses[170]:

Equation 6

$$\sigma = \frac{(CTE_c - CTE_s)(T_2 - T_1)E_c}{1 - v_c}$$

where,

σ = resultant residual stress (MPa)

CTE_c = coefficient of thermal expansion for the coating material.

CTE_s = coefficient of thermal expansion of the substrate.

T_1= room temperature

T_2 = heat treatment temperature

E_c = Youngs Modulus of coating material

v_c = Poisson's number of coating material

Plastic deformation and creep can partially relieve these stresses by post-heat treatment by using high enough temperature for a long enough time to relieve all the stresses as performed by[171]. As seen from the above equation, post-heat treatment cannot be used to fully relieve the tensile residual stresses if the CTE of the coating is greater than the CTE of the substrate. Since the leading cause for residual stresses is the transient thermal gradients, one way to reduce these stresses is to regulate the cooling rate and melt pool size. Hence, adjusting the material (e.g., substrate preheating) and processing parameters could strongly influence residual stresses[132]. Substrate preheating is more effective since it decreases the cooling rates and allows more time for plastic deformation and creep. An increase in preheating temperature resulted in decrease of residual stress[172]. In addition, there are some other general rules for estimating these residual stresses. For example, compressive stress in the direction of growth dominated in the lower part of the wall deposited on a rigid substrate, whereas near the top surface, tensile stresses dominated in the longitudinal direction[173]. These rules, however, are subject to variation depending on the substrate geometry and heat flow patterns[127]. Laser pulse parameters can also influence residual stress fields[174].

2.14 MONITORING AND ADAPTIVE CONTROL

Despite the plethora of advantages over conventional coating techniques, industrial implementations of LC are still limited due to underlying issues about process stability and repeatability. The heat accumulation in LC depends on the size and geometry of the base material. This effect increases when depositing more layers on top of each other, i.e., in the case of near-net-shape metallic printing. The newly deposited layer melts to some extent the already deposited layers if the parameters are kept constant thorough out the process. Even with fewer layers, the corners and edges are still prone to heat accumulation due to limitations in heat conduction. This causes an increase in the temperature and size of the melt pool. In-situ monitoring is thus essential when depositing via LC. This online control of one of the main processing parameters (most commonly laser power) in LC via monitoring melt pool signals is called adaptive control.

Process monitoring has become a hotspot of research to ensure the quality and repeatability of the LC process and mainly involves temperature and geometric signature measurements. Temperature signatures are directly related to the coating quality and are essential for adaptive control. Since LC is a rapid heating and cooling process, the measuring sensors must acquire the data at a much higher rate coupled with higher resolutions. The geometric monitoring is usually done by high-speed cameras and 3-D scanners[28].

Doubenskaia et al.[175] measured a temperature of around 2200°C in LC of stellite on steel with a multi-wavelength pyrometer via Nd:YAG laser having a 0.8 mm spot diameter. Köhler et al.[176] measured the melt pool temperature by ratio pyrometry with 2D-resolved measurement. The temperature of coaxial LC of alloyed steels with the cobalt-based superalloy Stellite 21 was around 1800°C. Thawari et al.[177] reported a melt pool temperature of 1700°C generated at the melt pool with a non-contact k-type pyrometer for multi-layer coaxial LC of Stellite 6 on SS316 substrate. Bi et al.[178] used a germanium photodiode with an operating wavelength of 1200 – 1600 mm integrated coaxially to the laser beam in a coaxial cladding nozzle. Laser power significantly influences melt pool temperature more than scanning speed while depositing iron-based martensitic stainless-steel METCO 42C on mild carbon steel C45. Salehi et al.[179] developed a LabVIEW-based Proportional–Integral–Derivative controller (PID) controller with a 2-colour pyrometer and used it to monitor and control the melt pool temperature. Temperature control was not much of a feasible method to produce quality coatings. However, the relative quality was better than the runaway process and suggested that the melt pool should be controlled by controlling scanning speed and laser power. Due to slow response time, the mass feed rate control might not be able to influence the melt pool size in real-time. However, in another study, the brightness temperature varied non-monotonously in short intervals by increasing the powder feeding rate[180]. Song et al.[181] used a dual-colour pyrometer to monitor the melt pool temperature while depositing H13 tool steel on a substrate with an uneven surface. A dSPACE controller was used to sample the melt pool temperature from the pyrometer and to control the laser power through the laser's analogue control interface. The closed-loop system could track the melt pool temperature to a reference temperature profile by adjusting the diode power. Smurov et al.[182] used a bi-dimensional monochromatic and single-spot pyrometer and found a maximum brightness temperature of 1850 °C and 1727 °C respectively, while depositing Ti-based superalloy Ti6Al4V powder on an S235 steel substrate. The variations in measuring wavelengths account for the disparity. The increased laser power increased the measured brightness temperature, whereas an inverse relationship was found between scan speed and brightness temperature. However, the surface temperature with laser power varied with non-linear variation and was confirmed by both pyrometers. Similar trends were found by Pavlov et al.[180] that used a multi-wavelength pyrometer and the infrared camera for co-axial powder injection LC of MMC material (steel 16NCD13 (14NiCrMo13-4) and titanium carbide) on cast iron substrate S235.

Another approach involves the measuring of melt pool width by cameras. Hofman et al.[183] used a Complementary Metal Oxide Semiconductor (CMOS) camera and software algorithms to measure the width of the melt pool. The width of the melt pool was controlled at a defined reference value by the feedback control of laser power. Coldron et al.[184] monitored the melt pool behaviour using a CMOS camera in a coaxial arrangement with the laser beam in the LC process. High-speed camera videos have investigated the melt pool dynamics in several aspects. Gasser[185] used a high-speed camera to look at the TiC particles added to Stellite powder. Due to their high melting point at 3170 °C, these remained undissolved in the melt pool and served as tracer particles. De Baere et al.[186] observed high-frequency dynamics caused by powder particle injection in LC using halogen lamps for illumination and a bandpass

filter attached to a high-speed camera. Wirth et al.[187] used a high-speed camera to observe melt pool surface behaviour during LC at a frame rate of up to 67000 frames per second. Great randomness in the direction of particle flow was observed. Certain flow tendencies could be explained by surface tension phenomena such as the Marangoni effect and its dependence on the process parameters.

Many authors have used highly saturated melt pool images and emissivity values to calculate melt pool dimensions in the LC process[183,188-190]. Various methods of capturing camera images are used to calculate the melt pool dimensions. For instance, Colodron[184] used an emissivity-based algorithm to calculate melt pool width. Araujo et al.[188] used an elliptical approximation. The flaws in emissivity-based image processing algorithms were addressed by Sampson et al.[191], and a new image processing technique is developed that measures the melt pool edges in an improved manner. Machine vision technology enhances images in melt pool monitoring systems in the DED system. The technique performed melt pool measurements independent of emissivity values.

2.15 APPLICATIONS OF LC

LC's main applications are in the automotive, medical, and manufacturing industries. This includes refurbishment and repairing components involving shafts, turbines, and drilling tools. The process further extends to prototyping with the repetition of the operation. These possibilities are due to LC's technological advantages, including but not limited to proper bonding, low heat input and dilution. LC finds its application where material degradation occurs from extreme abrasion and corrosion, such as for the repair of construction equipment, agricultural equipment, hot extrusion dies, oil rig components, aerospace components, and marine components[192].

The generic LC applications are listed in Table 3:

Table 3 Applications of LC

Metals	Refurbishment of continuous casting rolls Bearing journals Mandrils, other plant infrastructure
Automotive	Cylinders The surfacing of automotive and diesel valves Repair of moulds Driveshafts
Mining and Drilling	Hard facing of valves, valve seats Refurbishment of crushers Hard banding of drill rods, Shafts, pumps General mining equipment
Aerospace	Repair of high-value components, such as turbine housings

Power generation	Steam turbine blades Gas turbine blades Hydraulic cylinders on oil rigs Turbine casings Plant and infrastructure
Petro-chemical	Plant and infrastructure Wear plates Valves and pump shafts Turbine components
Transport	Refurbishment of the running surfaces of axles, crankshafts LC of wheels to restore the wheel profiles Exhauster Cap Refurbishment High-temperature corrosion protection of exhaust valves with LC for low-speed two-stroke diesel engines used for ship propulsion LC of boiler tubes in ship engines Repair of high-wear components on dock-side cranes Refurbishment of worn propeller shafts
Paper and pulp	Rollers Crushers Pump shafts, impellors

Fishinan et al.[193] studied the LC and alloying for refurbishing worn machine parts Kazadi P et al.[194] refurbished steel mill components, including distance sleeves, foot rolls, descaler cassette and idler rolls. Denney and Lowry[195] successfully refurbished the catapult trough covers' LC. Chen and Xue[196] used LC of Crucible Particle Metallurgy tool steel on hardened HI 3 Hot-Work tool steel for automotive tooling applications. Tormis et al.[197,198] further devised a method for an innovative solution for shipboard crankshaft in-situ repairs. Gorunov[199] evaluated the possibility of refurbishing titanium turbine blades by LC. Chen et al.[200] used LC to repair IN738 turbine blades. Meinert and Bergan[201] repaired manufactured representing observed damage in aluminium alloys 6061-T6 and 7075-T651 components. Aditya et al.[202] found that Aermet-100 alloy can be used for refurbishment of high tensile steel such as AISI4340 steels by using LC. Liu et al.[203] studied the potential of LC for repairing damaged aircraft components such as 7xxx series aluminium alloy components. Thivillon et al.[204] studied the potential of near-net shaping via LC for manufacturing thick, functionally graded coatings and parts for reactor components. Wang and Xue[205] performed LC of functional coating for biomedical applications. LC has been evaluated in many studies for repair and maintenance of rails[206-216] as well as for reduction in PM emissions from GCI brake discs[217,218]. The comparison of various surface engineering technologies is given in the Table 4[192].

Table 4 Comparison of different surface engineering technologies with LC

Feature	Conventional Welding	Thermal Spraying	LC
Price	Low	Low	High
Consumables	High	Low	Low
Process Control	Low	Low	High
Quality	Low	High	High
Heat Input	High	Low	Low
Heat Affected Zone	Big	Small	Small
Deposition Rate	High	Very low	Low
Coating Thickness	High	Low	Medium
Porosity	Medium	High	Low
Bonding	Metallurgical	Mechanical	Metallurgical
Impact Resistance	High	Poor	High
Fatigue Resistance	High	Poor	High
Distortion	High	Low	Low
Dilution	High	Low	Low
Materials	Limited	Wide	Wide

2.15.1 SUITABILITY OF LC FOR PM EMISSION REDUCTION

The benefits of LC (metallurgical bonding, minimal heat input, to name a few) over the traditional technologies (thermal spraying, conventional welding etc.), as discussed above, make it partially the most suitable application for coatings. GCI brake discs offer reliable performance at an adequate cost and have been state-of-the-art in the automotive industry for a long time[219]. Apart from being prone to corrosion in harsh environments[220], the PM emissions from such discs have recently become a hot topic for the industry. Such emissions pose a significant threat to human health. The exhaust emissions from automobiles are well regulated worldwide, which was not true for the NE emissions until recently (November 2022) when the EU proposed Euro 7 Emissions Standard. Euro 7 standards are the first worldwide emissions standards that move beyond exhaust pipe emissions and set additional limits for PM emissions from brakes. These rules are set to be implemented for all vehicles, including electric ones[221]. The former accelerated the already-started efforts to reduce PM emissions from the brake discs. It, therefore, has become vital to reduce airborne emissions from GCI brake discs. A way to achieve that is coating and overlay welding of GCI brake discs[222]. LC has already found its applicability in various applications (as presented Table 3). With the recent advancements in LC, such as EHLA, improved process monitoring and repeatability, to name a few, this has been extended further. Wear debris created during operation contributes to airborne emissions from the brake discs[223]. Various surface treatment and coating technologies provide wear and corrosion protective functions. Gaseous Ferritic Nitro Carburising (FNC) can provide limited wear and corrosion protective function. Still, mass production would require large batch furnaces that will process thousands of disks simultaneously within two to four hours of production time[224]. Physical Vapour Deposition (PVD) coatings were tried but did not significantly improve the performance[225]. The high

investment costs and long production times of PVD coatings would result in very high costs of accordingly coated brake discs. Electroless and electroplating of GCI are also complicated due to the presence of graphite at the surface, and only after a long processing time, homogenous plating thickness will be achieved. Hard chrome platings have been used widely for wear and corrosion protection, but due to carcinogenic hexavalent chromium's involvement, the electroplating process has been replaced due to health concerns. Therefore, thermal spray and LC of GCI permit coating deposition on individual workpieces at high deposition rates and in accordingly short time. The former technologies make the integration into production lines easy, and advantageous production costs can be reached. Since thermal spray coating is not fused or sealed, the local penetration by corrosive media due to the evolution or presence of channels cannot be avoided.

On the other hand, LC ensures a metallurgical bond, but all the thermally sprayed powders cannot directly be coated via LC without avoiding cracks. The limitations are needed to be considered depending on the chosen coating method. It is also possible to coat a corrosion protective layer via LC that could later be thermally sprayed[226]. Although LC has been there for a long time, its applicability for coating GCI brake discs is relatively new and considerable efforts need to be made, especially in terms of making it reliable in terms of production times, cost and reliability. Various companies have already chosen LC's high-quality corrosion protection and wear-resistant coating. The throughput rate of LC has been considerably improved. An example is the latest laser coating machine from NAGEL MASCHINEN-UND WERKZEUGFABRIK GmbH, which claims to allow workpiece changeover times of less than two seconds. This allows the uninterrupted powder flow, which is fundamentally sensitive to pressure fluctuation and acceleration. The coating and grinding are performed from a single source[227]. The market is catching up with recent developments of grinding machines designed explicitly for hard-coated brake disc rotors[228]. Another hybrid process that is recently introduced (April 2023) also allows simultaneous coating and finishing and is capable to be applied to coating of brake discs[229]. Companies have already started to provide tailored LC solutions for coating brake discs. This has enabled LC to move from niche markets (due to high production costs) to new and improved product solutions that are easily capable of high-volume production and, further, more economical. The application of the buffer layer and the main coatings with a cycle time of 4-6 minutes, with a quantity of about 100,000 pieces per system, can be reached, making it suitable for the masses (LASERLINE). Therefore, this makes LC an expensive alternative for thermally sprayed coatings because their preparation and post-processing are very complex[49].

LC is commonly performed in LC workshops under controlled environment conditions, necessary precautions, and safety measures such as compulsory eye-protection glasses. For open-air applications such as railway and tram rails, in-situ LC with mobile laser systems, e.g., LASERLINE LDF series – Mobile High Power Diode Laser[230], has been practised with promising results[231]. The LC operators use fences – a well-known welders' measure to protect the melt pool from wind and achieve eye-protection of people and animals from fences from the welding arc light/laser light. However, for the applicability of LC in terms of

PM emissions, the R7 wheels were proposed to be cladded. As discussed above, the improved throughput rate applies to coating using LC for this application.

Chapter 3 - EXPERIMENTAL EQUIPMENT AND MATERIALS

Coaxial LC was used to carry out the coatings on the metallic substrates. This chapter introduces the equipment and the materials used to carry out the experimentations. The equipment is divided into Job Shop, Machine Shop and Lab equipment. Images of the equipment, model numbers, and other details are provided where possible.

The job shop section details the LC equipment, such as laser source, powder feeder, carrier gas, shielding gas, nozzle, chillers, closed-loop control system and the main workstation. The output laser power curves and curves created for the flow rate of the powder feeder are also discussed.

The pre-heating furnace, EBM cutting machine, abrasive saw etc., are detailed in the machine shop section.

The lab equipment includes the SEM, optical microscopy, microhardness test machine, and weighing scales used for the samples.

The emission test equipment is discussed in detail. This includes the working principle of the dedicated pin-on-disc tribometer and the particle counter instrument.

The chemical composition, size distribution, density, and flow properties of all the metallic powders used during this study are also described in this chapter.

3.1 LC Equipment (Job shop)

3.1.1 LASER SOURCE

A 3 KW "LASERLINE" Diode Laser (Figure 20) was used (wavelength 980 nm) and 1 mm fibre for transportation of beam to the cladding head. The laser spot diameter was 2 mm onto the substrate surface with a head standoff distance of 25 mm.

Figure 20 Diode 3 kW laser used for LC in present experiments

The laser power measurement was performed by the supplier via Gentec Laser Power Meters. There was a slight difference in the power indicated by the laser and the measurement by the laser power meter. The graph in Figure 21 shows the output power recorded by Gentec Laser Power Meter to the power displayed by the laser source.

The laser beam profiling data from CinCam CMOS Nano 1.001 is given in Figure 22. The measured data for beam profiling is shown below:
Beam Parameter (mm)

Width X: 2.23 mm (50 % of the peak)

Width Y: 2.24 mm (50 % of the peak)

Working Distance: 212 mm

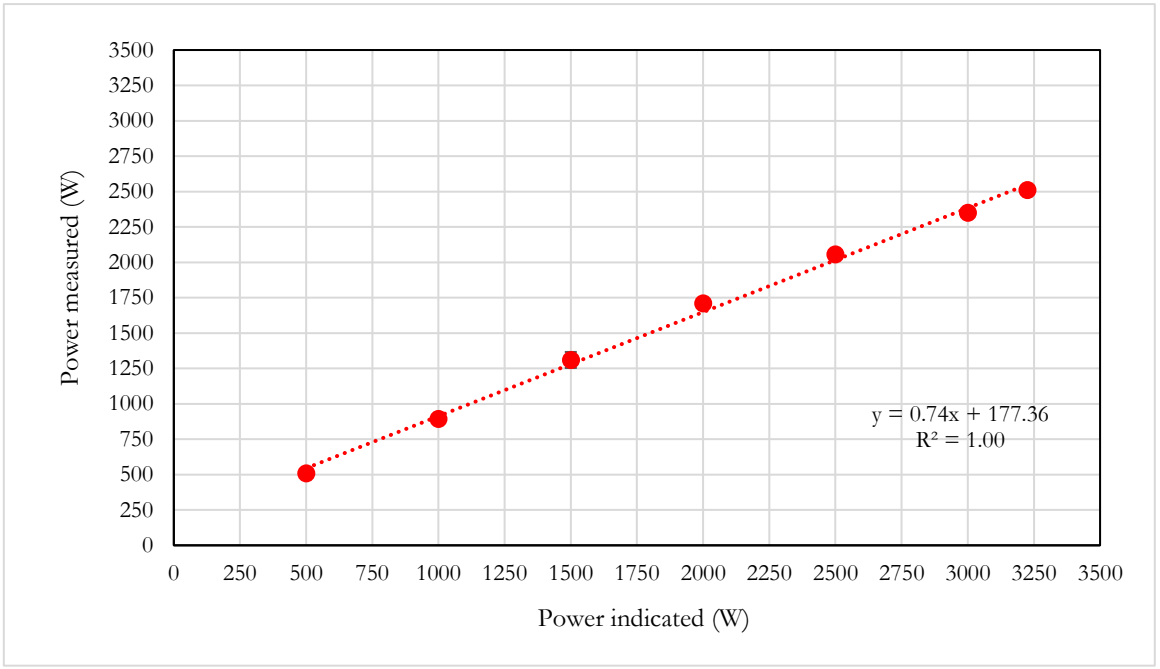

Figure 21 Laser power measured vs indicated

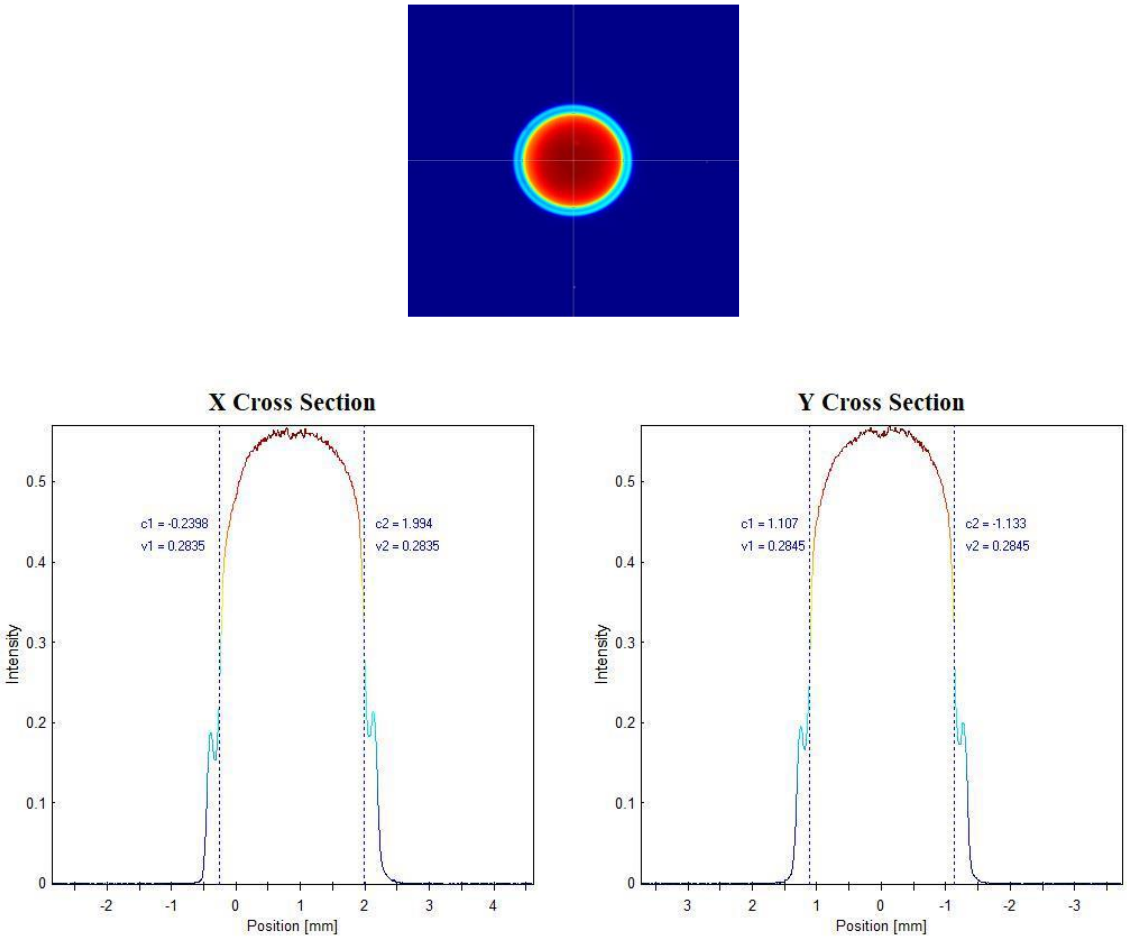

Figure 22 Beam profiling

3.1.2 POWDER FEEDER

The powder was fed to the nozzle via a GTV-type PF system (Figure 23) designed to convey, store and meter the powder. The detailed identification is shown in the Table 5:

Table 5 Model details of powder feeder

Product	GTV powder feeder
Type	GTV-PF 2/2 MF
Model number	953.016
Serial number	402.531
Year of manufacture	2016

It consisted of dual powder hoppers (dosing units) and a lower cabinet which held the powder hopper. This cabinet contained the drive and the Siemens S7 PLC control. The heating mat on the hopper aided in keeping the powder at a constant temperature during the process.

Figure 23 Powder feeder

The powder mass being driven down was measured over one minute at various disc RPMs on the controller. In detail, the procedure was carried out according to the following order powder ignition, 15 seconds empty, moving inside the container, one minute of powder shooting, and moving out of the container.

316L stainless steel powder (-160 + 53 µm) with 7.5 l/min of Argon 5.0 as carrier gas was used for this calibration.

The relationship between the powder feed rate and the disc RPMs is plotted as a flow calibration curve, as shown in Figure 24.

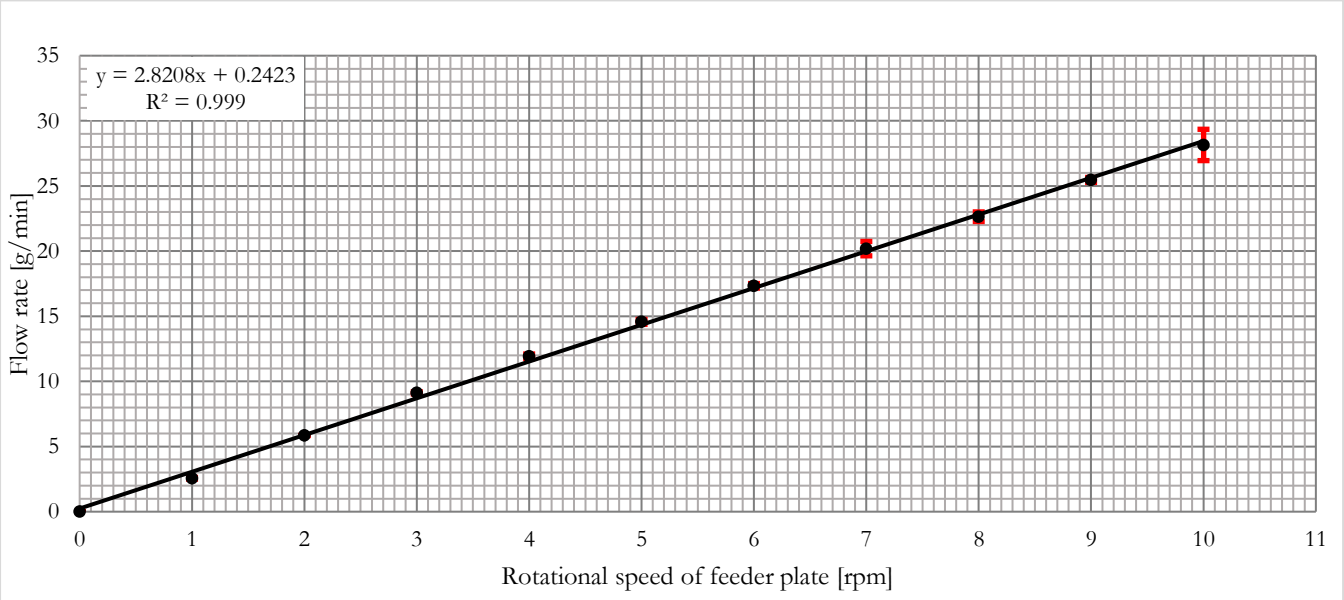

Figure 24 Relationship between powder flow mass rate and rotational speed of feeder

The slope equation can then be written as Equation 7:

Equation 7

$$y = 2.8208x + 0.2423$$

For example, from the above graph, for a disc revolution per minute of 3 RPM, the resulting g/min can be calculated using the slope equation obtained from the graph as shown in Table 6.

Table 6 Conversion of RPM to g/min

Linear Conversion	
Rotational speed of feeder [rpm]	g/min
3	2.8208×C21+0.2423 = 8.7

Out of the two powder hoppers, only one was used for the experiments that were carried out. The dual powder is helpful for multi-material manufacturing.

3.1.3 CARRIER GAS

A carrier gas is necessary that takes the powder to the delivery nozzle. The powder feeder used in this experiment was recommended to be operated with argon/nitrogen or helium. Oxygen, hydrogen, and other flammable gases were not permitted. However, if this powder feeder is to be used for thermal spraying, it is recommended that enough carrier gas flows through the powder feeder before igniting the laser.

For the present experiments, argon was used as a carrier gas.

3.1.4 DELIVERY NOZZLE

A GTV coaxial powder nozzle was used, developed explicitly for LC in material processing. The approved materials included steel material of all kinds, nickel, cobalt and copper-based alloys and precious metals. A detailed description of the nozzle is presented in the Table 7 for identification purposes.

Table 7 Model details of deliver nozzle

Product	GTV multi-jet nozzle Coaxial
Type	PN6625
Year of manufacture	2016

The nozzle could generate six single powder jets about 20 mm below the nozzle. The schematic of the nozzle is shown in Figure 25. The typical powder grain size that the nozzle could handle was from 53 – 160 μm with a powder stream focus from the 2 – 6 mm range. The nozzle length was 60 mm and approximately 180 mm, including the posting unit.

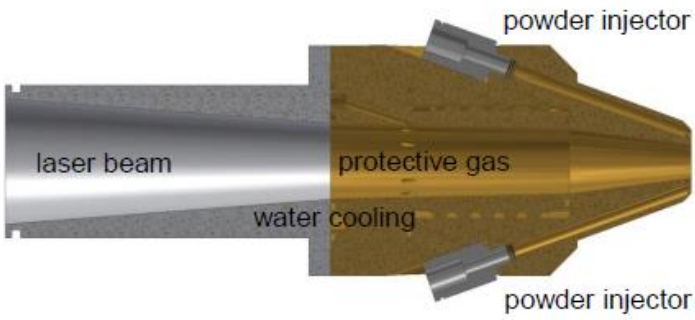

Figure 25 Schematic of the nozzle[232]

The powder focus was measured by switching on the powder and measuring from the bottom edge of the powder nozzle to the intersection of the powder jets. This distance was adjusted by loosening the nozzle nut. After setting the correct distance, the nozzle was aligned with the laser spot. This was done by adjusting the two-positioning screw's location on the positioning unit while keeping the laser, and powder feeder switched on. The settings for working distance could be clearly presented by the Figure 26.

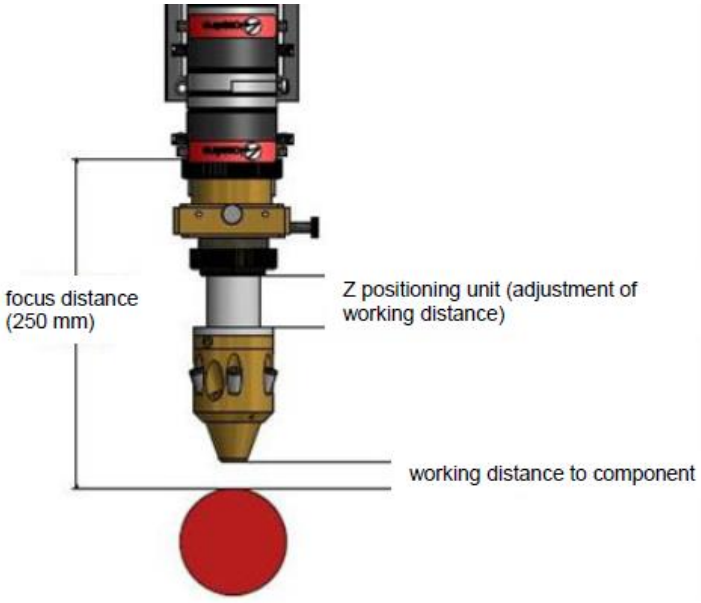

Figure 26 Schematic of setting the working distance[232]

A pre-measured metallic component was placed under the nozzle for the initial setting-up of working distance to the component, which was further tuned afterwards.

3.1.5 NOZZLE CHILLER

To avoid overheating and a continuous operation, a chiller was installed for the flow of cooling water to keep the nozzle at optimum temperature during the process.

3.1.6 SHIELDING GAS

Shielding gas is required to prevent splashes and fumes from entering the interior of the nozzle and prohibits the contamination of the nozzle and optics. Argon was used as the shielding gas. The shielding gas also prevents oxidation and aids in the cooling of the coating. The strength of the shielding gas flow must be adjusted properly since it can negatively influence the shape of the powder focus.

3.1.7 CLOSED-LOOP CONTROL SYSTEM

The closed-loop control system used in these experiments was made by New Infrared Technologies (NIT) called CLAMIR (control for laser AM with infrared imaging). It works by controlling the melt pool width in real-time by adjusting the laser power. CLAMIR was installed in the laser optics mounted onto the laser head coaxially to monitor the melt pool width from the top. The installation of CLAMIR in the LC head is shown in Figure 27.

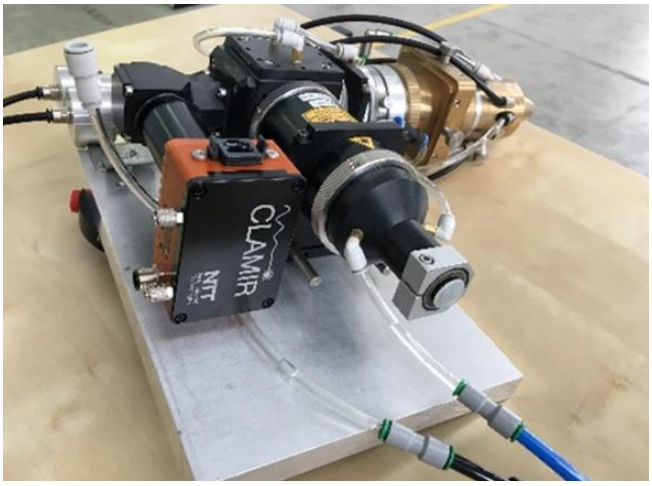

Figure 27 LC head used in the present experiments

The control system was based on a high-speed infrared camera that acquires images of melt pool width. These images were captured at a rate of 1 kHz and were 64×64 pixels. It implies that one thousand measurements of melt pool width were acquired in one second via these captured images, defined by a set threshold value. The scheme of the PID filter implemented in CLAMIR for the closed-loop feedback control is shown in Figure 28.

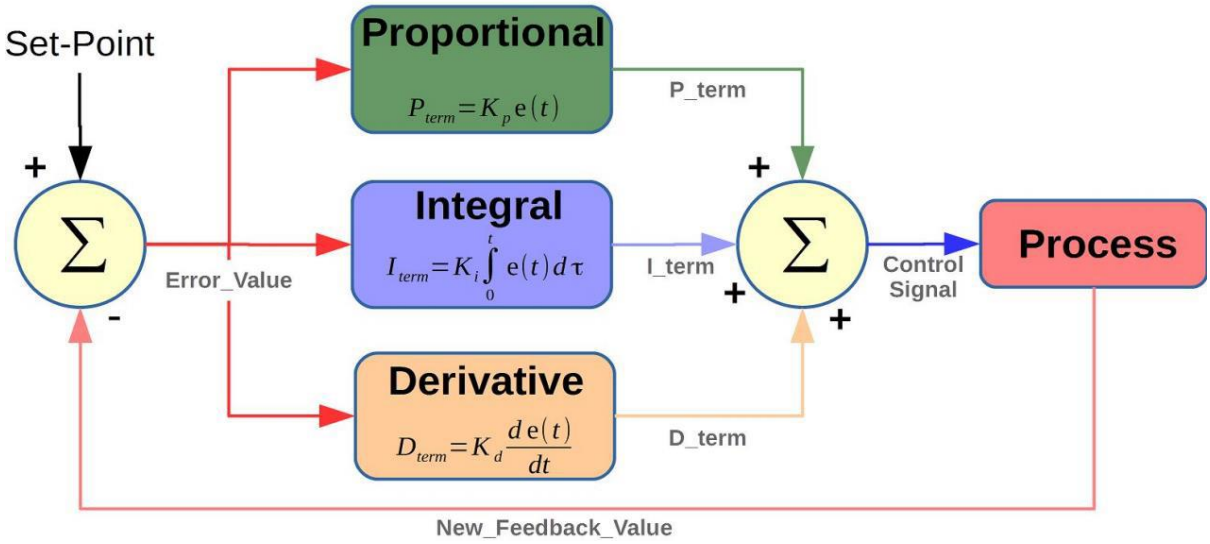

Figure 28 Working principle of CLAMIR[233]

The K_p, K_i and K_d values can be modified by writing new values in their corresponding boxes in the settings. K_p reduces a large part of the overall error. K_i reduces the final error in a system. Summing even a tiny error over time produces a significant drive signal to move the system towards a more minor error. K_d reduces the fast errors.

3.1.8 WORKSTATION

The experiments were conducted on a robotized DED system. The cladding head was mounted on a six-axis ABB Robot (IRB 4600). An additional 2-axis was given by a roto tilting table (IRBP A250). Figure 29 shows the workstation setup.

Figure 29 Workstation set-up used in the present experiments

3.2 MACHINE SHOP EQUIPMENT

The machine shop equipment used to carry out this research is presented below:

3.2.1 FURNACE

NABERTHERM furnace (Figure 30) was used to preheat the full-scale brake disc.

Figure 30 Furnace used for preheating of GCI brake disc in the present experiments

3.2.2 CUTTING MACHINES

Baoma Dk 7732 Wire cutting EDM machine, was used to cut the full-scale brake disc samples. For preparation of metallurgical sample the mitter saw and abrasive saw were used. Figure 31 shows all these cutting machines.

(a) EDM (b) Mitter saw (c) Abrasive saw

Figure 31 Cutting machines used for sampling in the present experiments

3.3 LAB EQUIPMENT

The molding press (REMET IPA 30) was used to mount the samples in a resin. The samples were then grinded (REMET LSA grinding machine) by SiC abrasive papers and were polished up to 1 μm by using a diamond spray. The set-up used is shown in Figure 32.

(a) Moulding press (b) Grinding and polishing machine

Figure 32 Machines used for preparation of metallographic samples

3.3.1 MICROSCOPE

For metallurgical analysis the ZEISS inverted Optical microscope was used. The equipment used for microhardness tests of the samples and the optical microscope are shown in Figure 33.

(a) (b)

Figure 33 (a) Microscope used (b) Vickers microhardness test

3.4 SET-UP FOR EMISSION TESTS

The emission tests were performed at Mahine Design. KTH Royal Institute of technology in Stockholm. The set-up is shown in Figure 34.

This chamber was connected to a Dekati Gravimetric Impactor (DGI) and Dekati Electrical Low-Pressure Impactor (ELPI+). The DGI had four stages with 47 mm aluminium filters. The end of DGI had a 70 mm PTFE filter. For ELPI+, 25 mm polycarbonate filters were used for stages 1-5 and aluminium filters for the rest of the stages. The aluminium filters are standard filters used for both devices.

The data from ELPI+ was mainly used for the emission analysis in this study. The further description of working principle of the dedicated pin on disc tribometer as well as the of ELPI+ follows.

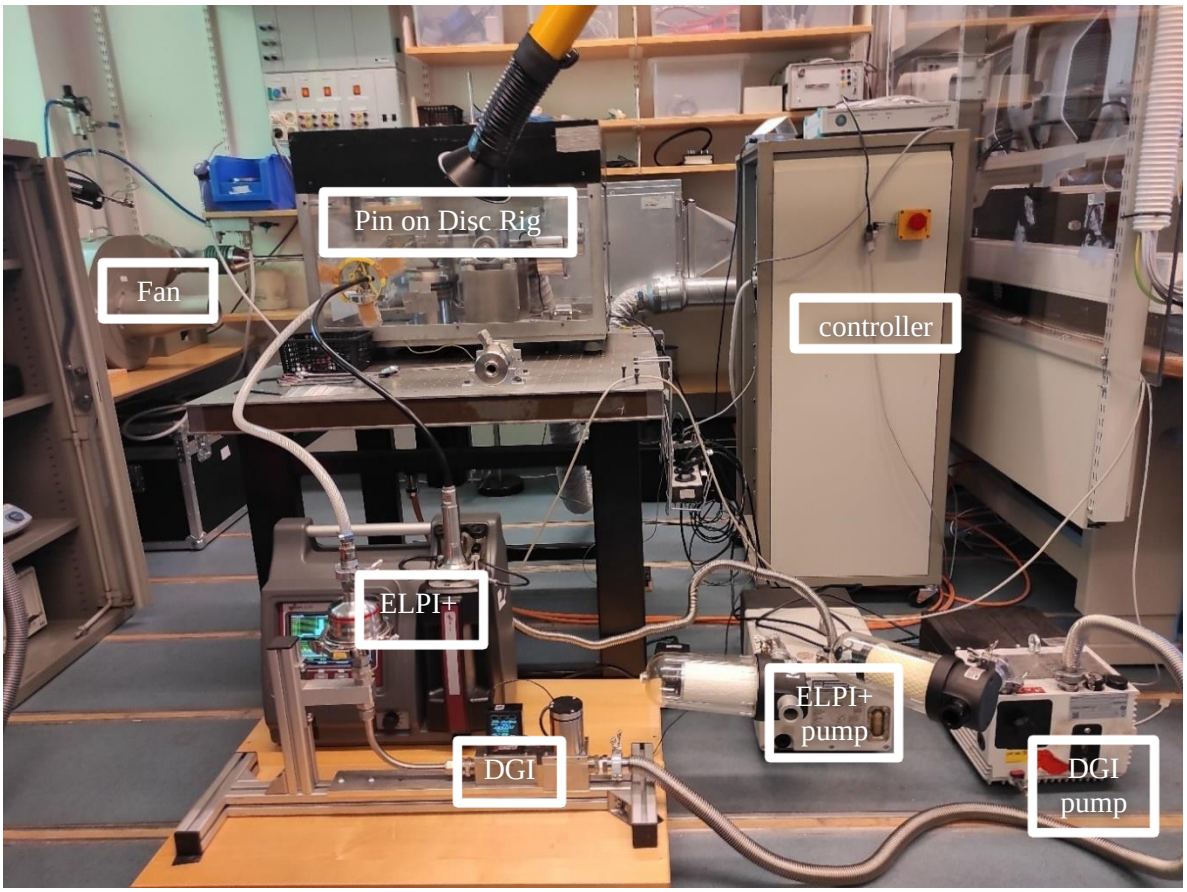

Figure 34 Set-up for emission measurements

3.4.1 ENVIRONMENTALLY CONTROLLED PIN-ON-DISC CONNECT WITH PARTICLE MEASURING INSTRUMENT

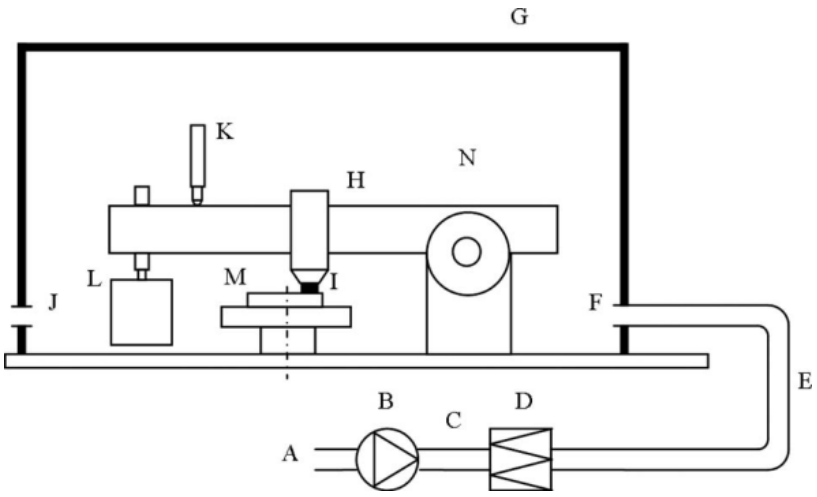

Figure 35 Schematic of environmentally controlled pin of disc rig used for emission measurements in the present experiments (A) Room air; (B) fan; (C) flow rate measurement point; (D) filter; (E) flexible tube; (F) inlet for clean air, measurement point; (G) closed box (chamber); (H) pin-on-disc machine; (N) air inside box, well mixed; (J) air out-let, measurement points; (L) dead weight; (M) rotating disc sample; and (I) pin sample[234]

Figure 35 illustrates the schematic of the test setup. The tests were performed using a pin-on-disc tribometer enclosed in a controlled climate chamber. Fan (B) supplies air to box (G) from the room (A). Filter (D) ensures the filtration of air before entering through inlet (F) via flexible tube (E). The airflow inside the chamber is controlled at 0.42 m/s via the flow measurement system (C). The air inside the box (N) is well-mixed due to the complex volume of the pin-on-disc machine (H). The outlet (J) is connected to the particle measuring instrument that collects the particles from the contact between pin (I) and rotating disc (M).

3.4.2 PARTICLE COUNTER INSTRUMENT

The low-pressure electrical impactor (ELPI+) developed by Dekati Ltd, Finland, was used to measure the particle concentration. The operating principle of ELPI+ is that the particles are charged upon passing through a unipolar corona charger (to a known positive charge level) which are then classified in a cascade impactor into 14 size classes depending on their aerodynamic size. The electrometers detect the charge carried by these particles as these particles get collected in the impactor stages. The classification of particles is based on their respective inertia, with larger particles getting collected in the upper impactor stage and smaller particles in the lower stages. ELPI+ measures the particle size distribution and concentration in the particle size range of 6 nm – 10 μm[235]. The particles were collected on greased aluminium filters during these 14 impactor stages. The operating principle of ELPI+ (uncertainty of less than 10% of the full-scale output) is shown in Figure 36.

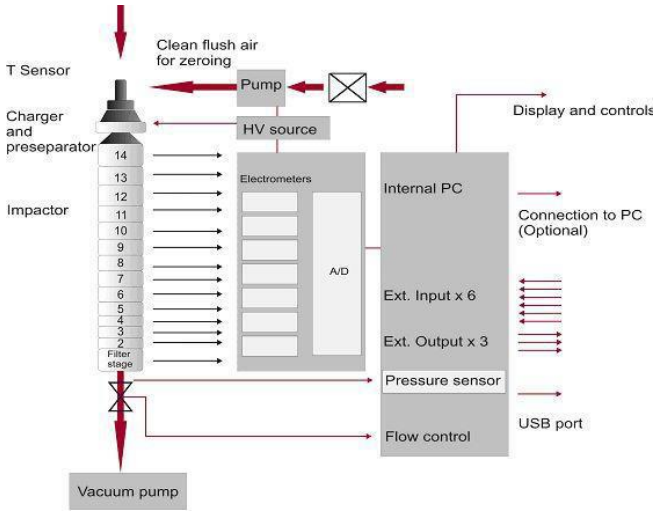

Figure 36 Operating principle of ELPI+

SARTORIUS® ME614S and METTLER TOLEDO XP2003S were used for this measurement for pin and disc specimens, respectively.

3.5 MATERIALS USED FOR LC

3.6 METALLIC POWDERS

For the preliminary tests, the metallic powders were supplied by M4P MATERIAL SOLUTIONS GmbH. The metallic powder used for the rail-wheel contact had a patent pending. All the powders were gas automized. The chemical composition (Table 8,

Table 9,

Table 10), properties (

Table 11) and size range(Table 12) are presented in tables as per the suppliers documentation.

Table 8 Chemical composition of 316L stainless steel powder

Material	Size range	Element	C	Si	Mn	P	S	N	Cr	Mo	Ni	Cu	Co	Fe
316L stainless steel	50–150 µm	Composition %	0.016	0.47	1.82	0.024	0.025	0.075	16.81	2.07	10.12	0.27	0.19	base

Table 9 Chemical composition of aluminium bronze powder

Material	Size range	Element	Cu	Al	Fe	C
CuAl10Fe1	45–125 µm	Composition %	Base	10.40	0.85	0.005

Table 10 Chemical compostion of tool steel

Material	Size range	Element	C	Si	Mn	Cr	Mo	V	Fe
		Min	0.30	0.80	0.25	4.80	1.10	0.35	Balance
Fe2343.03	45–125 µm	Max	0.34	1.20	0.50	5.50	1.50	0.55	Balance

Table 11 Properties of metallic powders used for LC

Material	Apparent density (g/cm3)	Flow (Carney Flow, Ø 5.0 mm) (s/g)
316L stainless steel	-	-

CuAl10Fe1	4.10	3.5/50
Fe2343.03	4.24	2.9/50

Table 12 Size distribution of metallic powders used for LC

Material	-45 μm	-32 μm	-20 μm	45 μm	43 μm	+53 μm	125 μm
CuAl10Fe1	0.80	0%	-	-	-		2.70%
Fe2343.03	-	-	10.70%	0.30%	-	0.0%	-
Stainless steel	50 – 150 μm						

3.7 SUBSTRATES

The chemical composition and dimensions of substrates used to perform the LC part of the research are given below (Table 13,Table 14):

Table 13 Substare dimensions for multilayer LC of 316L stainless steel

Material	Geometry and purpose	Length (mm)	Width (mm)	Height (mm)
S235JR	Rectangular for LC	80	10	10

Table 14 Substrate dimensions for multitrack LC of aluminium bronze

Material	Geometry and purpose	Length (mm)	Internal diameter (mm)	External diameter (mm)
S235JR	Pipe for LC	280	84	90

3.8 EMISSION TEST MATERIALS:

Table 15 shows the substrate materials used for the emission tests performed for brake disc / Cu free contact.

Table 15 Substrate materials for emission tests

Material	Geometry and purpose	Size	Weight

Gray lamellar cast iron	Disc cut out for lab POD tests	Ø 60 x 2 mm	340 g
Gray lamellar cast iron	Uncooled brake disc for LC	ø 300 x 12 mm	5 kg

For the rail-wheel contact the commercial contact was compared with two types of LC overlays discs. The details of which are given in Table 16. The detailed properties are listed in Chapter 7 - of PM Emission tests.

Table 16 Properties of specimens used for emission measurment of rail-wheel contact

	Case-1	Case-2	Case-3
Pin Material	Standard railway carbon steel	LC self-lubricating overlay	LC stainless steel overlay
UIC60 900A rail steel	R7 wheel steel UIC standard 812-3 (ER7 EN13262),	LC overlay with Ni-based powder alloy containing 8% manganese sulphide (MnS)[236], disc substrate steel EN S235JR.	LC overlay with martensitic stainless steel powder alloy Rockit 401, Fe-0.15C-18Cr-0.5Mo-2.5N-<3 other (Höganäs AB), disc substrate steel EN S235JR.

The pins and discs were cut from the commercial used UIC60 900A rail and R7 wheel material, respectively. Mushroom-type (round-headed) pins and cylindrical plates were manufactured to be used as pins and discs, respectively. The sketch of both pin and disc are given in Figure 37. Note that the contact radius of the pins was 50 mm.

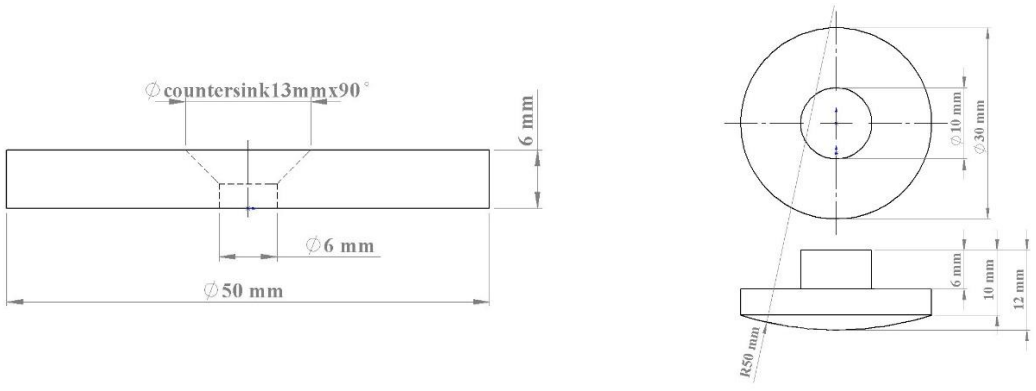

(a) (b)

Figure 37 Sketch for emissions tests of wheel-rail (a) Disc sample (b) Pin sample

Figure 38 shows the sketch of disc and pin made for the laboratory commercial brake disc / Cu free pad contact emission tests respectively. Cylindrical pins were used for this test.

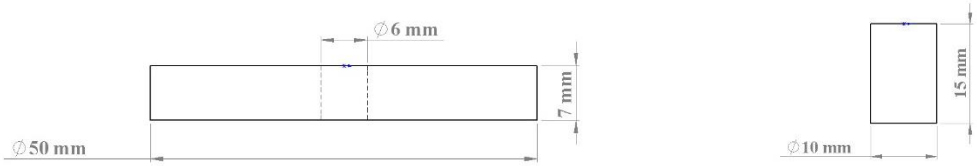

(a) (b)

Figure 38 Sketch for emissions tests of brake disc / brake pad (a) Disc sample (b) Pin sample

Chapter 4 - MULTI-LAYER COAXIAL LC OF 316L STAINLESS STEEL

The successive melting and remelting of coated layers from LC create geometric distortions. Different control loop systems are used especially in cases where multi layers are to be deposited. Multilayer coatings could be required for various purposes such as creating thicker coatings, combining different materials, or near-shape manufacturing. For this purpose, thin-walled structures of 316L stainless steel were fabricated on structural steel base. Thin-walled structures were chosen since the fabrication is quite challenging due to complex stress distribution as well as it tests the limit of smallest part fabrication from the LC technology with given equipment.

This chapter discusses the methodology and results of the deposition of thin-walled structures via LC when coupled with a closed loop control system. The effect of closed loop control system was tested as a function of laser power to control the melt pool width and in terms of two possible scan strategies. Also, the effect of gradual power reduction on deposition of thin walls are discussed. The geometrical features of the resulting walls are discussed concerning the scan strategy and the effectiveness of the closed-loop control system. Porosity, microstructure, and microhardness are also presented in this chapter.

4.1 METHODOLOGY

A rapid code was developed from ABB ROBOSTUDIO software to fabricate thin walls. The effect of constant laser power was studied and compared with a manual power reduction on the fabrication of such parts. The walls were fabricated with and without the closed-loop control system. The effect of a closed-loop control system on scan strategy was also studied and compared. A total of 70 layers were deposited by using 316L stainless steel powder. The start and end point of the arrow shown in Figure 39 represents the status of the laser, i.e., on and off, respectively. The resulting scan strategy was then termed Bidirectional and Unidirectional.

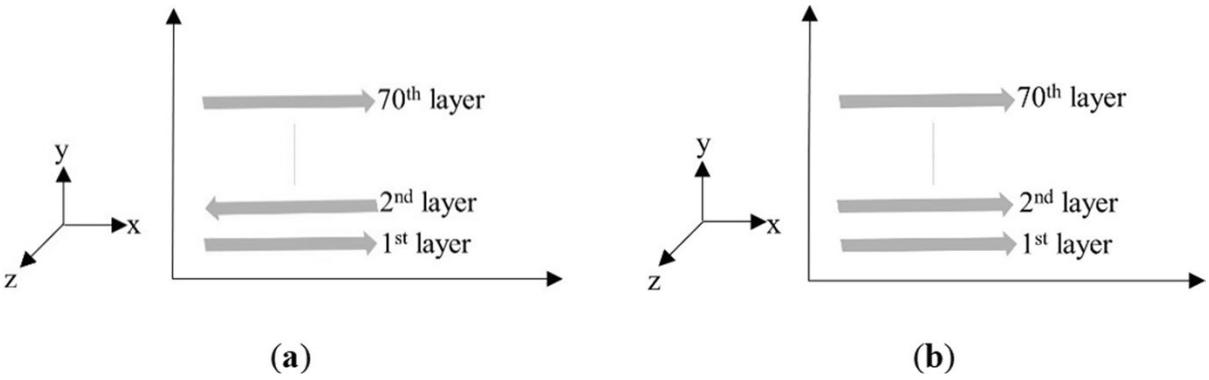

Figure 39 Scan strategies. (a) Bi-directional (b) Uni-directional

The process parameters used in this experiment were taken from the previous handling of the same powder with the given DED system. The stand-off distance between the nozzle and the deposited material must be constant to achieve good geometric stability. The increment for each layer was selected based on the previously performed experiments. Due to the complex nature of the process, as of now, there does not exist a standard way to determine these values. Therefore, in general, this increment value on the z-axis is based on the hit, trial method and a value of 0.4 mm was deemed suitable for our system and employed for this experiment.

Argon was used as a carrier and shielding gas with a flow rate of 7.5 l/min and 20 l/min, respectively. Scan speed and powder feed rate were kept constant at 17 mm/s and 9.1 g/min, respectively. A total of 70 layers with a theoretical length of 40 mm were deposited for all the samples. The variable process parameters are reported in the Table 17.

Table 17 Process parameters for multilayer LC of 316L stainless steel

Sample	Scan Strategy	Power Mode	Initial Power (W)	ΔP (W)	P minimum

1	Bidirectional	Constant	2000	0	/
2	Bidirectional	Manual Reduction	2000	100	1000
3	Unidirectional	Manual Reduction	2000	100	1000
4	Bidirectional	CLAMIR	2000	CLAMIR controlled	-
5	Bidirectional	CLAMIR	2000	CLAMIR controlled	-
6	Unidirectional	CLAMIR	2000	CLAMIR controlled	-

Figure 40 shows the sectioning of samples along with the notations used in Table 18 that describes the resulting geometric values. To minimize the effect of acceleration and deceleration the measurements the wall samples were cut from the middle along the length. The sectioning was made from where the wall reached the maximum height where the former could not apply. The samples were also cut into half to make the size feasible for the mounting press. The samples were mounted and polished with Sic abrasive paper from grit size ranging from 800 µm to 2000 µm. The samples were further polished by up to 1 µm by using diamond spray. These were then etched using Nital etchant to reveal the deposition depth. Villela's reagent were then used to reveal the microstructure.

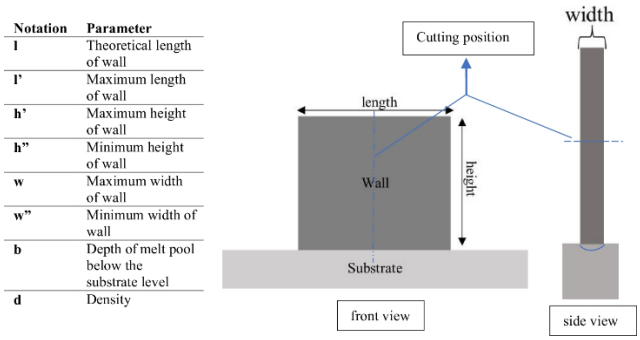

Figure 40 Sectioning of samples along with the used notations

Table 18 Results of multilayer LC of 316L stainless steel

Sample	l (mm)	l' (mm)	h' (mm)	h" (mm)	w (mm)	w" (mm)	b (mm)	d (%)
1	40	42.01	17.24	14.5	3.3	2.7	0.803	99.8
2	40	42.06	30.95	30.2	3.2	2.6	0.798	99.7
3	40	33.01	33.01	-	2.9	2.8	0.777	99.9
4	40	42.17	32.46	31.9	2.8	2.6	0.791	99.5
5	40	41.8	32.27	32.3	2.5	2.2	0.258	99.4
6	40	33	32.56	-	2.5	1.6	0.819	99.7

4.2 RESULTS AND DISCUSSION

4.2.1 BIDIRECTIONAL SCAN STRATEGY

4.2.1.1 Deposition with constant Power:

Figure 41 shows the first impression of the LC when thin walls were built with constant power. With constant power for the initial layers, more and more heat gets dissipated through the substrate. Nevertheless, as the layer advances, more radial heat dissipation starts to occur and hence the outwards velocity of melt pool flow increases due to outward Marangoni's Effect[123]. This causes a varying width of the layers and, in this case, an increase in clad width, which causes a decrease in overall wall height. Also, gradually the layers were seen to be bent through the middle.

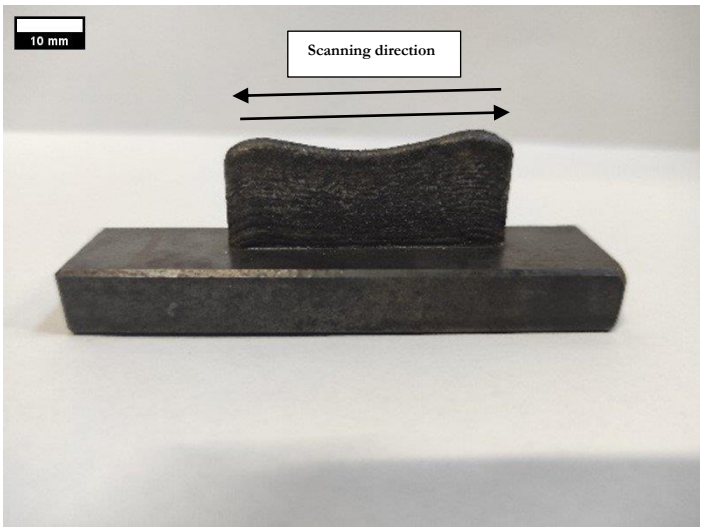

Figure 41 Thin-wall fabricated via constant power

4.2.1.2 Deposition with manual Power Reduction:

The wall was built with less power at each successive layer to remedy the geometrical inconsistency. Figure 42 shows the result of this manual power reduction. Only laser power was changed by keeping all the other parameters constant. This improvement of the geometrical features by such power reduction agrees with previous research[122,237-239].

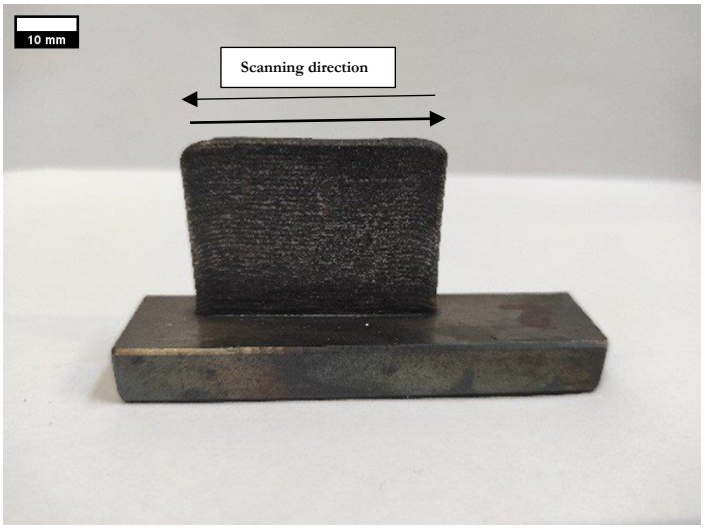

Figure 42 Thin-wall fabricated via manual power reduction

4.2.1.3 Deposition with Closed Loop Control:

Figure 43 shows the wall when tahe closed-loop control system was set to control the melt pool width at 2 mm. Relatively more consistent walls were fabricated when the CLAMIR was set to auto-calculate the melt pool width during the deposition of the first three layers and later implement control based on that value.

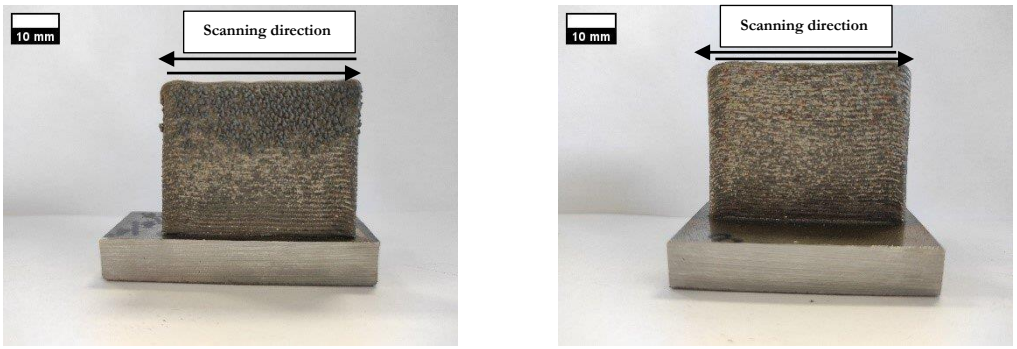

(a) (b)

Figure 43 Thin-wall fabricated samples with closed loop control system (a) Width set at 2 mm in CLAMIR (b) Automatic width set-up via CLAMIR

When the melt pool width was forced to be controlled at 2 mm via CLAMIR, the width of the cladding decreased with wall height. The un-melted powder was stuck to the wall Figure 43 (a). The reason is that on inspection of CLAMIR data, it was found that to keep the melt pool width at 2 mm, the power was reduced to almost 250 W. The graph from CALMIR data supports this, as shown in Figure 44.

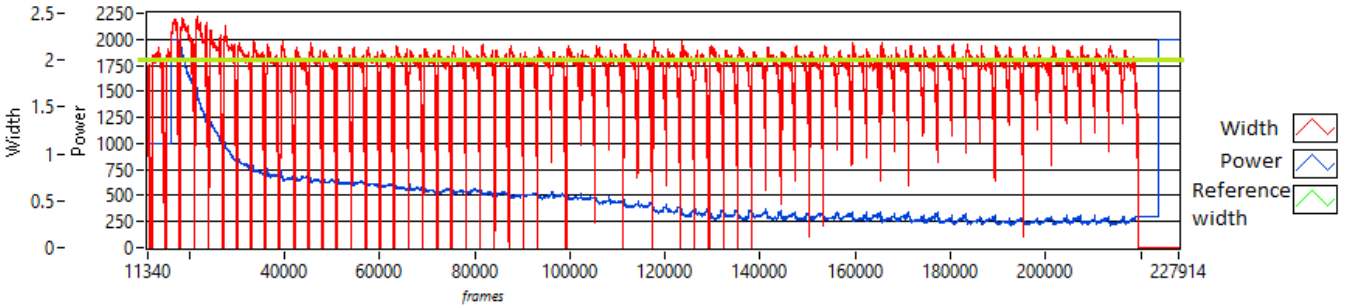

Figure 44 Power and width graph from CLAMIR with forced width of 2 mm

This reduction occurred gradually, but since the powder feed rate was constant, this low power was unable to melt enough powder. Thus, a system coupled with close-loop control for power and feed rate adjustment would bring a near-ideal system. This is also the reason for the reduced clad width for the topmost layers, where the powder is seen to be stuck to the outer surface of the wall.

The CALMIR was set to auto-calculate the melt pool during the first three layers and then implemented the control from the fourth layer in the case of sample 5. Both the clad widths, overall height and uniform-clad length were achieved with good geometric consistency. Since the melt pool width depends greatly on laser power and powder feed rate, therefore, when control was operated from system-given values, better results were seen. The obtained graph for sample 5 is given in Figure 45. The auto calculation of width for sample 5 for the first three layers reveals that the reference width changes from 2 mm to 2.31 mm, which can be seen in the graph from Figure 44 and then CLAMIR uses this reference width to control the power till the end of fabrication.

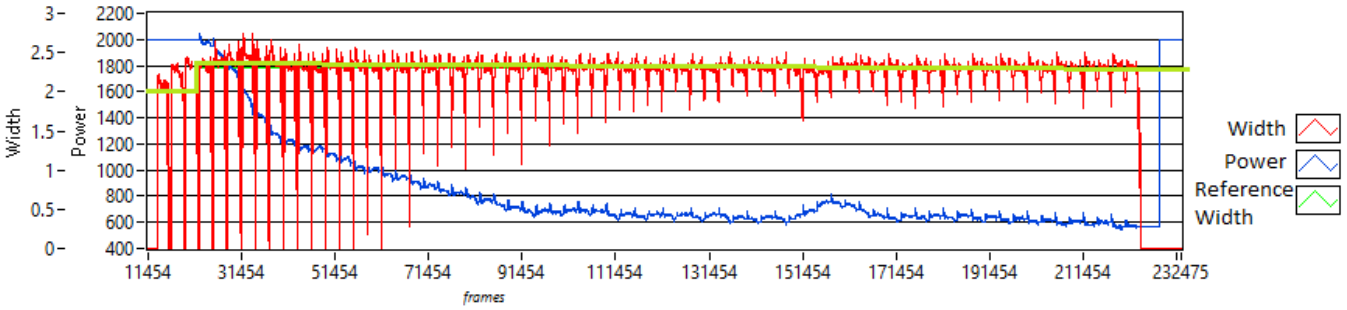

Figure 45 Power and width graph from CLAMIR with automatic width set-up

4.2.2 UNIDIRECTIONAL SCAN STRATEGY

As seen from the above sections, a closed-loop control system capable of controlling both laser power and feed rate would result in better results. The capability of the closed-loop control system was further tested by changing the scan strategy for fabricating simple thin-walled structures. Since it was clear that constant power mode is incapable of fabricating geometrically consistent walls, the unidirectional scan strategy, i.e., the laser, was kept on only at the start of the layer and switched off on return. It was tested by manually reducing the power and implementing the closed-loop control system. Figure 46 shows the walls fabricated

with a unidirectional scan strategy via both modes. Neither reducing power manually nor the closed-loop control system was able to fabricate geometrically consistent walls. The different features of starting and ending zone are counteracted via the opposite scanning direction of adjacent layers in bidirectional scan strategy. Whereas accumulation at the starting zone and decline at the ending zone was reinforced layer wise which resulted in an uneven height. Similar results were found in another research[240] for the two scan strategies, but it did not study the effect of closed-loop control system.

This implies that scan strategy is vital in fabricating simple thin-walled structures.

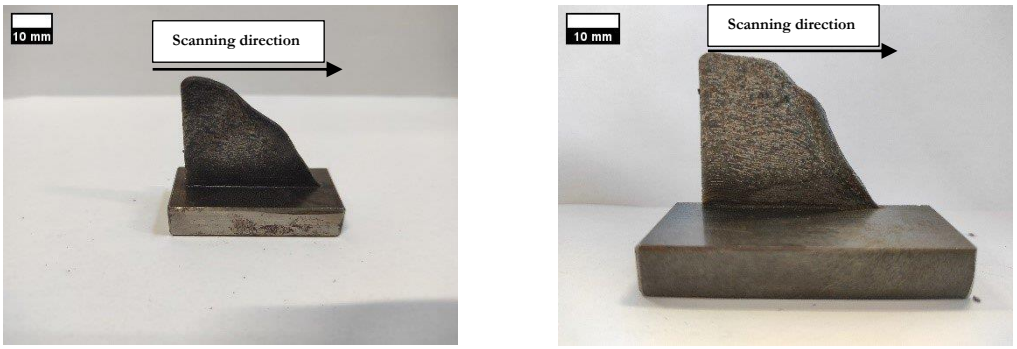

(a) (b)

Figure 46 Unidirectional scan strategy(a) Manual power reduction (without CLAMIR control (b) CLAMIR controlled

4.2.3 POROSITY ANALYSIS:

The images of polished samples taken from the microscope were evaluated for density analysis using ImageJ software by conversion to binary images. Overall, it was found that samples with excellent density were fabricated in the case of all the samples. This is attributed to the feasibility of process parameters for fabricating such thin-walled structures. The highest density was recorded for sample#1 (fabricated via constant power). The constant laser power induces an almost entirely dense part but compromises the geometrical features of the wall. The density results obtained for each sample are reported in Table 18. The porosity increased upon using closed-loop control, yet it managed to fabricate a thin wall with good geometrical features. This increase in porosity occurred due to the excessive reduction of laser power by the closed-loop control system.

4.2.4 DEPTH OF COATING INTO SUBSTRATE:

The coating depth into the substrate is reported in the table and can be visually seen in Figure 47. A stable bond between the substrate and the clad can be seen. The low penetration depth of the melt pool into the substrate for sample 4 could be explained by the extreme decrease of power CLAMIR commanded to keep the melt pool at a 2 mm width.

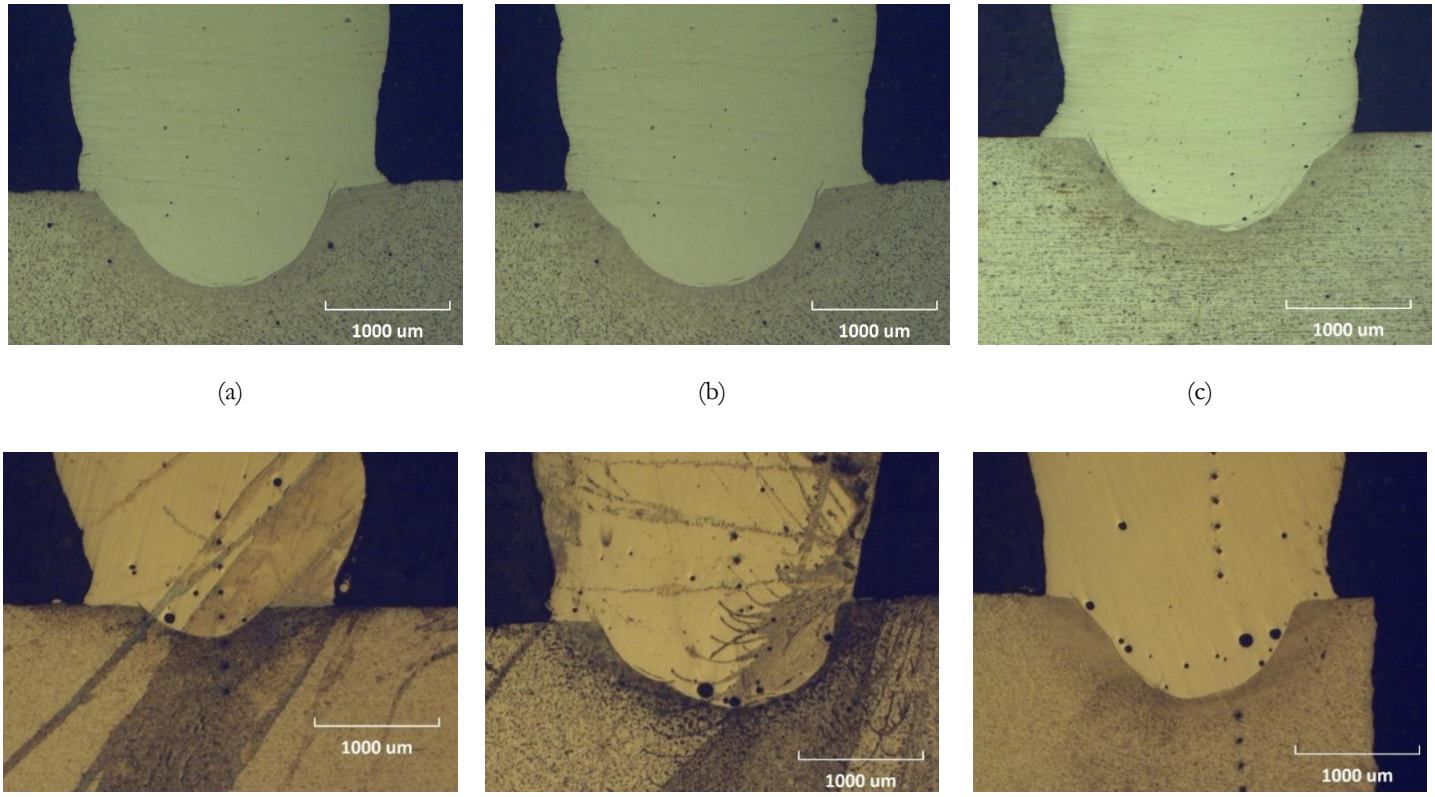

(a) (b) (c)

(d) (e) (f)

Figure 47 Deposition depth (a), (b), (c) Without CLAMIR (d), (e), (f) With CLAMIR

4.2.5 MICROSTRUCTURE:

The complex thermal behaviour makes it extremely difficult to predict the microstructure reliably. The microstructure's morphology and grain size are influenced by the main processing parameters that influence height, heating/cooling rate and bulk temperature increment[241]. The microstructure of the fabricated samples represents a columnar dendritic structure typical for the LC parts. The layers were free from defects. A more homogenous microstructure could be seen for the parts fabricated via the closed-loop control. The microstructure result coincides with work of Saboori et al.[241,242] and shows that the microstructure differs in the middle and edges of the melt pool. For the overall part, however, the microstructure grows with a columnar dendritic structure in the direction of the maximum thermal gradient for the first and middle layers. For the last layers, cellular structures were reported. Figure 48 shows the microstructure of the parts fabricated with and without CLAMIR and of the substrate.

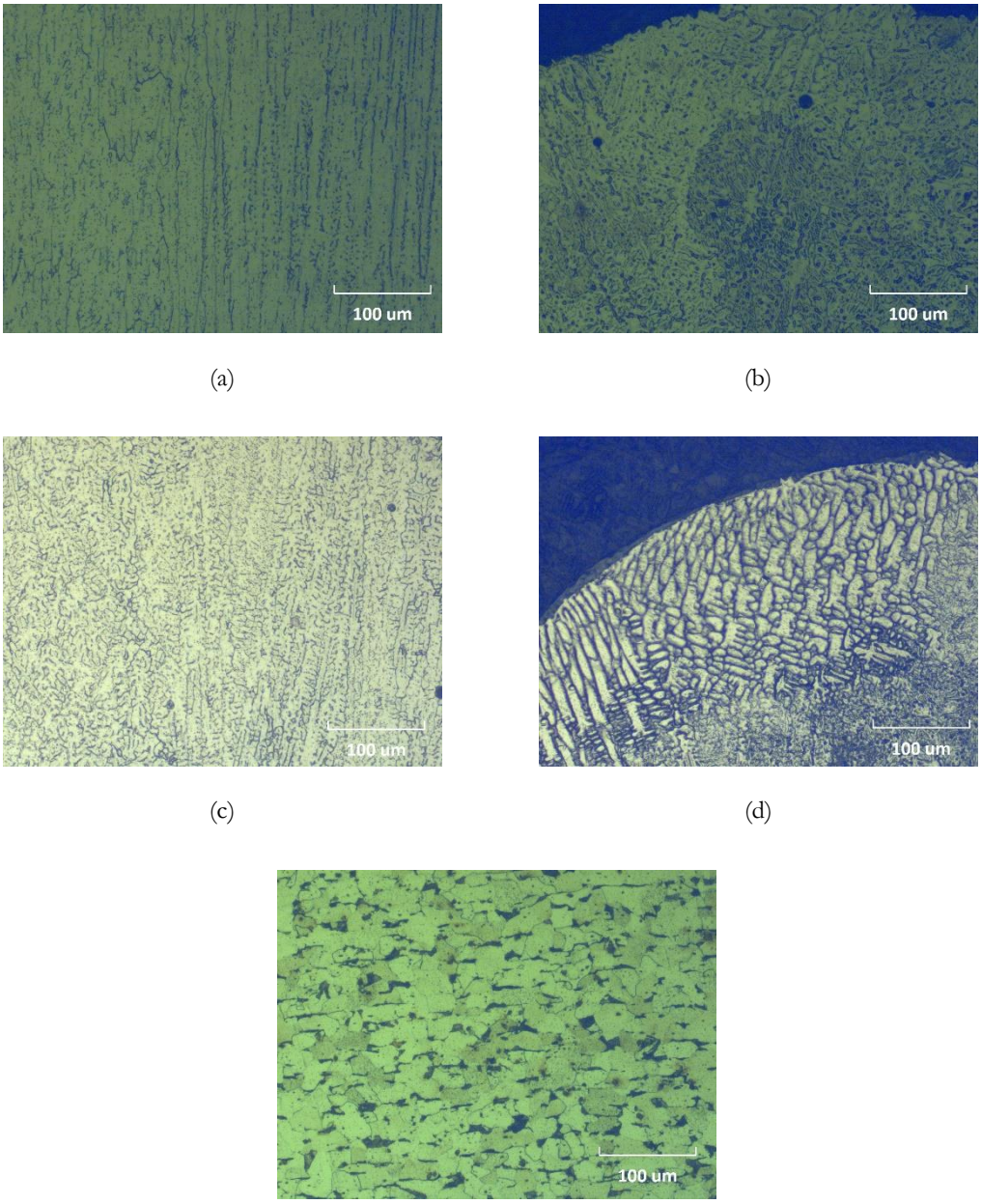

(a) (b)

(c) (d)

(e)

Figure 48 Microstructure for bidirectional scan strategy (a), (b) with constant power, (c), (d) CLAMIR controlled (e) substrate

4.2.6 MICROHARDNESS:

The microhardness measurements were taken for the substrate, dilution zone (depth of melt pool below the substrate level) and the wall for all the samples. Vickers Microhardness with 300 g load for a dwell time of 15 sec was used. Since the wall was also cut in half, therefore, the position (mm) mentioned in the graphs (Figure 49, Figure 50) was combined for all three areas (wall start, mid and extreme) and therefore depicts only the increments between successive indents for each of the three, but when combined this distance does not reflect the exact position of indent on the wall. For example, for sample 1, the position (mm) value is 5.6 mm, but it shows the extreme end of the wall, which reached a height of 17 mm, as from Table 18. The three areas are therefore mentioned in the graphs for each sample. In all the cases, regardless of

closed-loop control, the hardness value was high for the dilution zone. Microhardness decreases as the wall progress in height.

The first layers also had higher values due to the dilution between 316L stainless steel and the low-carbon steel substrate, as also shown by Abdalla R. Nassar[243]. The wall's middle layers had low hardness values compared to both the start and top layers. This attribute is typical for DED fabricated parts due to cyclic thermal history, as the heat build-up in the middle layers is higher than in the first and last layers. Due to this reason, the central layers have fewer microhardness values compared to the first and last layers of DED fabricated parts[121]. This trend is most visible for sample 4, shown in Figure 50. The hardness values for samples fabricated without closed-loop control and with manual power reduction mode are shown in Figure 49. The graph in Figure 50 represents the microhardness values for samples fabricated via closed-loop control. There was a scatter in the values within the three defined areas. Since sometimes the indent might be placed just on the interface between the two layers that returned higher values. This was evident after the etching of the samples with higher scatter values. In all the cases, the power had a significant effect on the hardness values. Upon analysing geometrically inconsistent samples, it was found that the microhardness values were lower than the other samples. In this case, the section was taken when the layer had just started towards its length.

In comparison, all the other samples were cut through the middle. This shows that the hardness values change along the height as well as along the layer length. This could be due to the different temperature gradients along the laser scan direction as compared to the temperature gradient along the height of the thin wall, as also demonstrated by Wang et al.[244].

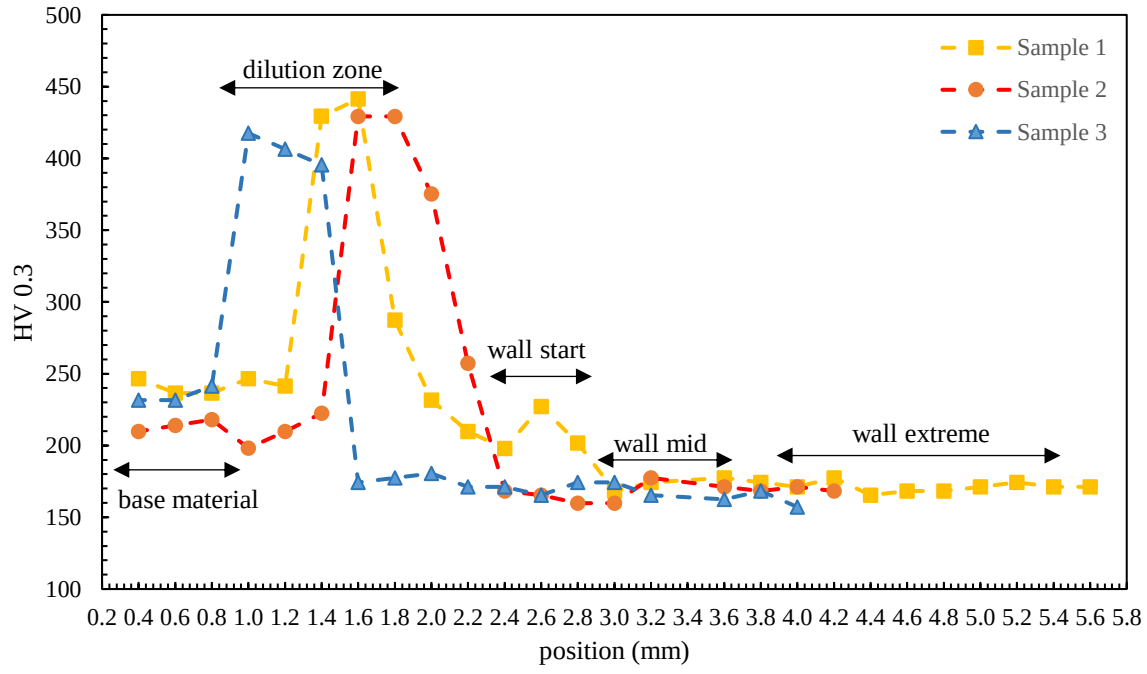

Figure 49 Microhardness graph for samples without CLAMIR

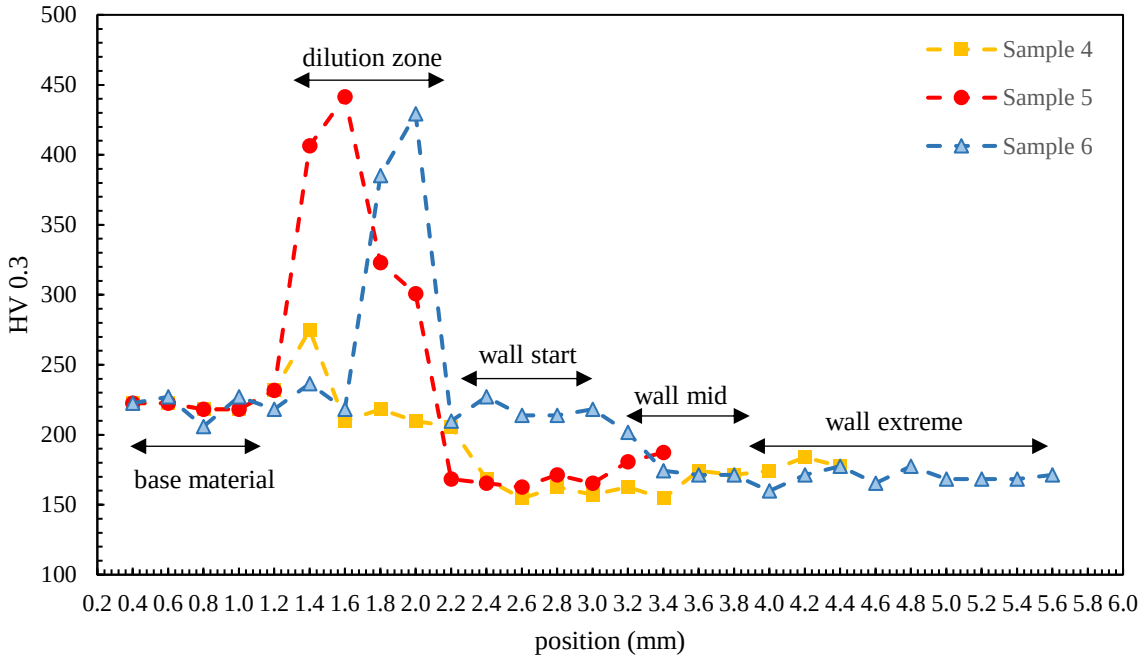

Figure 50 Microhardness for samples with CLAMIR

Chapter 5 - MULTI-TRACK COAXIAL LC OF ALUMINIUM BRONZE

Coaxial LC involves numerous interactions, such as laser beam/powder, melt pool/substrate, and laser beam/substrate. This includes various physical phenomena, such as fluid flow and phase transitions. Such interactions and the physical phenomenon could be controlled by controlling the main process parameters such as laser power, scan speed, feed rate, hatch distance, etc. However, the other associated process parameters, such as spot size, and shielding gas flow rate, also play an essential role. All these parameters have individual and combined effects on the resultant coating, making the optimisation quite challenging. Computational models are proposed for this optimisation but require highly qualified labour and increased costs. Statistical models are an alternative solution to this problem since these do not require any additional costs. The LC process models are highly relative and depend on the equipment used and the material under investigation. Therefore, the research data base for such models needs to be increased with different materials and LC equipment. The models commonly found in the literature are targeted to single-clad tracks, whereas in real scenarios, multi-track coatings are required to coat the substrate thoroughly.

Nevertheless, the importance of single-clad optimisation cannot be denied; however, the present study aimed to describe the coating achieved by depositing three tracks. The overlapping plays an essential role during dilution; therefore, the single-clad track optimisations must be carefully adjusted when it comes to the actual coating of substrates. The overlapping reduces the dilution since some of the energy is absorbed by a part of the previously deposited layer that is being overlapped and in increased clad height.

This chapter describes the methodology and discusses the results of aluminium-bronze LC. The effect of main process parameters on multi-track layers is discussed, which were used to develop a combined parameter statistically. The resulting microhardness and optical microscopy of the resulting metallurgical samples are discussed.

5.1 METHODOLOGY

The aluminium bronze powder was deposited on to S235JR pipe by varying main process parameters (laser power, scan speed, and hatch distance). The effect of these process parameters was then studied on the resulting geometric characteristics (height, width, dilution of clad).

The parameters were selected based on the previous experiments and current literature. These parameters were further tuned according to our LC system in the series of pre-tests performed. These pre-tests resulted in equivalent results to the main experiment. Factors laser power and scan speed had three levels, whereas factor hatch distance had two levels, and an entire factorial Design of Experiment (DOE) resulted in a total of eighteen trials, as shown in the Table 19. The full factorial design was chosen to use all parameter combinations and to analyse their interactions.

Table 19 Process parameters for multilayer LC of aluminium bronze

Sample. No.	P (W)	Hatch Distance (mm)	Scan Speed (m/s)
1	1800	1.2	20
2	2200	1.8	12
3	1800	1.2	12
4	2600	1.8	12
5	2600	1.2	12
6	1800	1.2	16
7	2200	1.2	16
8	2600	1.8	20
9	1800	1.8	12
10	2200	1.2	12
11	2200	1.2	20
12	2200	1.8	20
13	1800	1.8	20
14	2600	1.2	20
15	2600	1.2	16
16	2600	1.8	16
17	1800	1.8	16
18	2200	1.8	16

Argon was used as a carrier and shielding gas with a flow rate of 7.5 l/min and 20 l/min, respectively. It was applied via the orifices in the nozzle and helped cool the deposited layer. The powder feed rate was kept constant at a rate of 200 mg/s. Continuous spiral clads of three tracks were deposited for each of the 18 runs.

5.2 RESULTS AND DISCUSSION

The samples from 1 to 18 correspond to the cladded pipe, as shown in Figure 51. The pipe was sectioned transversely for geometric and metallographic analysis. The sectioning profile of the samples is also presnted. The pipe was cut transversely, and the metallographic samples were prepared. The samples were grounded with silicon carbide paper (200 – 2000 grit size), a rotating disc with water as a lubricant, and later polished up to 1 μm using a diamond abrasive.

Figure 51 Processed pipe and sample profiling

Figure 52 shows the considerations for geometric measurements i.e., the width of coating w, the height of clad h, and the penetration depth b. These features were observed under inverted ZEISS optical microscope. The density measurements were taken via ImageJ software by performing an image analysis.

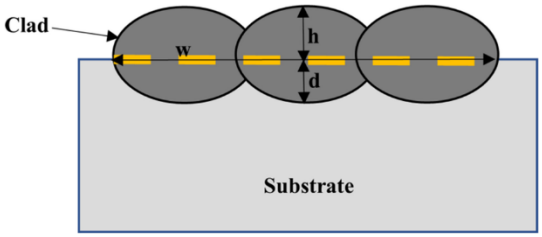

Figure 52 Geometric considerations for coating

The percentage of dilution was determined by area method according to Equation 8.

Equation 8

$$\% \text{ Dilution (D)} = \frac{d}{h+d} \times 100$$

Table 20 Results of multilayer LC of aluminium bronze

Sample number	H (mm)	W (mm)	D (%)
1	1.20	4.70	11.48
2	1.51	6.41	12.92
3	1.91	4.88	8.47
4	1.45	6.71	13.33
5	1.95	5.59	11.70
6	1.36	5.01	13.00
7	1.39	5.28	10.75
8	0.86	6.32	19.14
9	1.28	6.26	9.33
10	1.81	5.5	9.74
11	1.23	5.12	13.44
12	1.08	6.08	15.51
13	0.94	5.86	14.88
14	1.19	5.19	12.96
15	1.44	5.35	13.10
16	1.11	6.33	15.56
17	1.19	6.35	14.34
18	1.07	6.32	15.20

Table 20 presents the results of the main geometrical features against the main processing parameters. The individual effect of all three processing parameters power (P), scan speed (V), and hatch distance (HD) were plotted against the height of the cladding. The aim here is to find the combined parameter derived

from P, V and HD that could linearly depend on clad height. These plots do not concern the combined effect but provide useful information in our quest of finding the values of α, β, and γ and ultimately the combined parameter.

5.2.1 Optical Microscopy

The cross-sectional optical micrographs are arranged to decrease hatch distance from bottom to top and increase scan speed from right to left for each specific laser power used (Figure 53). The qualitative features of the main processing parameters on the geometrical characteristics of clads can be observed. Well-bonded clads without major defects were formed for all the processing parameters with some porosity. The beads were improperly shaped at low speeds, and this effect is more apparent at a hatch distance of 1.2 m. The clad height depicts an inverse relationship with laser power with the increased speed at a constant feed rate. Wider clads were formed with increased hatch distance and scan speed for all laser power values. The waviness of the tracks also seems to decrease with the increase of laser power, which correspond to less post-processing. The dilution seems to have a direct relationship with laser power and is independent of the feed rate since it was kept constant. These geometrical variations can be controlled by establishing a combined parameter by using P^{α}, V^{β} and HD^{γ} depending on the dependence of each geometrical characteristic on the individual parameter. On that account, the geometrical characteristic of the resulting clads was investigated against combined parameters and examined via statistics.

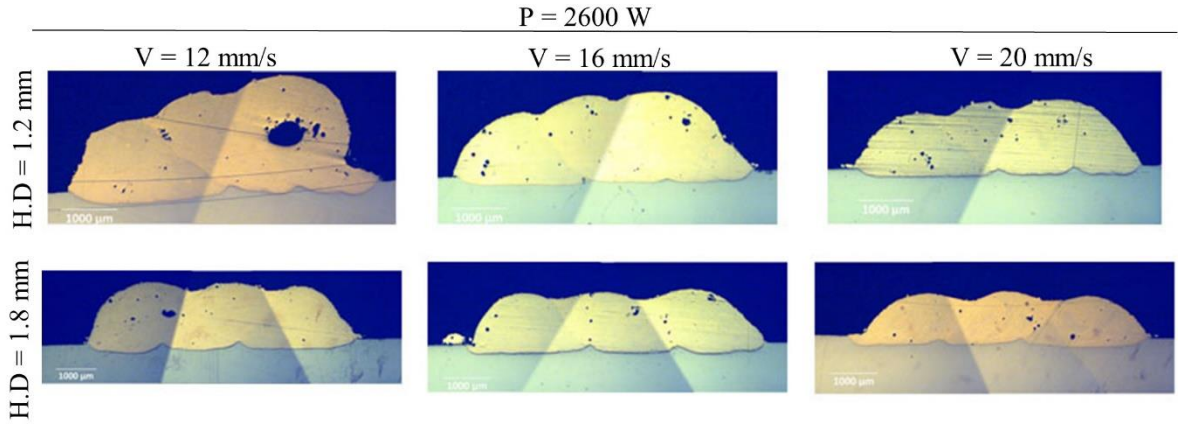

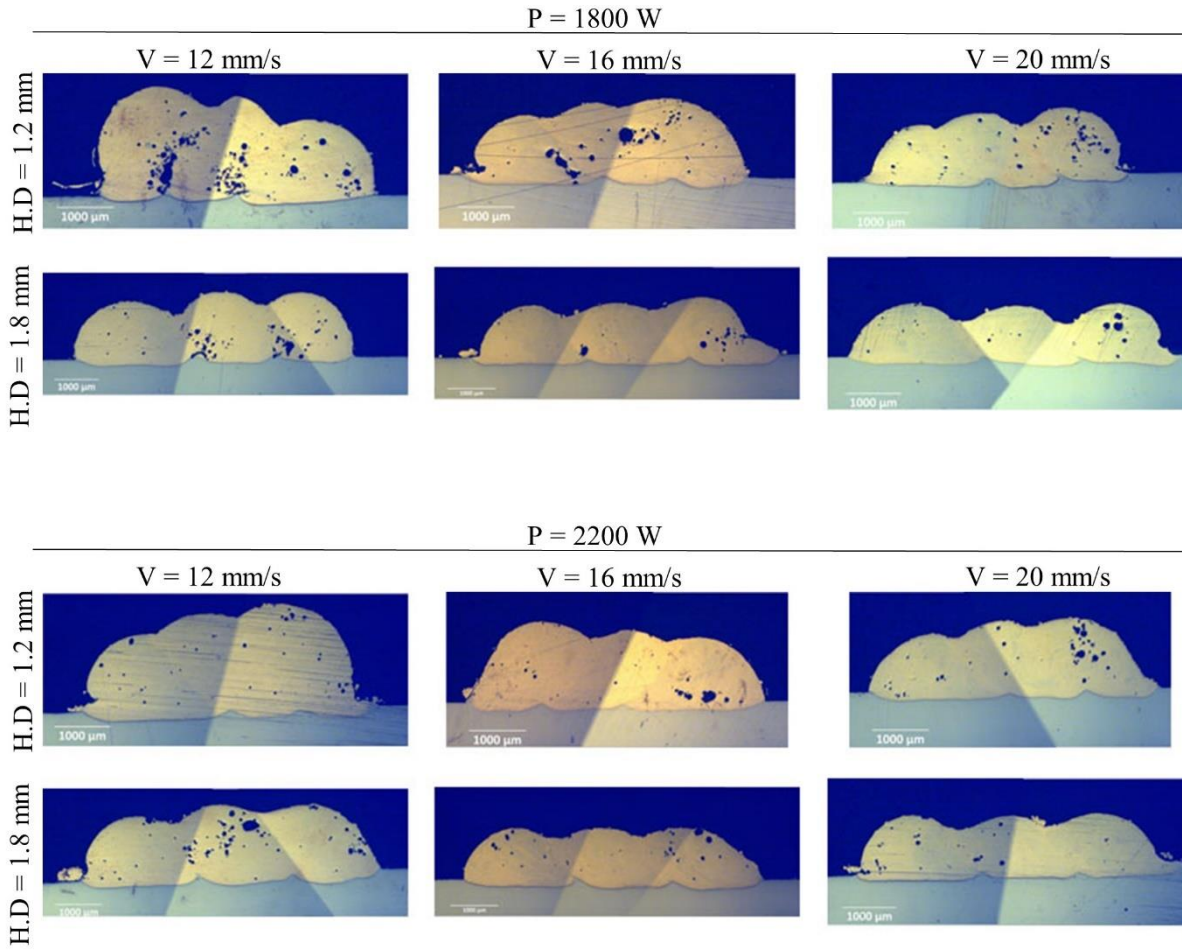

Figure 53 Cross sectional optical micrographs for coating. Scan speed (V) increase from right to left and hatch distance (HD) from top to bottom for each given power (P)

5.2.2 GEOMETRICAL CHARACTERISTICS OF COATING

5.2.2.1 Clad Height

The individual effect of the three processing parameters is shown in Figure 54 ((a), (b), (c)). Hatch distance and scan speed account for a more significant effect on clad height than the laser power. This agrees with previous research[245], where scan speed significantly impacts clad height more than laser power. The deposition rate per unit length decreases with increasing scan speed. An increased hatch distance also results in elevated clad heights due to overlapping. However, many studies[141,145,246-248] reported laser power as a significant factor in controlling clad height. This held when the processing parameters were coupled with the feed rate. Among feed rate and laser power Bennet et al.[249] reported that feed rate has a more significant effect on the clad height than laser power. Furthermore, the catchment efficiency determines the fraction of laser energy absorbed by the feedstock powder particles that reach the melt pool. This implies that with a constant feed rate same amount of powder will be melted upon interaction with the laser beam.

Therefore, the combined parameter that controls clad height does not include the laser power due to its negligible effect. The statistical dependence of clad height is shown in Figure 54. The clad height is found to be directly proportional to $V^{-1.5}.HD^{-1.1}$ with an R-sq. of 0.95. The high regression coefficient and the residuals plot confirm the linear model.

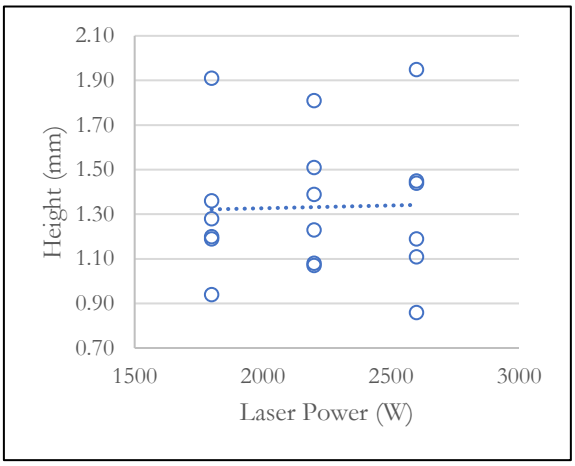

(a)

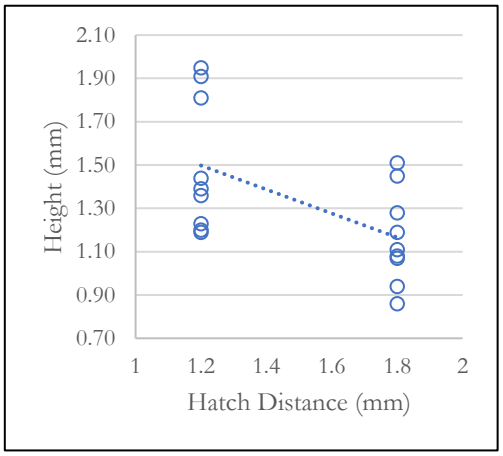

(b)

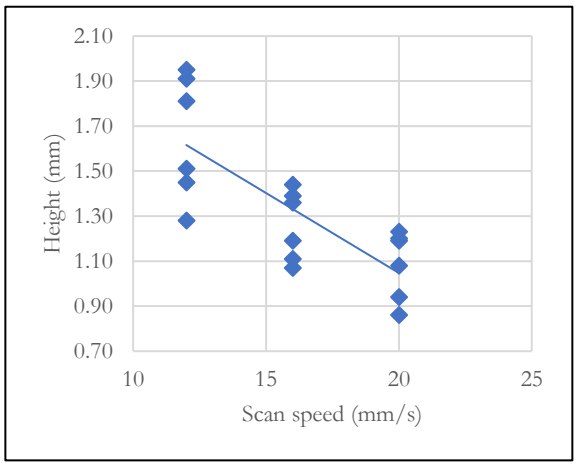

(c)

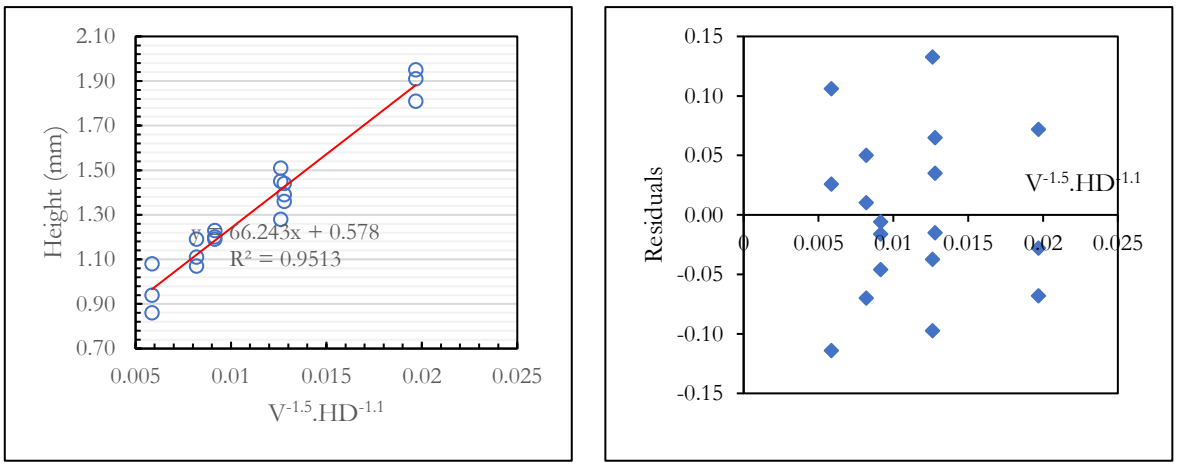

(d) (e)

Figure 54 Dependence of coating height on (a) laser power (P) (b) scan speed (V) and (c) hatch distance (HD) (d) combined parameter (e) residuals

5.2.2.2 Clad Width

The individual effect of the three processing parameters is shown in Figure 55 ((a), (b) and (c)). Clad width is directly proportional to power and hatch distance, whereas inversely proportional to scan speed. Therefore, for predicting the combined parameter that could effectively control the clad width, all three parameters were taken into account. Also, from the relationship, it was clear that the value of alpha and beta would be positive, whereas the values for gamma would be negative.

The combined parameter found in this study (Figure 55(c)) is correlated with previous research in which feed rate was a variable instead of hatch distance for clad width[141]. It is to be noted here that the combined parameters are highly dependent on substrate/powder and experimental setup. Shear effect and Marangoni's effect, along with other forces, account for the melt pool formation in LC and process parameters play a vital role in determining these effects[31]. In the present study, adding hatch distance as a variable could have changed the overall effect on the melt pool, which resulted in all the parameters having a detrimental effect on the clad width. In many studies[141,143,144], the clad width mainly depended on laser power and scan speed, where hatch distance was not a variable. This corresponds to the fact that an addition or removal of one parameter in LC could influence the effect of individual parameters in determining the geometry of the coating.

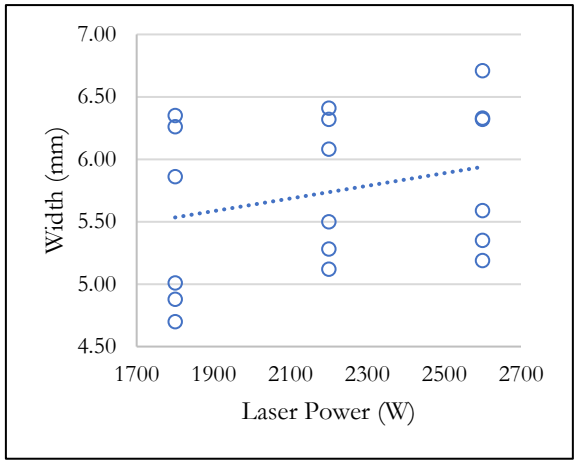

(a)

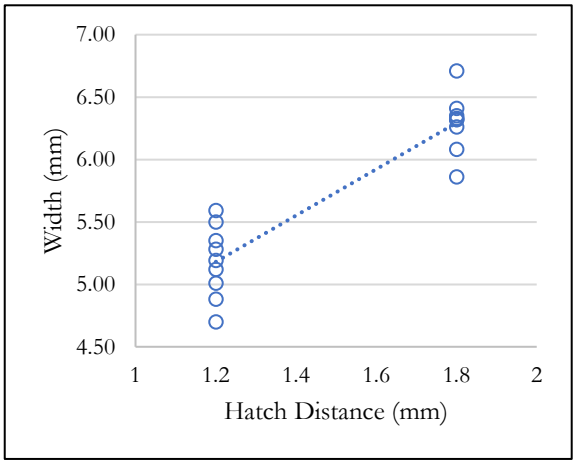

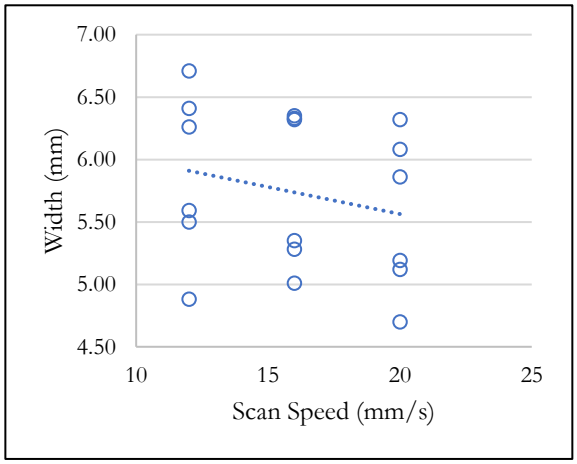

(b) (c)

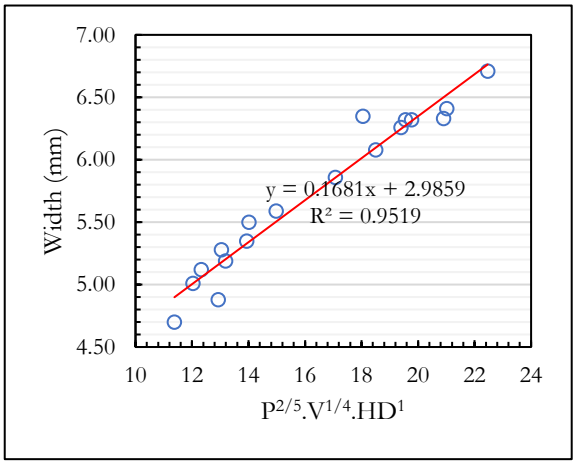

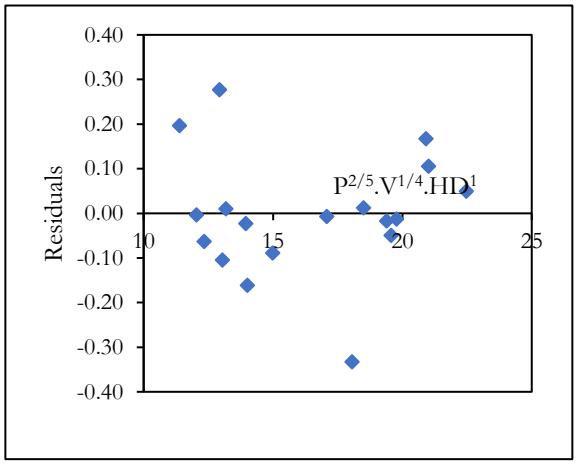

(d) (e)

Figure 55 Dependence of coating width on (a) laser power (P) (b) scan speed (V) and (c) hatch distance (HD) (d) combined parameter (e) residuals

5.2.2.3 Percentage of Dilution

The percentage of dilution was calculated according to Equation 8. It is an important property to measure since it could represent the metallurgical bond between the substrate and the clad.

Similarly, to find the combined parameter, first, the individual graphs for each parameter were plotted to understand the effect of the respective parameter under consideration. Since it was impossible to obtain a sufficiently valid model with a linear regression corresponding to an acceptable R-sq, logarithmic regression was used instead. The logarithmic regression employed in the present study is in agreement with previous research[141].

The combined parameter that can linearly control the % dilution was $P^{1.1}V^{1.25}HD^{1.2}$ Figure 56 (d). The R-sq. Value and residuals confirm the validity of the model. Assuming the scan speed to be constant, an increase in laser power will result in increased absorption of energy into powder metal as well as the substrate. This increased absorption of energy will result in deeper depositions. However, an increase in scan speed can decrease the deposition depth with controlled laser power. Hatch distance also plays a critical role because an increased hatch distance corresponds to increased interaction between the laser beam and substrate, resulting in more significant melting of the substrate and increased dilution.

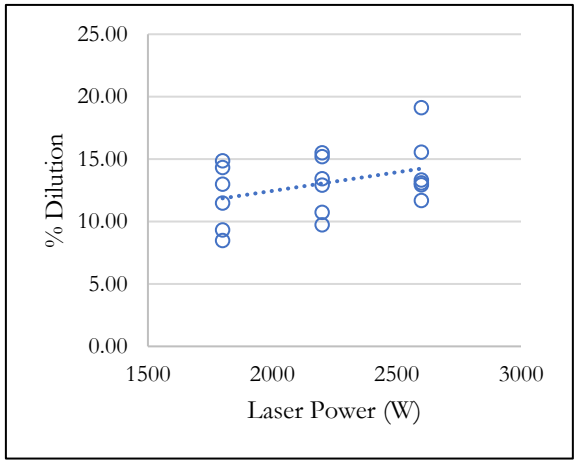

(a)

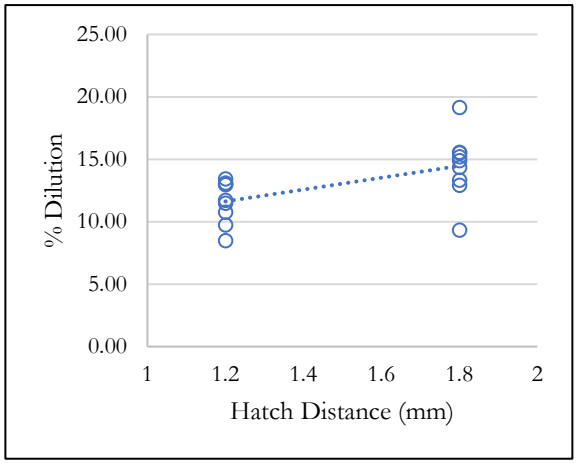

(b)

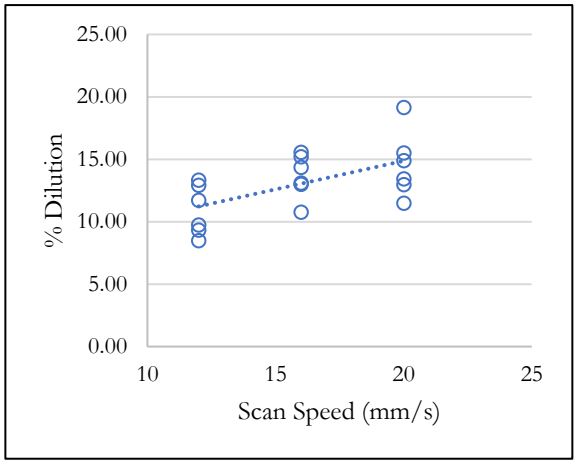

(c)

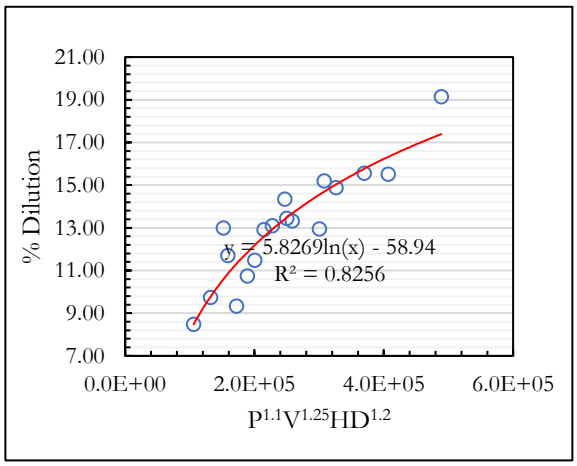

(d)

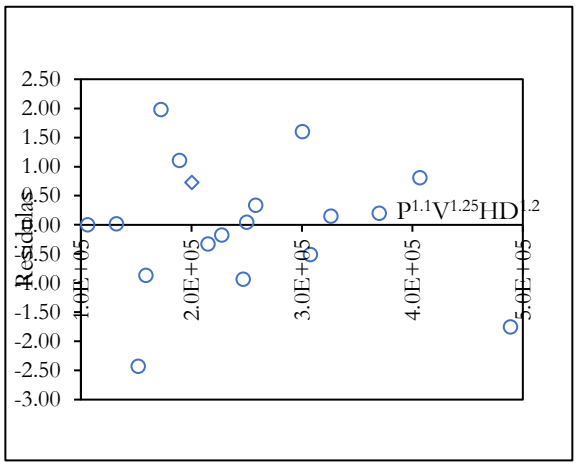

(e)

Figure 56 Dependence of coating % dilution on (a) laser power (P) (b) scan speed (V) and (c) hatch distance (HD) (d) combined parameter (e) residuals

The predicted combined parameters from this study for geometrical characteristics of coating are summarised in Table 21. The high correlation coefficient depicts the uniformity of the results.

Table 21 Predicted combined parameters for multitrack LC of aluminium bornze

Measured Quantity (y)	Combined parameter (x)	Square of Correlation coefficient (R-sq)	a	b
h (mm)	$V^{-1.5}.HD^{-1.1}$	0.95	66.243	0.578
w (mm)	$P^{2/5}.V^{1/4}.HD^{1}$	0.95	0.1681	2.9859
D (%)	$P^{1.1}.V^{1.25}.HD^{1.2}$	0.83	5.8269	-58.94

5.2.3 Microhardness

The average microhardness of the dilution zone is found to be more significant as compared to both substrate and coating for all the samples. In all cases, the coating also has microhardness greater than the typical coating material. The coating microhardness was found to be 250 $HV_{0.3}$ which is more than that of the typically used hardness of aluminium bronze[250]. The overall comparison of microhardness values among the samples reveals no significant differences, implying that the average microhardness was not significantly affected by a given set of parameters. Figure 57 shows the microhardness profile that runs from the substrate through the interface towards the coating.

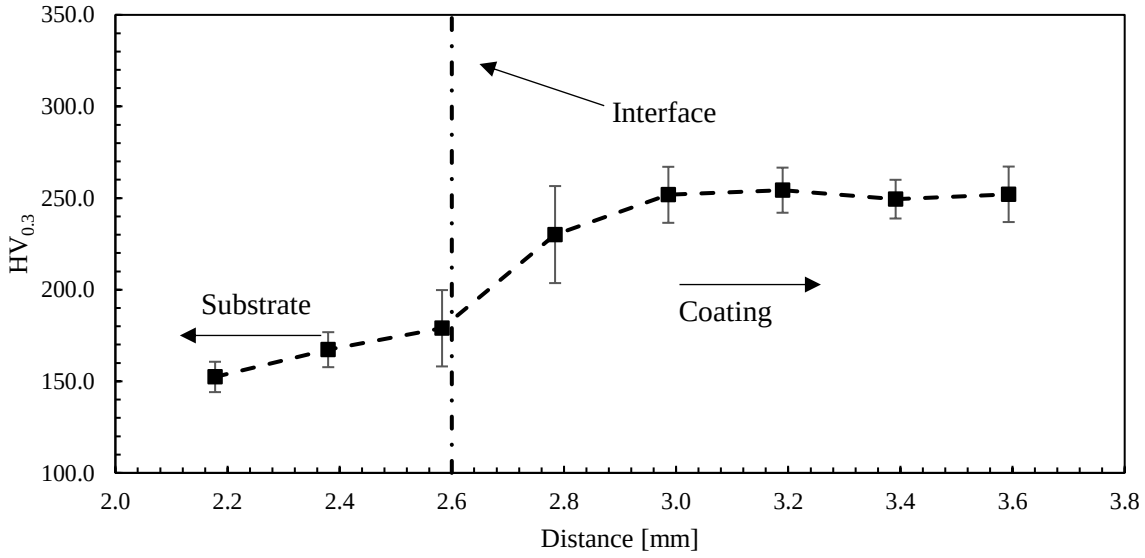

Figure 57 Microhardness profile for LC of aluminium bronze

Chapter 6 - COAXIAL LC OF TOOL STEEL ON THE BRAKE DISC

This chapter describes the LC of tool steel on full-scale GCI brake discs. The challenges encountered during LC are described, and further trials to resolve the issues faced. The optical microscopy and microhardness results are presented in this chapter.

METHODOLOGY

Figure 58 shows the uncooled full-scale brake disc used to carry out this experiment. The surface of the commercial brake disc was removed to allow a coating thickness of 150 μm.

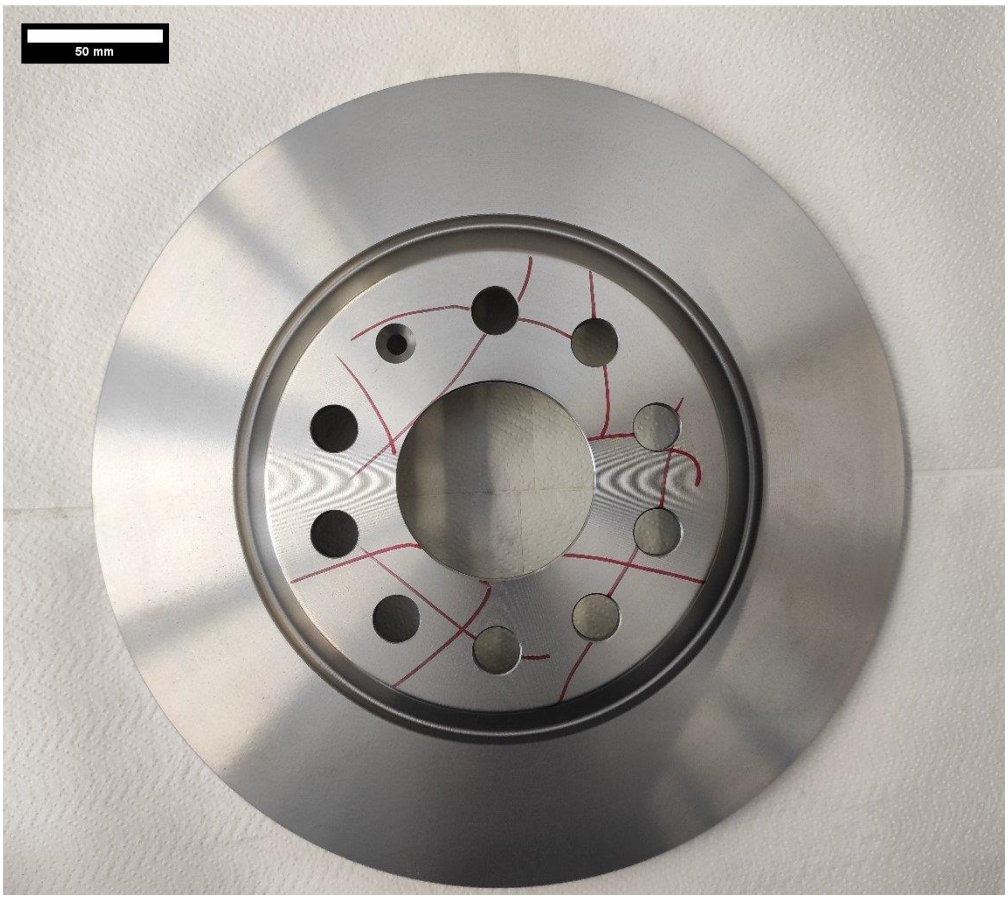

Figure 58 GCI car brake disc for LC

6.1 PROCESS PARAMETERS (PHASE-1)

Full-scale GCI brake discs were laser-cladded with tool steel. Single-clad tracks were deposited to find the optimal processing parameters suitable for the LC of GCI. The initial process parameters were selected from the knowledge gained from the two experimentations described in Chapter 3 -. A full factorial DOE was developed with the resulting processing parameter combinations as given below in the Table 22:

Table 22 Processing parameters for LC of GCI brake disc (Disc_01)

	Sample no.	Laser Power (W)	Scan Speed (mm/s)	Feed Rate (g/min)
Disc_01	1	2500	300	17.2
	2	3000	300	11.5
	3	3000	233	11.5
	4	3000	167	17.2

	5	3000	167	22.8
	6	2000	300	11.5
	7	3000	233	17.2
	8	2000	300	22.8
	9	3000	233	22.8
	10	2500	167	17.2
	11	3000	167	11.5
	12	2000	300	17.2
	13	2000	167	17.2
	14	2500	233	11.5
	15	2500	233	17.2
	16	3000	300	17.2
	17	2000	167	11.5
	18	2500	300	22.8
	19	2500	300	11.5
	20	2500	167	22.8
	21	2000	233	11.5
	22	2000	167	22.8
	23	2500	233	22.8
	24	3000	300	22.8
	25	2000	233	22.8
	26	2500	167	11.5
	27	2000	233	17.2

6.2 RESULTS AND DISCUSSION

6.2.1 DISC_01

For initial trials, one disc was utilized fully from both sides to deposit a total of 27 single-clad tracks, according to the DOE. The resulting cladded disc is shown in Figure 59.

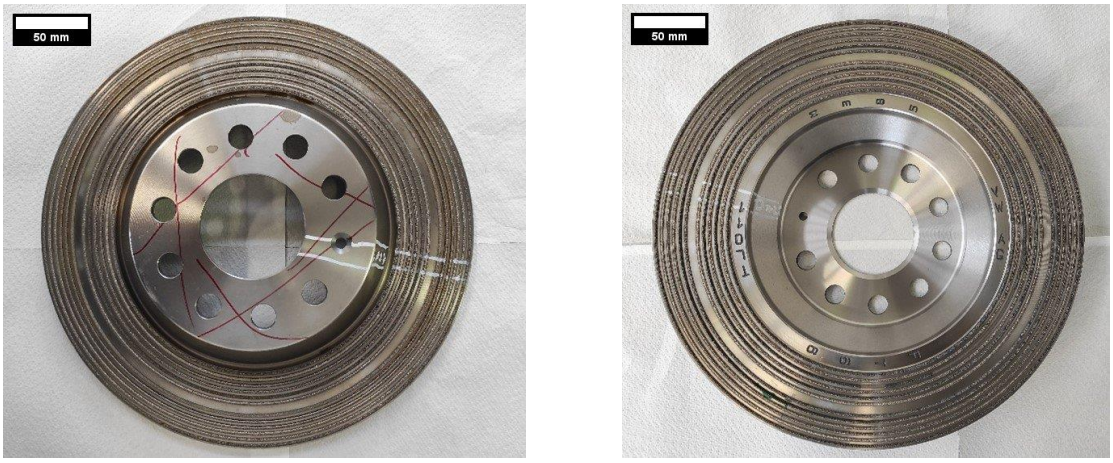

(a) (b)

Figure 59 Disc 1 LC overlayed with tool steel (a) hub side (b) flat side

6.2.1.1 ***CROSS-SECTIONAL ANALYSIS:***

EBM sectioned the disc, and metallographic samples were then prepared by mounting the specimens into resin and then polishing up to 1 μm. Figure 60. show the sectioning of discs and the resulting metallographic samples.

(a) (b)

Figure 60 Metallographic sample preparation for Disc 1 (a) sectioning (b) finished samples

6.2.1.2 Optical Microscopy

Figure 61 shows the sectional images of the clad tracks with decreasing feed rpm from bottom to top and an increasing scan speed from left to right for each specific power used. Note that the substrate was laser-cladded with no pre-treatment. At first, all single beads have visible cracks regardless of the changing process parameters. The power of 2000 W combined with all three scan speeds (167 mm/s, 233 mm/s, 300 mm/s) resulted in almost no dilution.

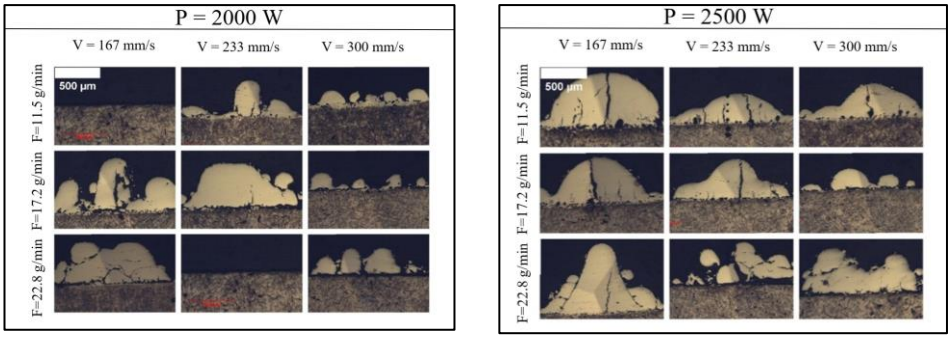

(a) (b)

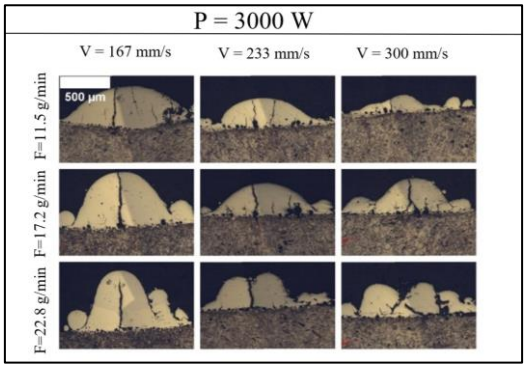

(c)

Figure 61 Cross sectional optical micrographs for coating. Scan speed (V) increase from right to left and hatch distance (HD) from top to bottom for each given power (P)

6.2.2 CRACKING SOLUTION

To overcome the issue of cracks, a further fifteen iterations were performed by preheating full-scale GCI discs.

The modified Karsays formula was used to find the Carbon Equivalent value, one criterion to determine cast iron's weldability[251].

$$CE = \%C+0.31(\%Si)+0.33(\%P)+0.45(\%S)+0.028(\%Mn)+\%Mo+\%Cr-0.02(\%Ni)-0.01(\%Cu)$$

$$CE = (3.3\%)+0.31(1.85\%)+0.028(0.75)$$

$$CE = 3.8945$$

The no-crack temperature from this CE value was found to be 360°C from the graph, devised by the American Welding Society (AWS) D11.2 code committee.

The entire disc was kept in the furnace. The time required to achieve the above temperature was calculated by creating a temperature-time curve (Figure 62) by using the Equation 9. The values used are presented in Table 23.

Equation 9

$$T = Ti + (Ta - Ti)(1 - e^{-\frac{\tau hA}{mc}})$$

Table 23 Values for calculating the temperature-time curve

Initial Temperature [T_i] (°C)	25
Ambient temperature in which the body is placed [Ta] (°C)	360
Specific Heat [c] (J/Kg °C)	440
Convection Coefficient [h] (W/m2 °C)	10
The surface area of the piece to be heated, ambient temp. An (m2)	0.1354
Mass of the body [m] (Kg)	5
Time [τ] (sec)	From 1 to 16188.9

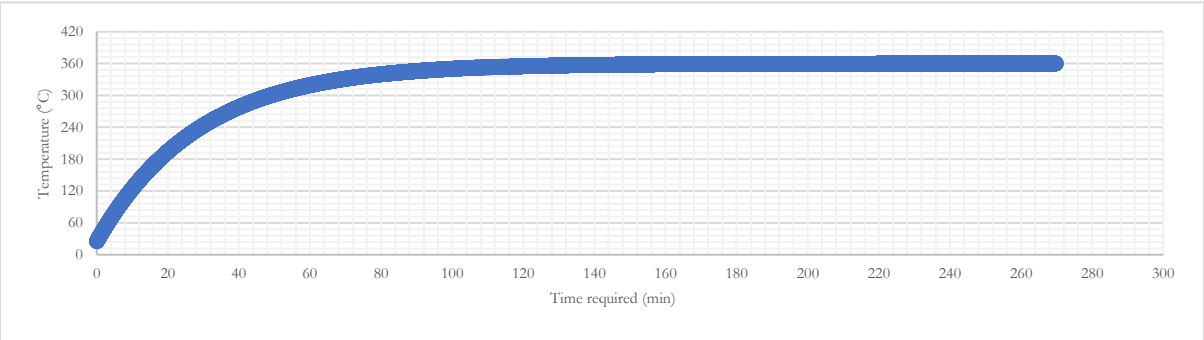

Figure 62 Temperature-time curve

The feed rate was selected from the above trials to be 17.2 g/min. For the second phase, multi-tracks were deposited with pre-heating.

6.2.3 Cross-Sectional Analysis

The resulting cladded discs (Figure 63) were sectioned and polished for optical microscopic analysis. After analysing the first two samples, the Power was reduced to 35 %. The preheating of the disc required less temperature for cladding. Table 24 presents the results for these discs.

Figure 63 From Left Disc_02, Disc_03, Disc_04 LC overlayed with tool steel

Table 24 Process parameters for LC of GCI brake discs (Disc_02, Disc_03, Disc_04)

Disc no.	Sample no.	P (W)	Scan Speed (mm/sec)	Hatch distance (mm)	no. of layers	no. of tracks
Disc_02	1	3000	233	0.5	1	5
	2	3000	167	0.5	1	5
	3	1000	233	0.7	1	5
	4	2000	233	0.7	1	5
	5	1000	167	0.7	1	8
Disc_03	6	1000	233	0.7	1	8
	7	1000	167	0.7	1	8
	8	1500	233	0.7	1	8
	9	2000	300	0.7	1	8
	10	1500	167	0.7	1	8
Disc_04	11	1000	233	0.7	2	10
	12	1000	167	0.7	2	10
	13	1000	233	0.7	3	10
	14	1000	167	0.7	3	10
	15	1000	80	0.7	1	10

6.2.3.1 Optical Microscopy

Disc_02

The optical microscopy for the five samples for Disc_02 along with the measure clad height and width (where possible) is presented from Figure 64 to Figure 68.

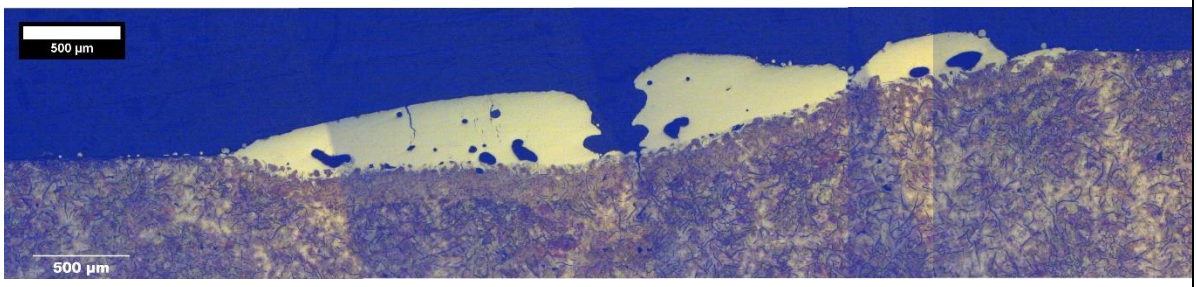

Clad Height = /	Clad Width = /

Figure 64 Disc_02 Sample 1

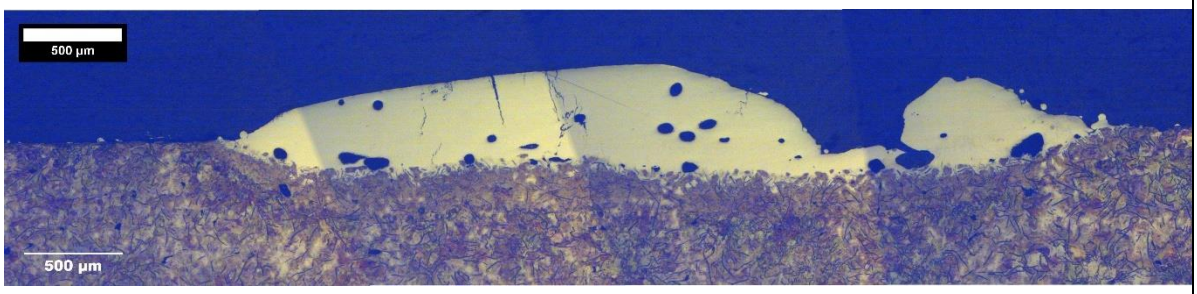

Clad Height = 0.342 mm	Clad Width = 4.5 mm

Figure 65 Disc_02 Sample 2

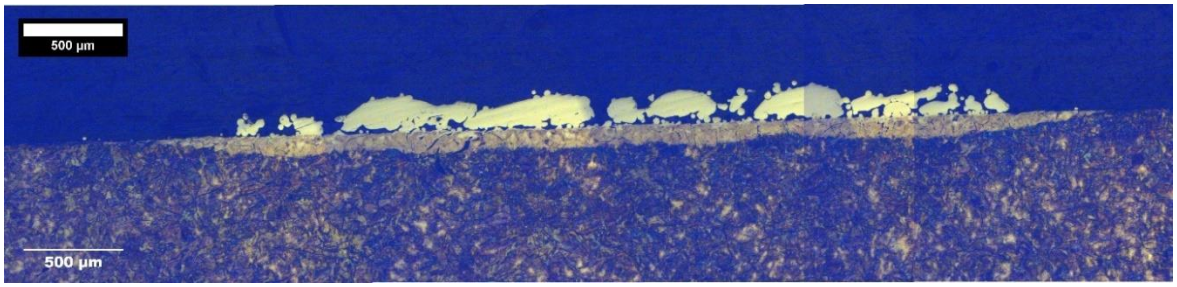

Clad Height = /	Clad Width = /

Figure 66 Disc_02 Sample 3

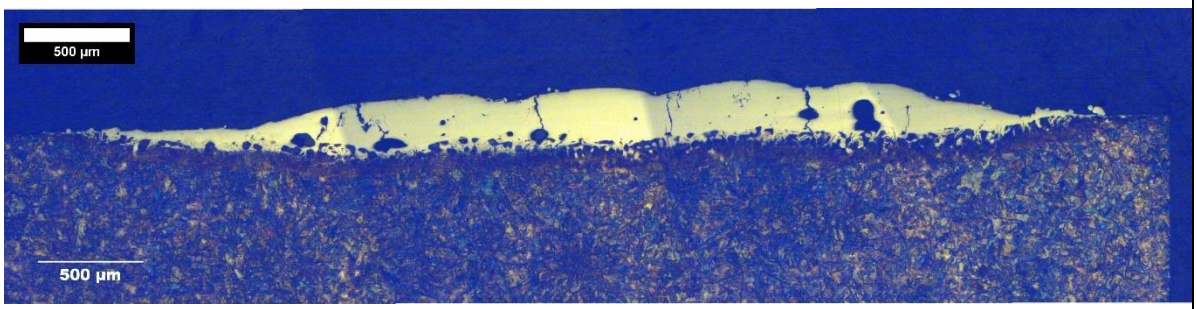

Clad Height = 0.191	Clad Width = 4.47

Figure 67 Disc_02 Sample 4

Clad Height = /	Clad Width = /

Figure 68 Disc_02 Sample 5

6.2.3.1.1 Disc_03

The optical microscopy for the five samples for Disc_02 along with the measure clad height and width (where possible) is presented from Figure 69 to Figure 73.

Clad Height = /	Clad Width = /

Figure 69 Disc_03 Sample 6

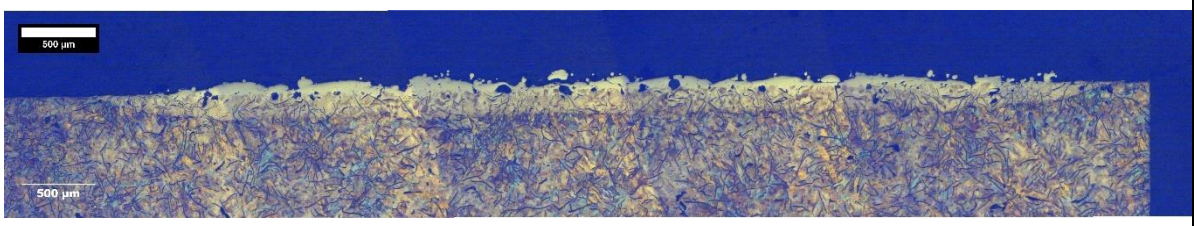

Clad Height = 0.101	Clad Width = 5.782

Figure 70 Disc_03 Sample 7

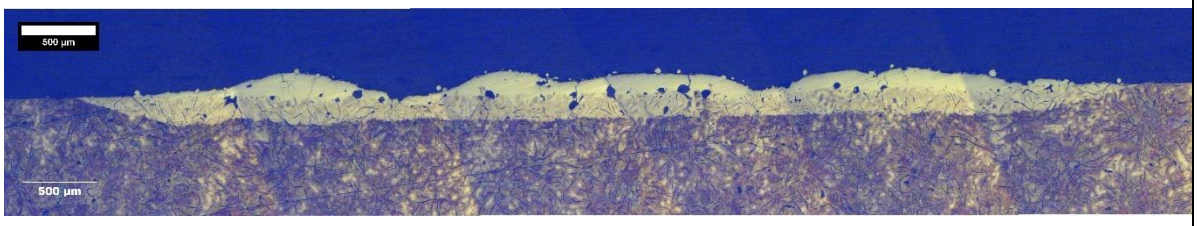

Clad Height = 0.136 mm	Clad Width = 6.854

Figure 71 Disc_03 Sample 8

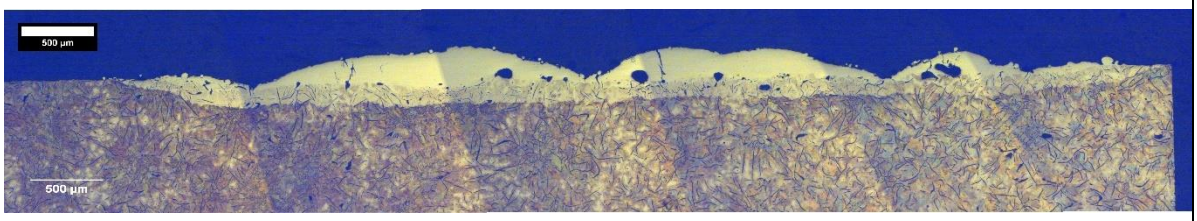

Clad Height = 0.166	Clad Width = 5.213

Figure 72 Disc_03 Sample 9

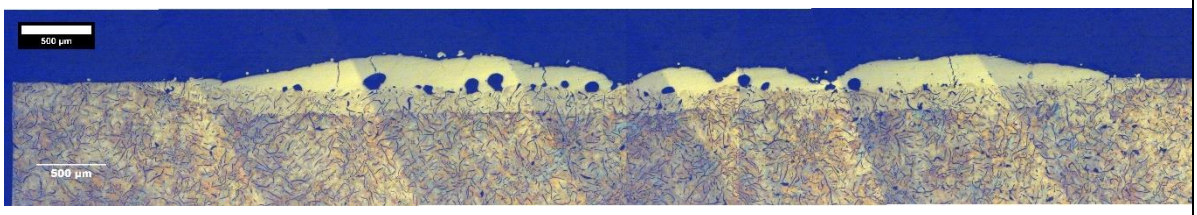

Clad Height = 0.182	Clad Width = 6.33

Figure 73 Disc_03 Sample 10

6.2.3.1.2 Disc_04

The optical microscopy for the five samples for Disc_02 along with the measure clad height and width (where possible) is presented from Figure 74 to Figure 78.

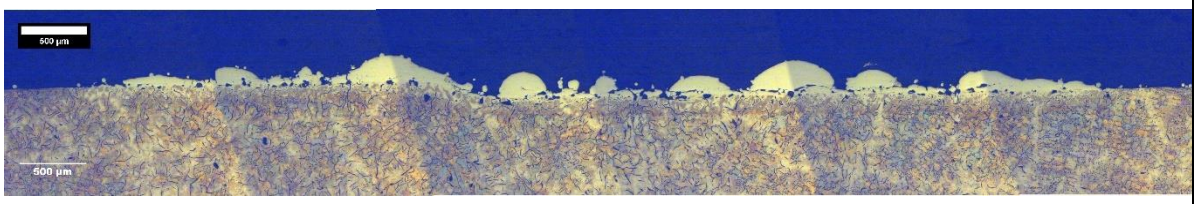

Clad Height = /	Clad Width = /

Figure 74 Disc_04 Sample 11

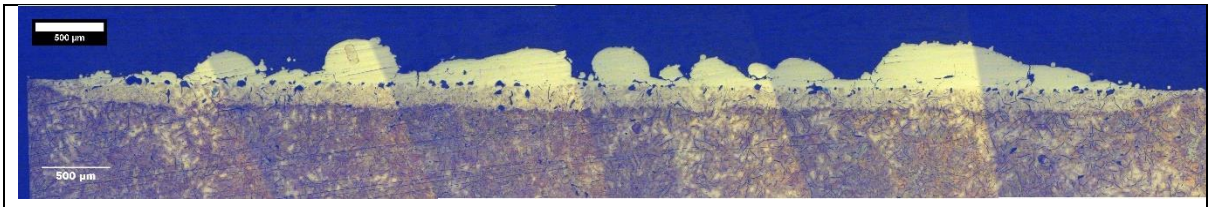

Clad Height = 0.268	Clad Width = 7.536

Figure 75 Disc_04 Sample 12

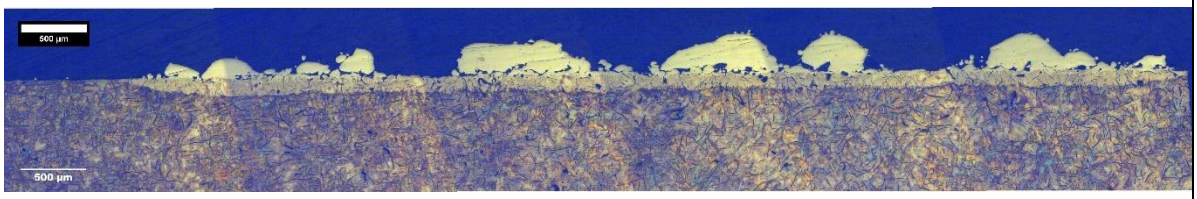

Clad Height = /	Clad Width = /

Figure 76 Disc_04 Sample 13

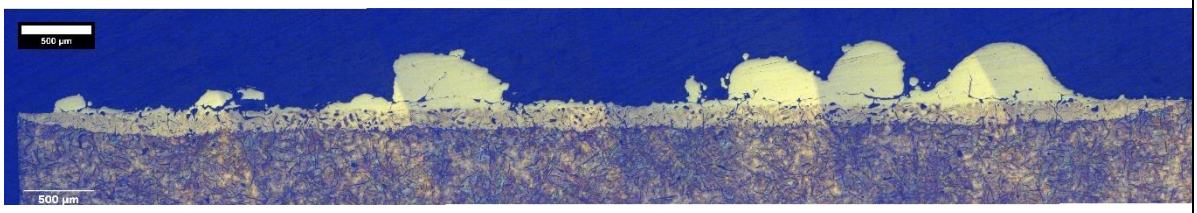

Clad Height = /	Clad Width = /

Figure 77 Disc_04 Sample 15

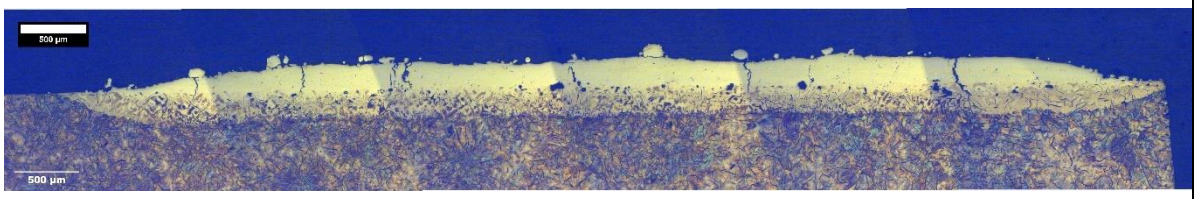

Clad Height = 0.190	Clad Width = 7.641

Figure 78 Disc_04 Sample 16

6.3 MICROHARDNESS

The microhardness tests performed on the tool steel cladded brake disc is shown in Figure 79. The coating layer had an improved microhardness value as compared to that of typical GCI brake disc.

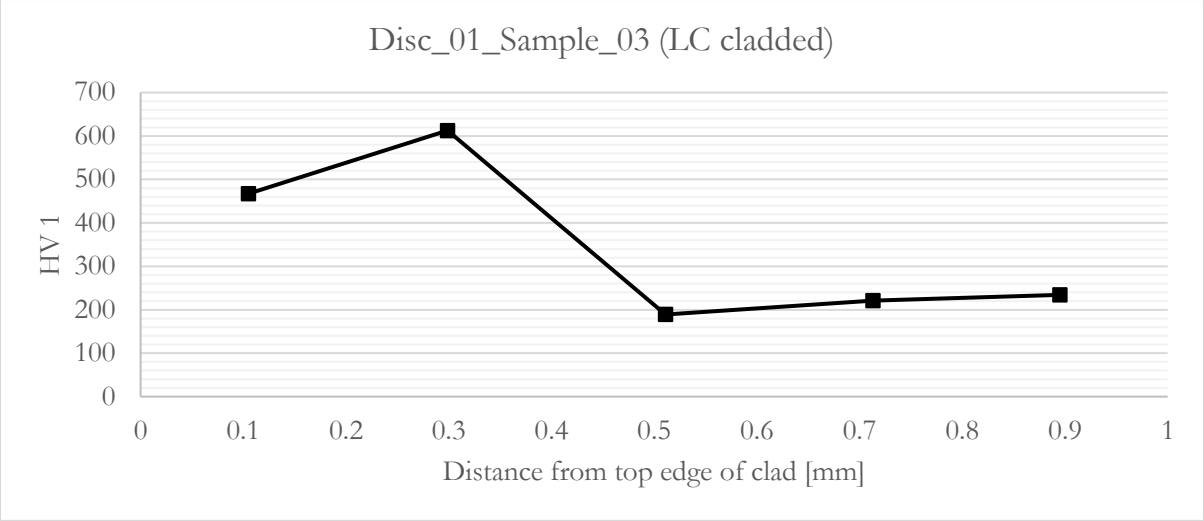

Figure 79 Microhardness of tool steel coatings on GCI brake disc

Out of the above micrographs, the (Disc_04, Sample#15) revealed desirable results with reduced porosity. The cracks are reduced but are still apparent. The full discs were laser-cladded with the following parameters. Figure 80 shows the surface of the final clad.

(a) (b)

Figure 80 GCI car brake disc fully cladded (a) hub side (b) close-up

Chapter 7 - PM EMISSION TESTS

LC has been applied mainly for repair applications along with prototyping as near-shape printing. The development of the technology has enabled it to be exploited for a severe issue of emissions from the automotive and locomotive sector. LC has recently been studied to reduce emissions from commercial cars' brake discs/brake pads. The possibility of increased state-level restrictions is forcing the manufacturers to find solutions to reduce NE emissions. These targeted PM for the brake disc/brake pad mainly involved PM2.5 and PM10 as a starter. LC has been somewhat beneficial in achieving this and has seen an increase in patents of LC for such applications.

The NE emissions is also of great concern in the underground train platforms. Other methods such as water cleaning has not proved to be an effective solution. The toxicity of such PM requires alternative solutions to be researched and developed as soon as possible.

This chapter focuses on the studying the PM emissions from automotive brake disc and from rail-wheel contact (locomotive). GCI brake disc against Cu-free pads were tested in lab environment with varying test conditions. This verifies the PM emission from such contact as well as the response of emissions to varying test conditions in lab environment. The early-stage emission results from tool steel cladded brake disc reported to have reduced PM 10 emissions. The PM emissions from rail-wheel contact were studied on a nanometric scale. Two types of LC overlayed discs were used to study such emissions. The implementation in real scenarios is backed with the friction and wear results.

7.1 LAB TESTS FOR COMMERCIAL BRAKE DISC / CU-FREE PAD

7.1.1 METHODOLOGY

At first, the experiments were performed on the dedicated pin-on-disc tribometer to verify the PM emission from the commercial brake disc / Cu-free pads and their response towards varying test conditions. This chamber was connected to a Dekati Gravimetric Impactor (DGI) and Dekati Electrical Low-Pressure Impactor (ELPI+). The DGI had four stages with 47 mm aluminium filters. The end of DGI had a 70 mm PTFE filter. For ELPI+, 25 mm polycarbonate filters were used for stages 1-5 and aluminium filters for the rest of the stages. The reason for using PTFE filters at the end of DGI is that it is easier for the toxic analysis group to extract the particles than other filters. Similarly, polycarbonate filters on ELPI+ stage 1-5 because of the convenience for the chemical analysis group. The aluminium filters are standard filters used for both devices.

The cylindrical pins of 10 mm diameter were cut out from the commercial Cu-free brake pads. The GCI discs of diameter 50 mm were cut from the commercially used car brake disc. Twelve different test conditions were tested by varying sliding speed and contact pressure. The sliding distance for all the tests was kept at 7200 m. Table 25 presents the parameters for each test.

Table 25 Parameters for pin on disc emission tests of GCI brake disc

Test no.	Room Temperature (°C)	Relative humidity (%)	Sliding speed (m/sec)	Contact pressure (MPa)	Applied dead load (Kg)	RPM
1	23.7	59	1.0	0.3	1.2	531
2	24.7	64	3.0	1.2	4.7	1592
3	24.3	60	1.0	1.2	4.7	503
4	23.2	52	1.0	1.2	4.7	503
5	24.0	57	3.0	0.3	1.2	1508
6	21.4	51	4.0	0.6	2.3	2010
7	22.7	47	4.0	0.8	3.1	2010
8	20.9	52	1.0	0.6	2.3	503
9	20.3	54	3.0	0.8	3.1	1508
10	21.8	51	3.2	1.0	3.9	1608
11	21.5	48	4.0	1.2	4.7	2010
12	22.9	57	3	1.1	3.9	1659

(a)

Figure 81 Lab scale GCI brake disc / Cu free pad for emission tests

7.1.2 Results and Discussion

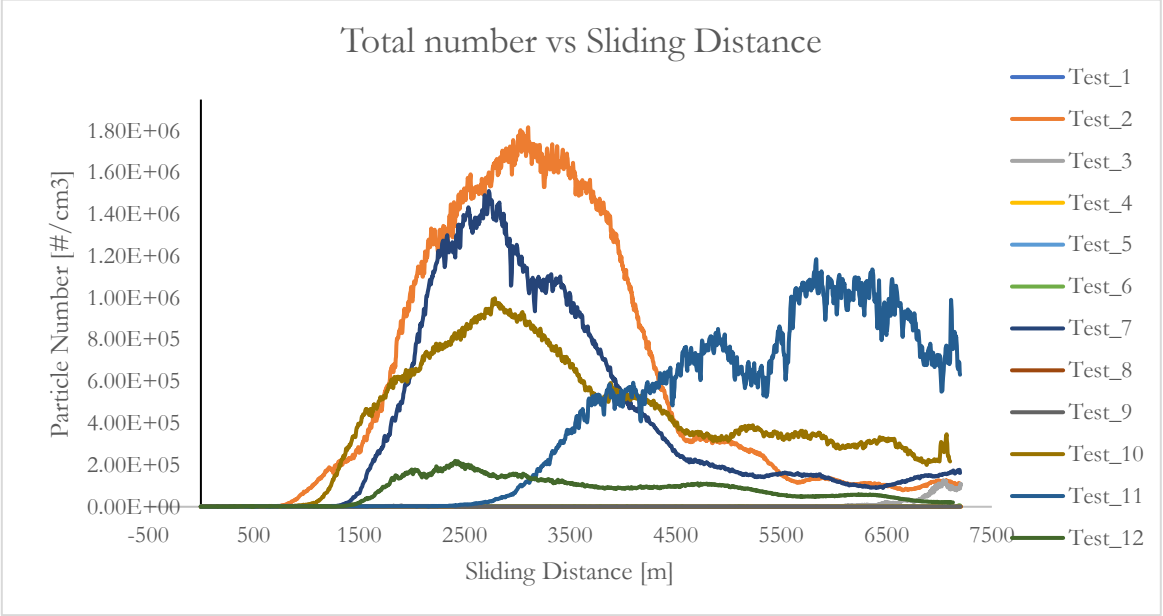

Figure 82 Lab emission result from commercial GCI brake disc / Cu free pad

The measured particle number concentration and particle size distribution for all the test combinations for commercial GCI brake discs against Cu-free pad are presented in Figure 82 and Figure 83 respectively. Airborne particles were generated for almost all the tested contact conditions. This generation trend, however, varies in terms of the first occurrence and number concentration which is evident from the peaks of the graph. The generated airborne particle concentration tends to show a drastic increase closer to the start of the test after the running in phase and then continues to decrease with sliding distance. Out of the

tested conditions, it can be confirmed that test two resulted in the most particulate matter emissions. These parameters were found to result in equivalent results when the test was repeated three times. For most of the tested conditions, the particle size distribution ranged from 10 – 100 nm.

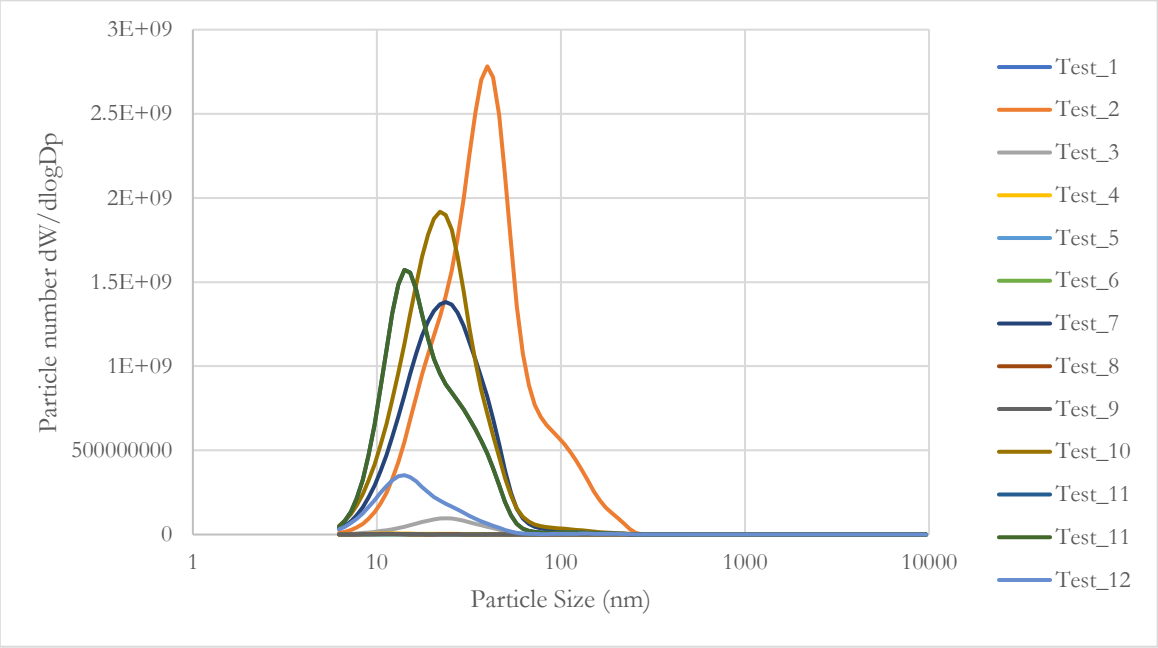

Figure 83 Size distribution of emissions from commercial GCI brake disc / Cu free pad

The PM emissions form the tool steel cladded brake discs were carried out from an external source. The early results revealed a substantial amount of reduction in PM 10 emissions as well almost negligible wear rate.

7.2 LAB SIMULATION OF RAIL-WHEEL CONTACT

7.2.1 METHODOLOGY

The tests were performed on the dedicated pin-on-disc tribometer connected to Dekati ELPI+.

Four tests were run for each of the following pin/disc combinations except for Case-1, which was repeated three times. The LC was outsourced.

- Case-1 – UIC60 900A rail pin against R7 wheel disc.
- Case-2 – UIC60 900A rail pin against R7 wheel disc LC with Ni-based powder alloy containing 8% manganese sulphide (MnS).
- Case-3 – UIC60 900A rail pin against R7 wheel disc LC with 316L stainless steel.

An ultrasonic bath cleaned the specimens in isopropanol for 15 minutes. Laser-cladded discs were carefully cleaned with wipes dipped into isopropanol. The force of 60 N was calculated by Hertzian contact theory[252] to simulate the train's contact pressure of 0.3 GPa. The sliding velocity corresponds to the

sliding wheel-rail contact's extreme contact situation to break in sharp curves. The material properties of discs and pins are listed in the Table 26.

Table 26 Properties of test specimens for pin on disc emission tests of rail-wheel contact

	Case-1	Case-2	Case-3
ID	Standard railway carbon steel	LC self-lubricating overlay	LC stainless steel overlay
pin	UIC60 900A rail steel, 0.6..0.8 C, Rm = 880..1030 MPa, A5≥10%. EN13674-1. Hardness 24 HRC (measured), ISO 21290 average roughness Ra ≈ 0.25 μm		
Disc material	R7 wheel steel UIC standard 812-3 (ER7 EN13262), C ≤ 0.52, Rm= 820..940 MPa, A≥14%.	LC overlay with Ni-based powder alloy containing 8% manganese sulphide (MnS)[236] disc substrate steel EN S235JR.	LC overlay with martensitic stainless steel powder alloy Rockit 401, Fe-0.15C-18Cr-0.5Mo-2.5N-<3 other (Höganäs AB), disc substrate steel EN S235JR.
Disc surface roughness Ra (μm)	0.2	0.2	0.5
Disc hardness (HRC)	30	41*	51
* Hardness is biased with MnS-addition – the indenter penetration is lubricated.			

The particle concentration was tested at the inlet and outlet. The system was set to run for 10 minutes without any contact to ensure zero particle concentration. The temperature and relative humidity varied from 20±1 °C and 33±1 %, respectively.

The tangential force was measured using an HBM® Z6FC3/20 kg load cell (non-linearity of 0.1% of the full-scale output). The coefficient of friction is then determined by dividing this measurement by the applied load.

The mass loss for specimens was measured before and after the test to the nearest 0.1 mg. SARTORIUS® ME614S and METTLER TOLEDO XP2003S were used for this measurement for pin and disc specimens, respectively. Specific wear rate k could then be determined by using Equation 10[222].

Equation 10

$$k = \frac{\Delta m}{\rho \cdot \Delta s \cdot F_N}$$

Where Δm is the mass loss of the specimen, ρ *is the* specimen's density (7.58 g/cm^3), Δs is the total sliding distance, and F_N is the normal load applied to the pin.

7.2.2 Results and Discussion

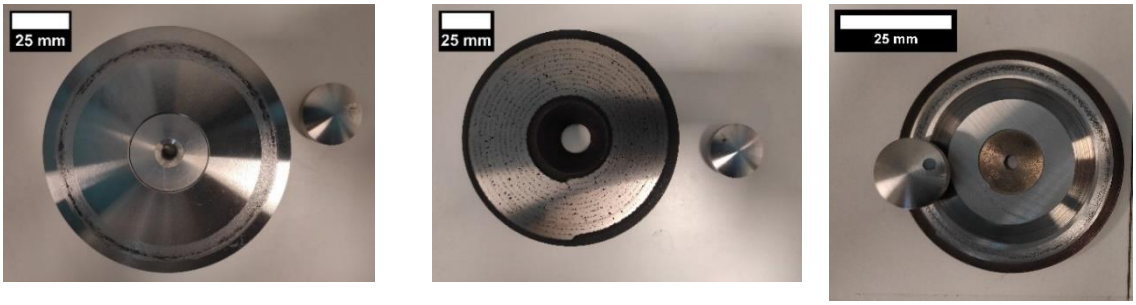

(a) (b) (c)

Figure 84 Rail-wheel emission test samples (a) Case 1 (b) Case 2 (c) Case 3

7.2.2.1 Friction

Figure 85 shows the coefficient of friction (CoF) for each case against the sliding distance. The values of the CoF from this experiment are within the acceptable limits for rail-wheel contact. For Case-1 and Case-3, the value of CoF is relatively stable and ranges between 0.44 – 0.52. For Case-2, it increases slightly over the sliding distance with a maximum value of 0.28 and an average value of 0.23 from all repititions. This agrees with the acceptable values for such contact. Since the accelration and braking usually require a CoF of about 0.2. The value of CoF is significant for this type of contact due to safety and performance reasons. An improper value can cause poor adhesin during braking, lead to extended stopping distance, and affect traction[253]. For Case-3, this value is averaged at 0.51, which is quite like the range reported in another research[254]. A CoF value above 0.4 is suggested to increase the chance of wheel and rails surface fatigue[253]. Therefore, in terms of CoF values, Case-2 yielded better results.

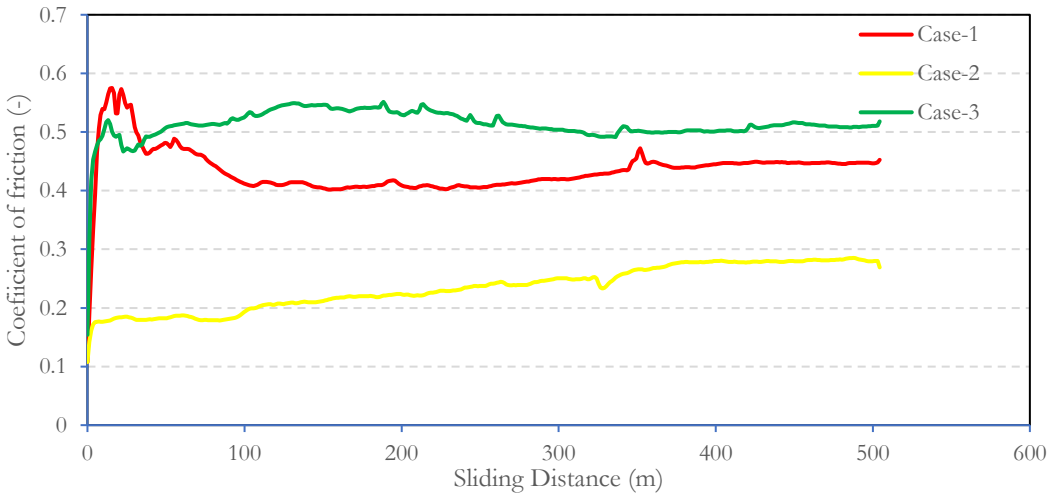

Figure 85 Coefficient of friction against total sliding distance for rail-wheel contact

7.2.2.2 Wear

The mass loss for both pin and disc are presented as box and whiskers plot in Figure 86. For Case-1, standard railway steels, both pin and disc mass loss are relatively high for both pin and disc. The disc mass loss for Case-2 and Case-3, with LC self-lubricating respective LC stainless steel overlay, are very similar, whereas pin mass loss for Case-3 is more than as of Case-2 but like Case-1. This trend is also illustrated by the specific wear rate for discs and pins. For Case-3, the material composition of LC stainless steel overlay has a few times lower thermal diffusivity than carbon steel, and it likely increases the contact temperature. The COF here is slightly higher than Case-1 with standard railway carbon steels. For Case-2, the LC self-lubricating overlay has a material composition that, without MnS, should also have a thermal diffusion coefficient a few times lower than for Case-1 with standard railway carbon steels. However, the presence of 8% MnS-solid lubricant drops the COF to 0.22-level, which for sure drops the contact temperature.

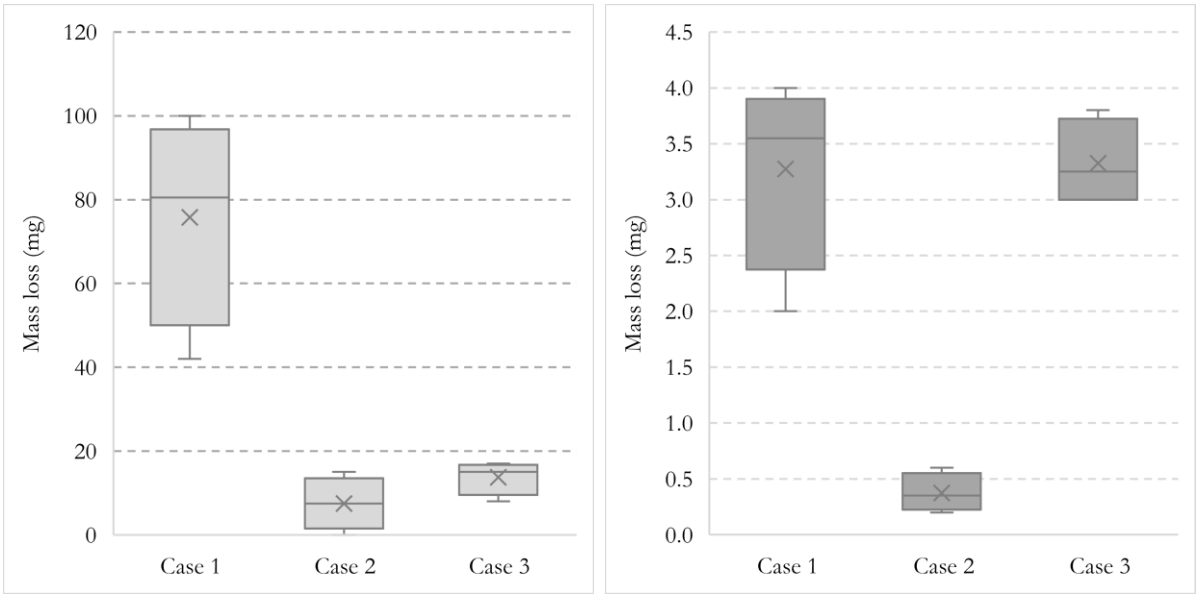

(a) (b)

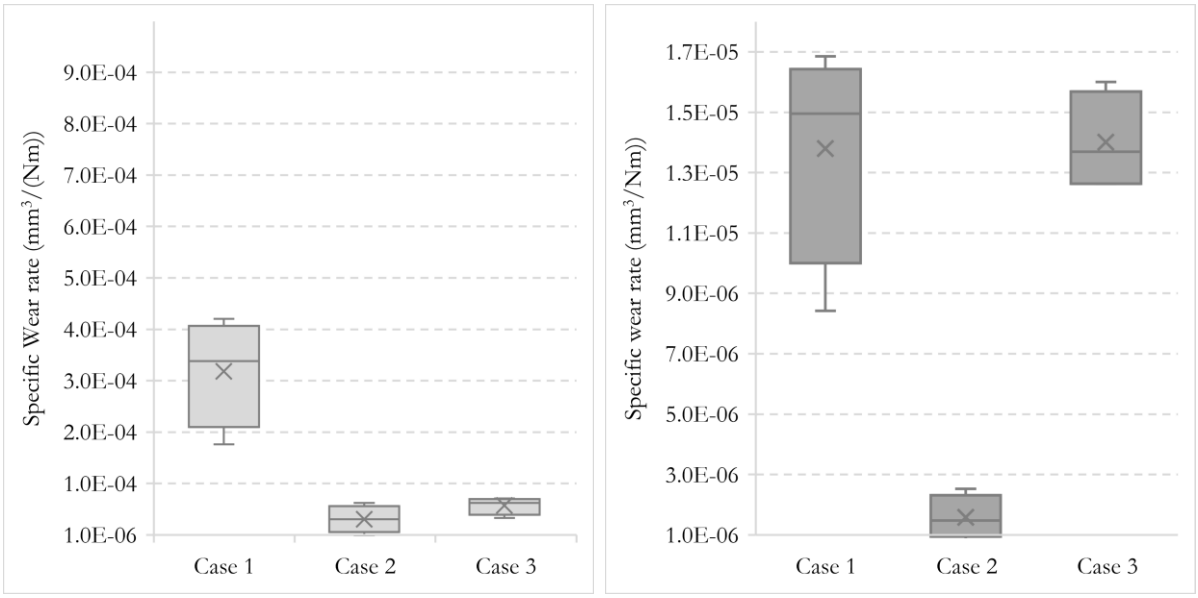

(c) (d)

Figure 86 Rail wheel contact (a) Disc mass loss (b) pin mass loss (c) disc specific wear rate (d) pin specific wear rate

7.2.2.3 SEM Analysis

The pin and disc-worn surfaces for all the cases were observed using the SEM (Figure 87, Figure 88). For Case-2, the wear track is much narrower, smooth, and with relatively less occurrence of flakes.

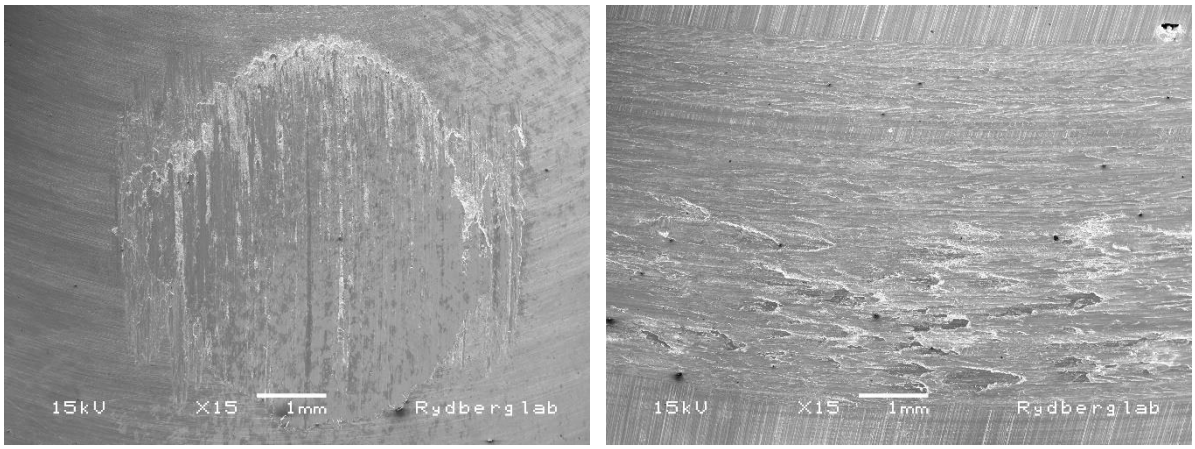

Case-1 – standards railway carbon steels

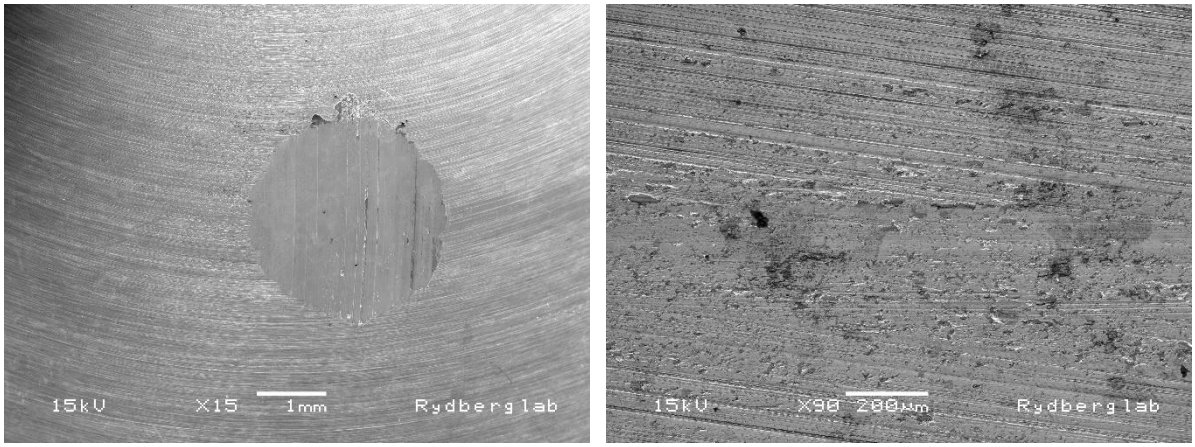

Case-2 – self-lubricating LC overlay.

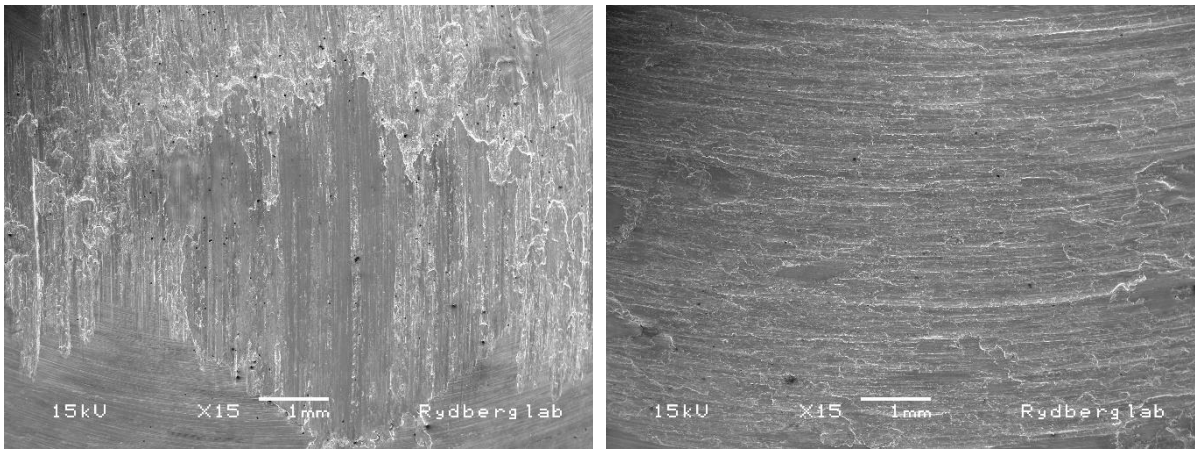

Case-3 – stainless steel LC overlay.

Figure 87 Wear track appearance for rail wheel contact (scale 15x)

Figure 88 shows the images of worn surfaces for both pins and discs. Transferred worn material in the form of wear flakes can be observed for both Case-1 and Case-3. This depicts the evidence of sliding adhesive wear. This phenomenon on the sliding wear marks is relatively less severe for the disc overlayed with stainless steel, i.e., for Case-3. The surface of Case 2, however, shows an entirely different trend. The wear marks can be seen without any wear, transferred material in the form of flakes. Also, this appearance suggests the presence of lubrication which in this case was due to the solid film lubrication with MnS. The generated air-borne particles correspond with the SEM analysis of the worn surfaces of both pin and discs for all the cases.

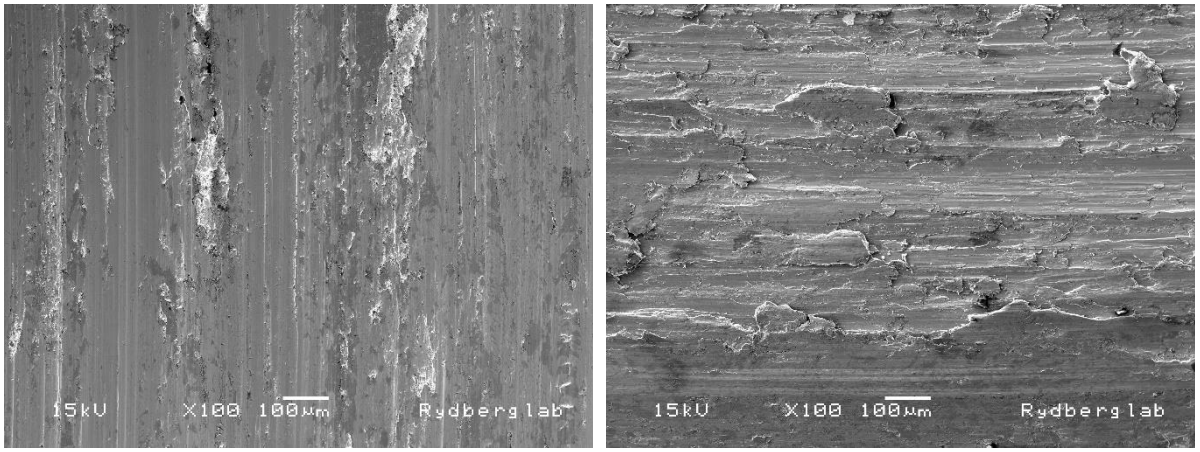

Case-1 – standards railway carbon steels

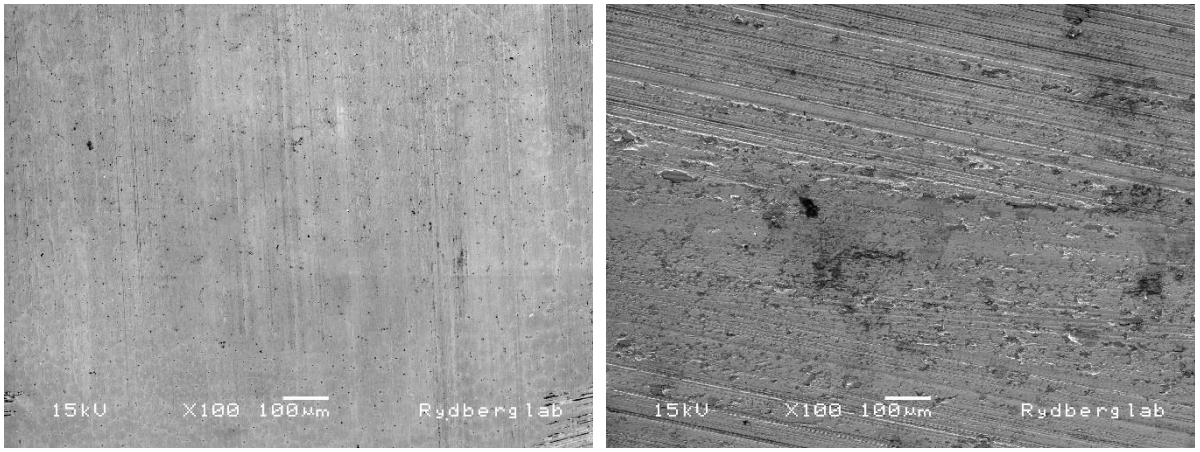

Case-2 – self-lubricating LC overlay.

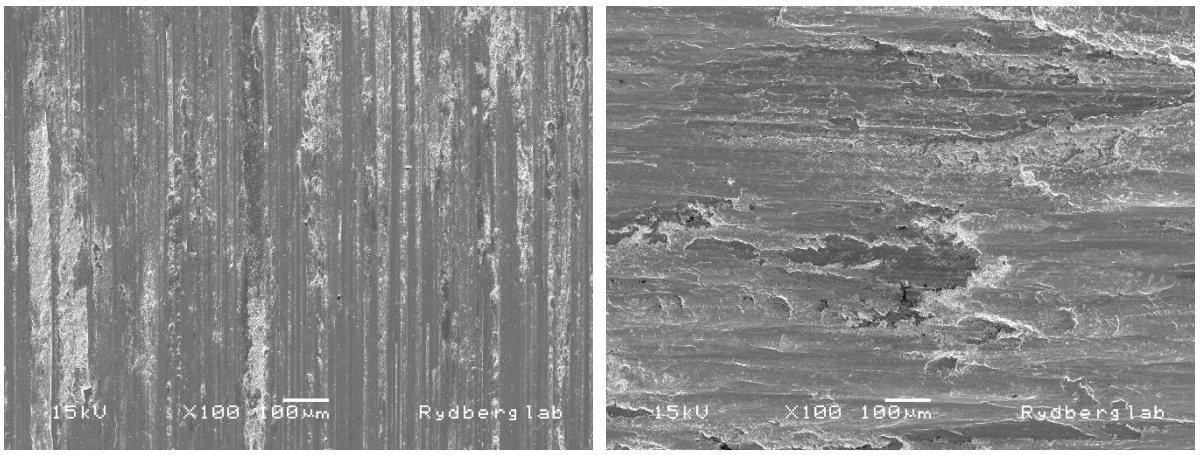

Case-3 – stainless steel LC overlay.

Figure 88 Wear track appearance for rail wheel contact (scale 100x)

7.2.2.4 Particle Emission Parameters

Figure 89 shows the total particle number against sliding distance for all repetitions performed for each case. The particle emissions for Case-2 and Case-3 seem to be similar, and for Case-1, a completely different trend can be observed. The PM emissions were almost negligible when one of the pearlitic steels (rail/wheel) was laser-cladded with Ni-based powder of martensitic stainless steel.

For Case-1 all the three curves appear to stabilize after about 500 m of sliding distance at 10^2 particles/cm^3. The main difference lies in the path for this stabilisation. For standard carbon railway steels, this particle number starts from 10^4 particles/cm^3 and linearly decreases to 10^2 cm^3 after about 350 m. For Case-2, LC overlayed self-lubricating disc, the particle number all-time remains unchanged and stays stable at 10^2 cm^3. The LC overlayed stainless-steel disc shows almost a similar trend to Case-2, and the particle number starts at slightly below 10^3 particles/cm^3 but reaches the particle number level of 10^2 particles/cm^3 after about 100 m.

The experiment confirms that dry wheel-rail contact emits air-borne particles, which is previously reported[255-257]. [255] reported that the generated air-borne particle size varies with the sliding velocity, and 90 % of such particles were found to have an aerodynamic diameter of less than 0.1 µm. The former is in complete agreement with the present study. An increase in the ultra-fine particles was also confirmed by another study[256] performed on a twin-disc rig that simulated both rolling/sliding and pure sliding[ref252]. When a similar test setup was used to simulate higher train velocities, [257]found that the generated ultra-fine particles were higher than the generated micro-particles, this increased particle emission can be linked to the study of [255] in which sliding velocity in dry sliding wheel-rail contact was found to be the critical factor in affecting the wear rate and particle emissions. Further, the particles were generated during the running-in period.

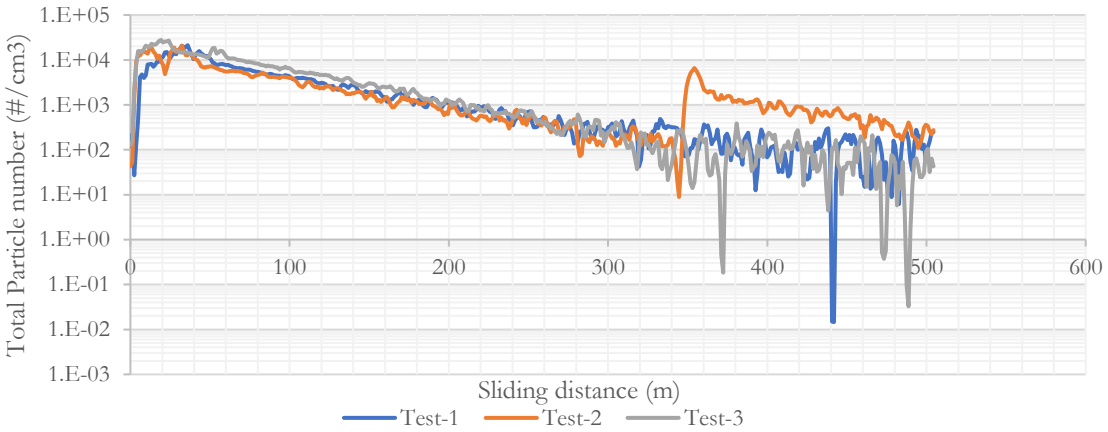

(a)

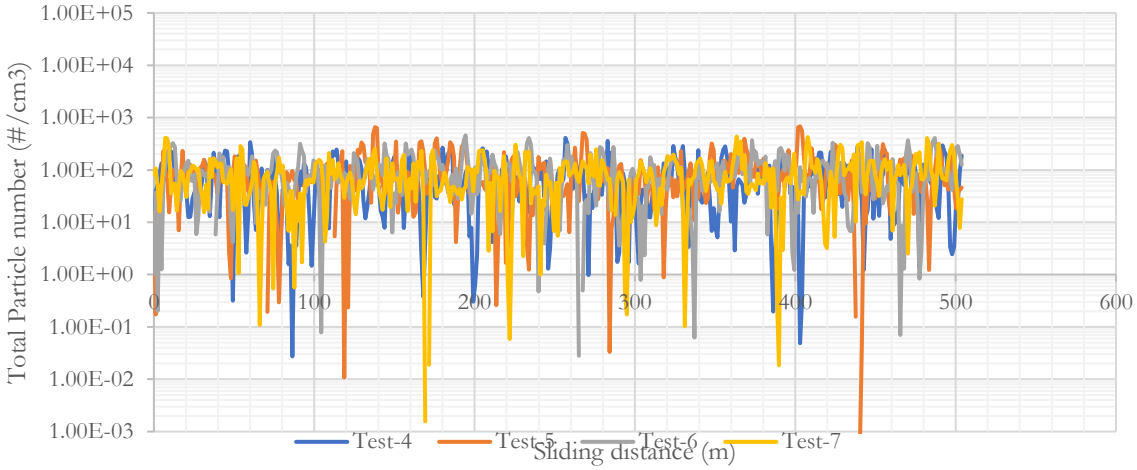

(b)

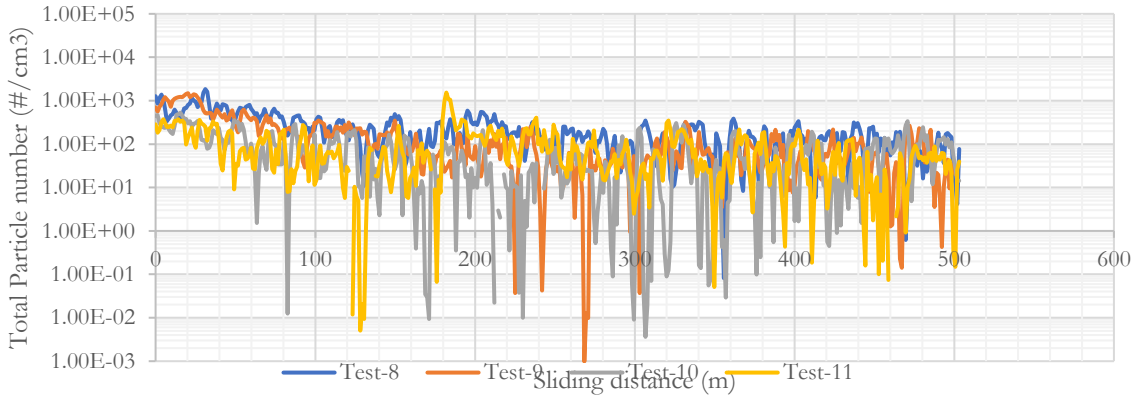

(c)

Figure 89 Total particle number for rail-wheel contact on logarithmic scale (a) Case-1 (b) Case-2 (c) Case-3

7.2.2.5 Size Distribution

The particle size distribution graph is shown in Figure 90. The particles emitted are in the ultra-fine range, i.e., from 6 nm to 0.1 μm for all three cases. The generation of ultra-fine particles for such contact type was closely related to the contact temperature in previous studies[258]. It was reported to result from a thermal rather than a mechanical process. Oxidative wear was previously reported to result from the generation of particles in such a size range. Oxidative wear is a sliding wear mechanism that does not occur under lubricated conditions and is more common in metals than other materials due to its chemical process. In the present study, the SEM analysis does not show any sign of oxide layers but shows evidence of adhesive wear. A plausible argument could be that probably the temperature required to reach the oxidative could not have been reached under the given conditions. For Case-2, the contact surface appeared to be smooth. This could be due to the presence of solid lubricant MnS. The reduction of particle emissions for Case-2 and Case-3 could be likely from the reduced wear rate.

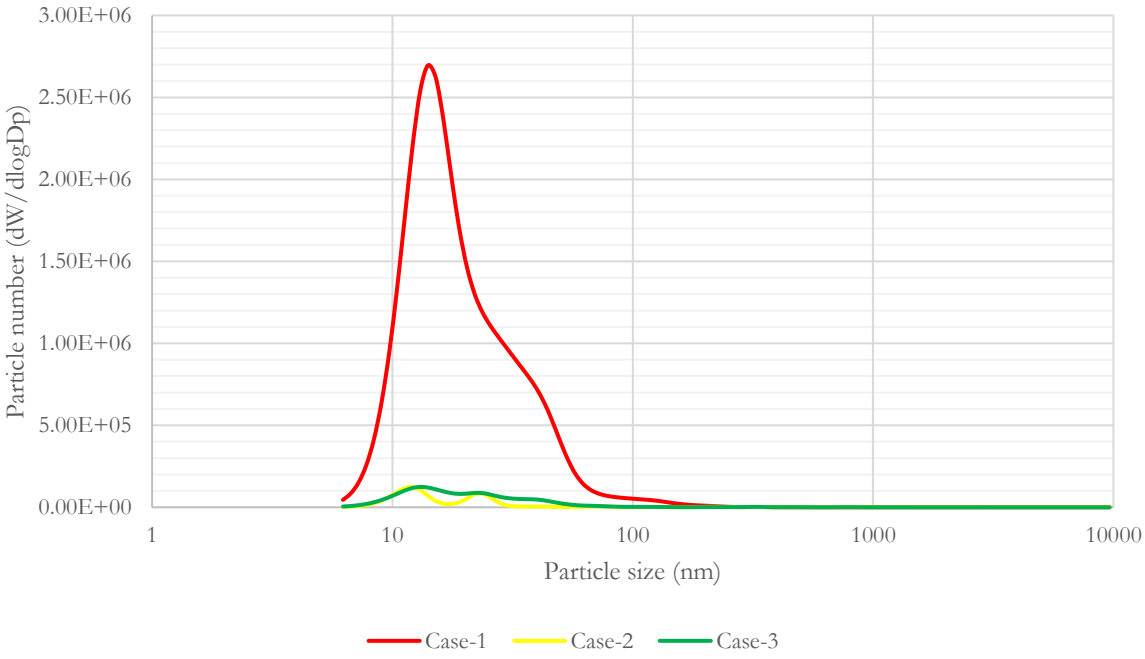

Figure 90 Normalised particle size distribution for rail-wheel contact for all three cases

The particles emitted for Case-1 were further studied by plotting only ultra-fine emitted particles against sliding distance. This is shown in Figure 91. It can be observed that this graph shows identical results as shown for particle size ranging from 6 nm to 10 µm. This is due to the reason that almost all the particles emitted were in the ultra-fine range.

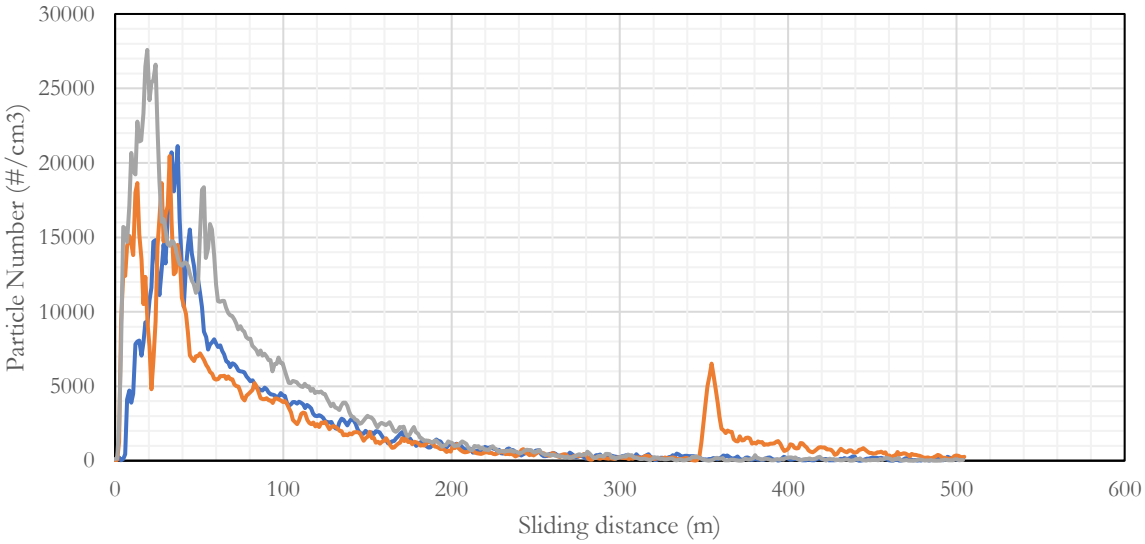

Figure 91 Ultrafine particles for Case-1 of rail-wheel contact

Chapter 8 - FINAL CONCLUSIONS AND RECOMMENDATIONS FOR FURTHER RESEARCH

This research focused on controlling the parameters of coaxial LC technology and its applicability for reducing NE emissions. The aim of the research was successfully fulfilled from the set objectives.

This chapter contains the main conclusions drawn from all the experiments and recommendations for future research.

8.1 OVERVIEW:

The purpose of the present PhD work was to evaluate the LC technology and further test its applicability to reduce harmful PM emissions from the automotive and locomotive sector.

The LC process was evaluated by performing multi-layer and multi-track deposits of 316L stainless steel and aluminium bronze onto rectangular and circular substrates. LC could also be applied for near-net shape fabrication and it requires multiple deposits of layers. The major hindrance in achieving this goal is geometric distortion. Therefore the effect of the scan strategy for depositing geometrically sound thin-walled 316L stainless steel deposits was studied when coupled with a recently developed commercial closed-loop control system.

Controlling the combined effect of process parameters is another major challenge for the successful implementation of LC technology. Usually, a single track is not enough, and multiple tracks are needed to be overlapped to coat a part fully. Multi-track deposits of aluminium bronze were carried out onto a circular structural steel substrate. Combined parameters capable of controlling a specific geometric characteristic were developed statistically.

Automotive GCI brake discs are being laser cladded to reduce the harmful PM emissions. Industries are looking for immediate solutions as NE regulations from EU are getting stricker. Most LC of GCI brake disc are carried out with metallic powders that contain heavy metals. Therefore, more often this could counter react by emitting much harmful particles from the brake pad / brake disc contact. Tool steel was selected since the material compostion is almost free from heavy metals (only small fraction of chromium) at the same time possess improved hardness values. The commercial GCI brake discs were laser cladded with tool steel without the use of an intermediate layer. The results from the emission tests show a substantial decrease of PM10 emissions as well as almost negligle wear rate as compare to the commercial materials contact.

A very few recent studies claimed that a substational amount of air-borne particles were found at the underground rail platforms. Efforts are currently being made such as the separating platforms via glass barriers, application of friction modifiers, water blast cleaning etc. The former methods, however failed to reduce the concentration of the air-borne particles. A lab simulation of extreme contact conditions of rail wheel contact were performed in the lab enviorment and the resulting particle concentration and size distribution was studied. Contact of laser cladded wheels with two different types of metallic powders were studied and results were compared to the commercial rail-wheel contact. The applicability of LC for reducing PM emissions from rail-wheel contact was further backed from the Coefficient of friction results and the SEM analysis of the wear tracks.

A specific conclusion from each of the studies performed is given.

8.2 MULTILAYER LC OF STAINLESS STEEL:

Controlling the final deposit's geometry was challenging in LC, especially when fabricating thin-walled structures. The closed-loop control system capable of controlling melt pool width by altering the laser power in real-time was found to be effective only when coupled with the correct scan strategy. Out of the two scan strategies, i.e., bi-directional and unidirectional, only bi-directional yielded a geometrically consistent wall. The use of constant power was not able to fabricate thin-walled structures. However, the use of a closed-loop control system seemed to minorly affect the final density of the part as the number of pores increased. The microhardness analysis revealed that the closed-loop control system had no significant effect even when a low power of 600 W was fed. The microhardness of the dilution zone was found to be more than that of the actual deposited wall and almost stays similar over the height of the wall.

8.3 MULTITRACK LC OF ALUMINIUM BRONZE:

The absence of cracks revealed that aluminium bronze can be cladded to structural steel pipes with an appropriate selection of process parameters. From the varied parameters (laser power, scan speed, hatch distance) for this experimental study, it can be concluded that laser power was found to have a negligible effect on controlling the height of the clad. The clad height was mostly governed by hatch distance and scan speed. The combined effect of the selected parameters on the height of the clad could then be written as $V^{-1.5}.HD^{-1.1}$. The width of the clad and the percentage dilution analysis depended on all three parameters under consideration for this study. Hatch distance was found to be the most critical governing factor for the width, whereas scan speed and hatch distance were both found to be the critical factors for the percentage of dilution. The resulting combined parameter controlling the clad's width and dilution percentage could then be written as $P^{2/5}.V^{1/4}.HD^{1}$ and $P^{1.1}.V^{1.25}.HD^{1.2}$. The microhardness of the coated samples was found to be more than the typically used value for aluminium bronze.

8.4 LC OF TOOL STEEL ON GCI BRAKE DISC:

GCI brake discs could not be effectively laser-cladded by tool steel without preheating grey cast iron to temperatures of at least 300 – 400 C. The former is true regardless of varying the process parameters of LC. Even on the preheated substrates, cracks were seen that originated from the substrate towards the coating.

8.5 PM EMISSION TESTS:

Simulation of various braking conditions in the lab revealed that commercial GCI brake discs emit particles when tested against Cu-free brake pads. Both the concentration and size distribution of these particles were found to be dependent on the test conditions. A significant number of both PM 2.5 and PM 10 resulted when the tests were carried out in lab conditions.

The use of LC overlayed brake disc with tool steel claimed to reduce these particles and resulted in almost negligible wear and reduced PM10 emissions.

The simulation rail-wheel contact in extreme conditions revealed that a substantial number of airborne particles were generated with a commercially used material of rails UIC60 900A and R7 wheels (Case-1). Ultrafine particles were generated at the tested conditions. For the commercially used materials, a running distance was required, after which the particle curves appeared to be stabilised. The emitted particles peaked at the beginning at 400 and then finally reached 200 particles/cm^3 after about 350 m of sliding distance. These airborne particle generations were almost negligible when LC overlayed wheels were used instead. Both for LC overlayed Ni-based powder with 8 % MnS (Case-2) and martensitic stainless-steel powder (Case-3). For Case-2, the peak starts at 300 particles/cm^3 and reaches 200 particles/cm^3 and running in distance of 200 m, whereas, for Case-3, the airborne particle emission stayed at a constant level of 200 particles/cm^3 throughout the sliding distance. The use of LC overlay thus reduced the number of airborne wear particles in the sub-100 nm range by more than a factor of 10. The coefficient of friction values for Case-1 was measured to be 0.43, for Case-2 0.51 and for Case-3 0.23. The specific wear rate for LC overlayed test discs was at a level of 10^{-5} mm^3/Nm, which accounted for almost one ten power lower than for the R7 wheel carbon steel. The test pins for Case-2 had a specific wear rate at a level of 10^{-5} mm3/Nm, which was about one ten power lower than for the other two discs.

8.6 FUTURE RECOMMENDATIONS:

As described in the literature and with the experiments presented in this thesis, LC has excellent potential to replace many standard surface engineering technologies. Primarily there is great potential in applying this technology in the areas that need immediate solutions, such as reducing NE from automobiles. The following investigations could be useful for future research.

Multilayer deposition could be monitored via a closed-loop control system, and an efficient temperature-measuring device could be implemented since geometric distortions are the main hindrance in implementing LC for AM. This data could help understand the melt pool behaviour and control such distortions more effectively. MMCs should be deposited to study the effectiveness of volume control fractions.

Empirical statistical models for LC are primarily system and material-dependent. More research is needed to expand the materials used to create such models. This could serve as a data base to validate the computational models. As presented in this study, these models are recommended to be based on multi-track depositions. Nonetheless, the importance of models obtained via single tracks cannot be denied; however, in most real-life cases, many tracks need to be overlapped to cover the whole surface.

Since tool steel contains a tiny fraction of heavy metals and has improved hardness values, further research could focus on using a buffer layer to avoid cracking coatings on GCI brake discs. A combined approach of substrate heating and the application of buffer layers could result in effective coatings.

As seen from the literature, an increased interest currently exists in reducing NE from brake discs of cars. As in this work, the emission from brake disc / Cu free pad varied by varying test conditions. Therefore,

these test conditions could be used for future studies to create wear and emission maps. The tool steel cladded discs could be tested for PM 2.5 emissions. Since the use of LC overlays for reducing ultra-fine PM emissions from rail-wheel contact is studied first time (to the best of the author's knowledge as of January 2023) as presented in this thesis, more research is necessary to understand this phenomenon fully. The particle concentration for the measured size range was close to the sensitivity limit of the instrument used. Therefore, an instrument with a lower sensitivity limit should be used for future studies. The test conditions should be varied in future studies to understand the emission response of such particles. This includes the simulation of contact conditions that are most common in subway environments. These particles could be further analysed for their harmfulness. An actual time-temperature measuring device could provide valuable results in describing the wear regimes in such contact.

APPENDIX 1 – RAPID CODE FOR FABRICATION OF THIN WALL VIA LC - BIDIRECTIONAL SCAN STRATEGY

```
MODULE Wall_BidirectionalScanStrategy
!*** Author: Nashit Ali ***
LOCAL VAR num velocity;
LOCAL VAR speeddata vel;
LOCAL VAR num user_selection := 0;
LOCAL VAR robtarget vertex1;
LOCAL VAR robtarget vertex2;
LOCAL VAR robtarget P1;
LOCAL VAR robtarget P2;
LOCAL VAR robtarget P3;
LOCAL VAR robtarget P4;
LOCAL VAR num deltaZ;
LOCAL VAR num length;
LOCAL VAR num increment;
LOCAL VAR num Nlayer;
LOCAL VAR num NtotLayers;
LOCAL VAR num HatchDistance;
LOCAL VAR num NtotPasses;
LOCAL VAR num Npasses;
LOCAL VAR num halfpasses;
LOCAL VAR num halfLayers;

PROC Wall_BidirectionalScanStrategy()
ActUnit STN1;
TPErase;
TPReadNum NtotLayers,"Total number of layers";
TPErase;
TPReadNum length,"length wall in mm";
TPErase;
TPReadNum deltaZ,"deltaZ mm";
TPErase;
TPReadNum NtotPasses,"Number of Passes";
TPErase;
TPReadNum HatchDistance,"Hatch Distance mm";
TPErase;
TPReadNum velocity,"Velocity of process [mm/s]";
vel:=[velocity,500,5000,1000];
TPErase;
TPReadFK user_selection, "Choose as starting position", "", "", "", "", "Current Position";
IF user_selection = 5 THEN
vertex1 := CRobT (\Tool:=toolCladding_16_11_2020\WObj:=wobjTavola_OLD16_11_2020);
ELSE
TPWrite "Invalid selection. Terminating the programme...";
WaitTime PRINT_TIME;
EXIT;
stop;
ENDIF
vertex2:= Offs(vertex1,length,0.0,0.0);
MoveL vertex1,vel,fine,toolCladding_16_11_2020\WObj:=wobjTavola_OLD16_11_2020;
LaserInit 3;
```

```
Waittime 1;
StartGasCopertura;
SetVelRotSelettore1(5.0);
StartSelettore1;
Waittime 10.0;
halfLayers:= Round(NtotLayers/2) + 1;
halfpasses:= Round(NtotPasses/2);
Nlayer:=0;
Npasses:=0;
FOR i FROM 1 TO halfLayers DO
first_layer:
Npasses:=0;
Nlayer:= Nlayer + 1;
IF Nlayer <= NtotLayers THEN
FOR id1 FROM 1 TO halfpasses DO
Npasses:=Npasses+1;
IF Npasses <= NtotPasses THEN
increment:= deltaZ * (Nlayer - 1);
P1:=Offs(vertex1, 0.0, HatchDistance*(Npasses-1),increment);
MoveL P1,vel,fine,toolCladding_16_11_2020\WObj:=wobjTavola_OLD16_11_2020;
LaserStart;
P2:=Offs(P1, length, 0.0,0.0);
MoveL P2,vel,fine,toolCladding_16_11_2020\WObj:=wobjTavola_OLD16_11_2020;
LaserStop;
ELSE GOTO second_layer;
ENDIF
Npasses:=Npasses+1;
IF Npasses <= NtotPasses THEN
P3:=Offs(P2, 0.0, HatchDistance,0.0);
MoveL P3,vel,fine,toolCladding_16_11_2020\WObj:=wobjTavola_OLD16_11_2020;
LaserStart;
P4:=Offs(P3, -length, 0.0,0.0);
MoveL P4,vel,fine,toolCladding_16_11_2020\WObj:=wobjTavola_OLD16_11_2020;
LaserStop;
ELSE GOTO second_layer;
ENDIF
ENDFOR
ELSE GOTO finisci;
ENDIF
second_layer:
Npasses:=0;
Nlayer:= Nlayer + 1;
IF Nlayer <= NtotLayers THEN
FOR id2 FROM 1 TO halfpasses DO
Npasses:=Npasses+1;
IF Npasses <= NtotPasses THEN
increment:= deltaZ * (Nlayer - 1);
P1:=Offs(vertex2, 0.0, HatchDistance*(Npasses-1),increment);
MoveL P1,vel,fine,toolCladding_16_11_2020\WObj:=wobjTavola_OLD16_11_2020;
LaserStart;
P2:=Offs(P1, -length, 0.0,0.0);
MoveL P2,vel,fine,toolCladding_16_11_2020\WObj:=wobjTavola_OLD16_11_2020;
LaserStop;
ELSE GOTO first_layer;
ENDIF
Npasses:=Npasses+1;
```

```
IF Npasses <= NtotPasses THEN
P3:=Offs(P2, 0.0, HatchDistance,0.0);
MoveL P3,vel,fine,toolCladding_16_11_2020\WObj:=wobjTavola_OLD16_11_2020;
LaserStart;
P4:=Offs(P3, length, 0.0,0.0);
MoveL P4,vel,fine,toolCladding_16_11_2020\WObj:=wobjTavola_OLD16_11_2020;
LaserStop;
ELSE GOTO first_layer;
ENDIF
ENDFOR
ELSE GOTO finisci;
ENDIF
ENDFOR
finisci:
LaserDeInit;
StopSelettore1;
StopGasCopertura;
TPWrite "Processing finished";
WaitTime PRINT_TIME;
EXIT;
stop;
ENDPROC
ENDMODULE
```

APPENDIX 2 – RAPID CODE FOR FABRICATION OF THIN WALL VIA LC - UNIDIRECTIONAL SCAN STRATEGY

```
MODULE Wall_UnidirectionalScanStatregy
!*** Author: Nashit Ali ***

LOCAL VAR num Velocity;
LOCAL VAR speeddata vel;
LOCAL VAR num user_selection := 0;
LOCAL VAR robtarget Pinitial;
LOCAL VAR robtarget P1;
LOCAL VAR robtarget P2;
LOCAL VAR robtarget P3;
LOCAL VAR robtarget P4;
LOCAL VAR num deltaZ;
LOCAL VAR num length;
LOCAL VAR num increment;
LOCAL VAR num Nlayer;
LOCAL VAR num NtotLayers;
LOCAL VAR num halflayers;

PROC Wall_UnidirectionalScanStatregy ()
ActUnit STN1;
TPErase;
TPReadNum NtotLayers,"total number of layers";
TPErase;
TPReadNum length,"length wall in mm";
TPErase;
TPReadNum deltaZ,"deltaZ mm";
TPErase;
TPReadNum Velocity,"velocity of process [mm/s]";
vel:=[Velocity,500,5000,1000];
TPErase;
TPReadFK user_selection, "choose as starting position ", "", "", "", "", "current position";
IF user_selection = 5 THEN
Pinitial := CRobT (\Tool:=toolCladding_16_11_2020\WObj:=wobjTavola_OLD16_11_2020);
ELSE
TPWrite "Invalid selection. Terminating the programme...";
WaitTime PRINT_TIME;
EXIT;
stop;
ENDIF
MoveL Pinitial,vel,fine,toolCladding_16_11_2020\WObj:=wobjTavola_OLD16_11_2020;
LaserInit 3;
Waittime 1;
StartGasCopertura;
SetVelRotSelettore1(5.0);
StartSelettore1;
Waittime 10.0;
halflayers:= Round(NtotLayers/2);
Nlayer:=0;
FOR i FROM 1 TO halflayers DO
Nlayer:= Nlayer + 1;
```

```
IF Nlayer <=NtotLayers THEN
increment:= deltaZ * (Nlayer - 1);
P1:=Offs(Pinitial, 0.0, 0.0,increment);
MoveL P1,vel,fine,toolCladding_16_11_2020\WObj:=wobjTavola_OLD16_11_2020;
LaserStart;
SetDO Fascio_Cladding_ON,1;
P2:=Offs(P1, length, 0.0,0.0);
MoveL P2,vel,fine,toolCladding_16_11_2020\WObj:=wobjTavola_OLD16_11_2020;
LaserStop;
ELSE GOTO finisci;
ENDIF
Nlayer:= Nlayer + 1;
IF Nlayer <=NtotLayers THEN
P3:=Offs(P2, 0.0, 0.0,deltaZ);
MoveL P3,vel,fine,toolCladding_16_11_2020\WObj:=wobjTavola_OLD16_11_2020;
LaserStart;
P4:=Offs(P3, -length, 0.0,0.0);
MoveL P4,vel,fine,toolCladding_16_11_2020\WObj:=wobjTavola_OLD16_11_2020;
LaserStop;
ELSE GOTO finisci;
ENDIF
ENDFOR
finisci:
LaserDeInit;
StopSelettore1;
StopGasCopertura;
TPWrite "Lavorazione terminata";
WaitTime PRINT_TIME;
stop;
ENDPROC
ENDMODULE
```

APPENDIX 3 – RAPID CODE FOR LC OF ALUMNIUM BRONZE

```
MODULE Cladding_Tube
!*** Author: Nashit Ali ***
LOCAL VAR num proc_speed;
LOCAL VAR speeddata speed;
LOCAL VAR num user_choice := 0;
LOCAL VAR robtarget Pinitial:=[[-67.78,8.57,125.92],[0.411293,-0.667377,-0.525886,0.329984],[0,0,0,0],[9E+09,-89.9863,-16816.5,9E+09,9E+09,9E+09]];
LOCAL VAR robtarget P1;
LOCAL VAR num shift;
LOCAL VAR num Power;
LOCAL VAR num HatchDistance;
LOCAL VAR num Ntracks;
LOCAL VAR NUM TracksCounter;
LOCAL VAR extjoint ext_axes_offset;

PROC Tube_Helix_Cladding_Tests()
ActUnit STN1;
ext_axes_offset:=[9E+09,0,0,9E+09,9E+09,9E+09];
TracksCounter:=0;
TPErase;
TPReadNum proc_speed,"Processing Speed [mm/s]";
speed:=[proc_speed,500,5000,1000];
TPErase;
TPReadNum Power,"Power [W]";
setPotenza(Power);
TPErase;
TPReadNum HatchDistance,"Hatch Distance [mm]";
TPErase;
TPReadNum NTracks,"Number of Tracks";
TPErase;
TPReadFK user_choice, "SET POWDER FEED RATE HOPPER No 2 !", "", "", "", "", "DONE!";
IF user_choice = 4  THEN
waittime 1;
ENDIF
MoveJ Pinitial, v200, fine, toolCladding_new\WObj:=WObjTavola;
laserinit 1;
Waittime 1;
StartGasCopertura;
StartSelettore2;
Waittime 15.0;
laserStart_Cladding;
FOR i FROM 1 TO Ntracks DO
TracksCounter:=TracksCounter+1;
shift:=HatchDistance*(TracksCounter);
P1:= Offs(Pinitial,0,0,-shift);
ext_axes_offset.eax_c:=ext_axes_offset.eax_c-360;
EOffsSet ext_axes_offset;
MoveJ P1,speed,z1,toolCladding_new\WObj:=wobjTavola;
ENDFOR
laserStop;
laserDeInit;
StopSelettore2;
```

```
StopGasCopertura;
TPWrite "PROCESSING FINISHED";
WaitTime PRINT_TIME;
stop;
ENDPROC
ENDMODULE
```

APPENDIX 4 – RAPID CODE FOR LC OF TOOL STEEL ON BRAKE DISC

```
!*** Author: Nashit Ali ***
MODULE Cladding_Discs
LOCAL VAR num proc_speed;
LOCAL VAR speeddata speed;
LOCAL VAR num user_choice := 0;
LOCAL VAR robtarget Pinitial:=[[-0.04,146.19,144.10],[0.0122067,-0.00750709,0.999863,0.00825432],[0,-
1,0,0],[9E+09,0.00280351,-0.00178562,9E+09,9E+09,9E+09]];
LOCAL VAR robtarget P1;
LOCAL VAR num shift;
LOCAL VAR num Power;
LOCAL VAR num rpm;
LOCAL VAR num HatchDistance;
LOCAL VAR num Ntracks;
LOCAL VAR NUM TracksCounter;
LOCAL VAR num NLayers;
LOCAL VAR extjoint ext_axes_offset;

PROC Disc_Cladding()

ActUnit STN1;
ext_axes_offset:=[9E+09,0,0,9E+09,9E+09,9E+09];
TracksCounter:=0;
TPErase;
TPReadNum proc_speed,"Processing Speed [mm/s]";
speed:=[proc_speed,500,5000,1000];
TPErase;
TPReadNum Power,"Power [W]";
setPotenza(Power);
TPErase;
TPReadNum rpm,"Set powder feeder RPM";
setVelRotSelettore1(rpm);
TPErase;
TPReadNum HatchDistance,"Hatch Distance [mm]";
TPErase;
TPReadNum NTracks,"Number of Tracks";
TPErase;
TPReadNum NLayers,"Number of Layers";
TPErase;
TPReadFK user_choice, "SET POWDER FEED RATE HOPPER No 1 !", "", "", "", "", "DONE!";
IF user_choice = 4  THEN
waittime 1;
ENDIF
MoveJ Pinitial, speed, fine, toolCladding_16_11_2020\WObj:=wobjTavola_OLD16_11_2020;
laserinit 4;
Waittime 1;
setVelRotSelettore1(5.0);
StartGasCopertura;
StartSelettore1;
Waittime 5.0;
FOR j FROM 1 to NLayers DO
TracksCounter:=0;
ext_axes_offset.eax_c:=ext_axes_offset.eax_c-360;
```

```
EOffsSet ext_axes_offset;
MoveJ Pinitial,speed,z1,toolCladding_16_11_2020\WObj:=wobjTavola_OLD16_11_2020;
laserStart;
FOR i FROM 1 TO Ntracks DO
TracksCounter:=TracksCounter+1;
shift:=HatchDistance*(TracksCounter);
P1:= Offs(Pinitial,0,-shift,0);
pPoseTrans.rot:=OrientZYX(360,0,0);
ext_axes_offset.eax_c:=ext_axes_offset.eax_c-360;
EOffsSet ext_axes_offset;
MoveJ P1,speed,z1,toolCladding_16_11_2020\WObj:=wobjTavola_OLD16_11_2020;
ENDFOR
laserStop;
ENDFOR
laserDeInit;
StopSelettore1;
StopGasCopertura;
TPWrite "PROCESSING FINISHED";
WaitTime PRINT_TIME;
stop;
ENDPROC
ENDMODULE
```

REFERENCES

1. Chateauminois, A. ASM Handbook: Surface Engineering (Vol 5). *Tribology International - TRIBOL INT* **2000**, *33*, 67, DOI 10.1016/S0301-679X(00)00006-2.

2. Tucker, R.C. Surface Engineering. *Thermal Spray Technology* **2013**, 10, DOI 10.31399/asm.hb.v05a.a0005707.

3. Kandeva, M.; Vencl, A.; Karastoyanov, D. *Advanced Tribological Coatings for Heavy-Duty Applications: Case Studies,* 2016;.

4. Rickerby, D.S.; Matthews, A. *Advanced Surface Coatings: A Handbook of Surface Engineering,* Blackie: 1991;.

5. Quintino, L. 1 - Overview of coating technologies. In *Surface modification by solid state processing*Elsevier Ltd: 2014; pp. 1-24.

6. Davis, J.R. Introduction to Surface Engineering for Corrosion and Wear Resistance. In *Surface Engineering for Corrosion and Wear Resistance*Maney Publishing: 2001; pp. 1-2.

7. Mishra, R.S.; Ma, Z.Y. Friction stir welding and processing. *Materials Science and Engineering: R: Reports* **2005**, *50*, 1-78, DOI 10.1016/j.mser.2005.07.001. Available online: https://www.sciencedirect.com/science/article/pii/S0927796X05000768 (accessed on Nov 1, 2022).

8. Qian, M.; Lim, L.C.; Chen, Z.D.; Chen, W.I. Parametric studies of laser cladding processes. *Journal of Materials Processing Technology* **1997**, *63*, 590-593, DOI 10.1016/S0924-0136(96)02689-1. Available online: https://www.sciencedirect.com/science/article/pii/S0924013696026891 (accessed on Nov 1, 2022).

9. Davis, J.R. Hardfacing, weld cladding, and dissimilar metal joining. *ASM International, ASM Handbook.* **1993**, *6*, 789-829.

10. Zhu, L.; Xue, P.; Lan, Q.; Meng, G.; Ren, Y.; Yang, Z.; Xu, P.; Liu, Z. Recent research and development status of laser cladding: A review. *Optics & Laser Technology* **2021**, *138*, 106915, DOI 10.1016/j.optlastec.2021.106915. Available online: https://www.sciencedirect.com/science/article/pii/S0030399221000037 (accessed on Nov 1, 2022).

11. Sylvester Bolokang, A.; Ntsoaki Mathabathe, M. Chapter 11 - Laser cladding—a modern joining technique. In *Advanced Welding and Deforming*Elsevier Inc: 2021; pp. 291-319.

12. Li, M.; Han, B.; Song, L.; He, Q. Enhanced surface layers by laser cladding and ion sulfurization processing towards improved wear-resistance and self-lubrication performances. *Applied Surface Science* **2020**, *503*, 144226, DOI 10.1016/j.apsusc.2019.144226. Available online: https://www.sciencedirect.com/science/article/pii/S0169433219330429 (accessed on Oct 31, 2022).

13. Liu, C.; Li, C.; Zhang, Z.; Sun, S.; Zeng, M.; Wang, F.; Guo, Y.; Wang, J. Modeling of thermal behavior and microstructure evolution during laser cladding of AlSi10Mg alloys. *Optics & Laser Technology* **2020**, *123*, 105926, DOI 10.1016/j.optlastec.2019.105926. Available online: https://www.sciencedirect.com/science/article/pii/S0030399219302634 (accessed on Oct 31, 2022).

14. Navas, C.; Conde, A.; Fernández, B.J.; Zubiri, F.; de Damborenea, J. Laser coatings to improve wear resistance of mould steel. *Surface and Coatings Technology* **2005**, *194*, 136-142, DOI 10.1016/j.surfcoat.2004.05.002. Available online: https://www.sciencedirect.com/science/article/pii/S0257897204003378 (accessed on Oct 31, 2022).

15. Huang, S.W.; Samandi, M.; Brandt, M. Abrasive wear performance and microstructure of laser clad WC/Ni layers. *Wear* **2004**, *256*, 1095-1105, DOI 10.1016/S0043-1648(03)00526-X. Available online: https://www.sciencedirect.com/science/article/pii/S004316480300526X (accessed on Oct 31, 2022).

16. Grigoratos, T.; Martini, G. Brake wear particle emissions: a review. *Environ Sci Pollut Res* **2014**, *22*, 2491, DOI 10.1007/s11356-014-3696-8.

17. Bessagnet, B.; Allemand, N.; Putaud, J.; Couvidat, F.; André, J.; Simpson, D.; Pisoni, E.; Murphy, B.N.; Thunis, P. Emissions of Carbonaceous Particulate Matter and Ultrafine Particles from Vehicles—A Scientific Review in a Cross-Cutting Context of Air Pollution and Climate Change. *Applied Sciences* **2022**, *12*, DOI 10.3390/app12073623.

18. Reif, K. *Brakes, Brake Control and Driver Assistance Systems: Function, Regulation and Components,* Springer Fachmedien Wiesbaden: 2014;.

19. Hu, B. Friction and Wear of Automotive and Aircraft Brakes. **2017**, DOI 10.31399/asm.hb.v18.a0006374. Available online: https://dl.asminternational.org/handbooks/edited-volume/50/chapter/619009/Friction-and-Wear-of-Automotive-and-Aircraft (accessed on Nov 1, 2022).

20. Aranke, O.; Algenaid, W.; Awe, S.; Joshi, S. Coatings for Automotive Gray Cast Iron Brake Discs: A Review. *Coatings* **2019**, *9*, DOI 10.3390/coatings9090552.

21. Wahlström, J., Towards a simulation methodology for prediction of airborne wear particles from disc brakes. 2009.

22. Moreno, T.; Martins, V.; Reche, C.; Minguillón, M.C.; de Miguel, E.; Querol, X. Chapter 13 - Air Quality in Subway Systems. In *Non-Exhaust Emissions*; Amato, F., Ed.; Academic Press: 2018; pp. 289-321.

23. Zhou, Y.; Wang, H.; Bi, H.; Wang, J. Experimental and numerical study of aerodynamic pressures on platform screen doors at the overtaking station of a high-speed subway. *Build Environ* **2021**, *191*, 107582, DOI 10.1016/j.buildenv.2020.107582. Available online: https://www.sciencedirect.com/science/article/pii/S0360132320309495

24. Moreno, T.; Martins, V.; Querol, X.; Jones, T.; BéruBé, K.; Minguillón, M.C.; Amato, F.; Capdevila, M.; de Miguel, E.; Centelles, S.; Gibbons, W. A new look at inhalable metalliferous airborne particles on rail subway platforms. *Sci Total Environ* **2015**, *505*, 367-375, DOI 10.1016/j.scitotenv.2014.10.013. Available online: https://www.sciencedirect.com/science/article/pii/S004896971401451X

25. Vanherle, K.; Lopez-Aparicio, S.; Grythe, H.; Lükewille, A.; Uterstaller, A.; Mayeres, I. Transport Non-exhaust PM-emissions. An overview of emission estimates, relevance, trends and policies. **2021**, DOI 10.13140/rg.2.2.25720.98562. Available online: https://search.datacite.org/works/10.13140/rg.2.2.25720.98562

26. Alimardani, M.; Fallah, V.; Khajepour, A.; Toyserkani, E. The effect of localized dynamic surface preheating in laser cladding of Stellite 1. *Surface & coatings technology* **2010**, *204*, 3911-3919, DOI 10.1016/j.surfcoat.2010.05.009. Available online: https://dx.doi.org/10.1016/j.surfcoat.2010.05.009

27. KELL, J.; TYRER, J.R.; HIGGINSON, R.L.; THOMSON, R.C. Microstructural characterization of autogenous laser welds on 316L stainless steel using EBSD and EDS. *Journal of microscopy (Oxford)* **2005**, *217*, 167-173, DOI 10.1111/j.1365-2818.2005.01447.x. Available online: https://onlinelibrary.wiley.com/doi/abs/10.1111/j.1365-2818.2005.01447.x

28. Wang, H.; Liu, W.; Tang, Z.; Wang, Y.; Mei, X.; Saleheen, K.M.; Wang, Z.; Zhang, H. Review on adaptive control of laser-directed energy deposition. *Optical engineering* **2020**, *59*, 070901, DOI 10.1117/1.OE.59.7.070901. Available online: http://www.dx.doi.org/10.1117/1.OE.59.7.070901

29. de Oliveira, U.; Ocelík, V.; De Hosson, J.T.M. Analysis of coaxial laser cladding processing conditions. *Surface & coatings technology* **2005**, *197*, 127-136, DOI 10.1016/j.surfcoat.2004.06.029. Available online: https://dx.doi.org/10.1016/j.surfcoat.2004.06.029

30. Doležel, I.; Kotlan, V.; Hamar, R.; Slobodník, K. Modelling the Laser Cladding of Geometrically More Complex Tracks and Its Experimental Verification. *Metals* **2021**, *11*, DOI 10.3390/met11091403.

31. Ansari, M.; Shoja Razavi, R.; Barekat, M. An empirical-statistical model for coaxial laser cladding of NiCrAlY powder on Inconel 738 superalloy. *Optics and laser technology* **2016**, *86*, 136-144, DOI 10.1016/j.optlastec.2016.06.014. Available online: https://dx.doi.org/10.1016/j.optlastec.2016.06.014

32. Seaman, F.U, Gnanamuthu, D. Met Prog. **1975**, *108*.

33. MAIMAN, T.H. Stimulated Optical Radiation in Ruby. *Nature* **1960**, *187*, 493-494, DOI 10.1038/187493a0. Available online: https://doi.org/10.1038/187493a0

34. Ciraud, P. Verfahren und Vorrichtung zur Herstellung beliebiger Gegenstände aus beliebigem schmelzbarem Material. **1973**.

35. Matthews, S.J. Laser fusing of hardfacing alloy powders, Lasers in Materials Processing, , Ohio, USA, 1983; E. A. Metzbower, Ed.; , pp. 138-148.

36. Vaccari, J.N. The laser's edge in metalworking. *American Machinist* .

37. Eboo, G.M.; Lindemanis, A.E. Advances In Laser Cladding Process Technology. *SPIE Proceedings* **1985**, DOI 10.1117/12.946399.

38. Shellabear, M.; Nyrhilä, O. DMLS -DEVELOPMENT HISTORY AND STATE OF THE ART.

39. Toyserkani, E.; Khajepour, A.; Corbin, S.F. *Laser Cladding,* Taylor & Francis: 2004;.

40. Kathuria, Y.P. Laser-cladding process: a study using stationary and scanning CO2 laser beams. *Surface and Coatings Technology* **1997**, *97*, 442, DOI 10.1016/s0257-8972(97)00165-5.

41. Garrido, A.H.; González, R.; Cadenas, M.; Wang, C.; Sadeghi, F. Lasers in Surface Engineering. In *Lasers in Manufacturing*2013; pp. 247-291.

42. Weerasinghe, V.M.; Steen, W.M. Laser Cladding with Pneumatic Powder Delivery. In *Applied Laser Tooling*; Soares, O.D.D.; Perez-Amor, M., Eds.; Springer Netherlands: Dordrecht, 1987; pp. 183-211.

43. Steen, W.M.; Mazumder, J. Basic Laser Optics. In *Laser Material Processing*; Steen, W.M.; Mazumder, J., Eds.; Springer London: London, 2010; pp. 79-130.

44. Brueckner, F.; Riede, M.; Müller, M.; Marquardt, F.; Willner, R.; Seidel, A.; Lopéz, E.; Leyens, C.; Beyer, E. Enhanced manufacturing possibilities using multi-materials in laser metal deposition. *Journal of Laser Applications* **2018**, *30*, DOI 10.2351/1.5040639.

45. Tsukamoto, S. 2 - Developments in CO2 laser welding. *Handbook of Laser Welding Technologies* **2013**, 17-46, DOI https://doi.org/10.1533/9780857098771.1.17

46. Petring, D.; Polzin, R.; Becker, M. Applications. In *High Power Diode Lasers: Technology and Applications*; Bachmann, F.; Loosen, P.; Poprawe, R., Eds.; Springer New York: New York, NY, 2007; pp. 285-533.

47. Santhanakrishnan, S.; Kong, F.; Kovacevic, R. An experimentally based thermo-kinetic hardening model for high power direct diode laser cladding. *Journal of materials processing technology* **2011**, *211*, 1247-1259, DOI 10.1016/j.jmatprotec.2011.02.006. Available online: https://dx.doi.org/10.1016/j.jmatprotec.2011.02.006

48. Dong, L.; Samson, B. *Fiber Lasers: Basics, Technology, and Applications,* CRC Press, Taylor & Francis Group: 2016;.

49. The Brake for Less Fine Dust New Euro 7 Pollution Rules. Available online: https://www.laserline.com/en-int/the-brake-for-less-fine-dust/ (Accessed on 21-04- 2023).

50. Laser Copper Welding with Blue High-Power Diode Laser. Available online: https://www.laserline.com/en-int/laser-welding-copper/ (Accessed on 28/10/ 2022).

51. Nakaaze, T.; Tsukamoto, M.; Sato, Y.; Funada, Y.; Tanigawa, D.; Sengoku, M.; Asano, K.; Higashino, R.; Abe, N. Development of 100W blue direct diode laser system for cladding of copper. *International Congress on Applications of Lasers & Electro-Optics* **2016**, DOI 10.2351/1.5118585.

52. Sengoku, M.; Tsukamoto, M.; Asano, K.; Higashino, R.; Sato, Y.; Funada, Y.; Yoshida, M.; Abe, N. Experimental investigation on temperature distribution of molten pool for copper with blue direct diode laser cladding. *International Congress on Applications of Lasers & Electro-Optics* **2017**, DOI 10.2351/1.5138179.

53. Hara, T.; Sato, Y.; Higashino, R.; Funada, Y.; Ohkubo, T.; Morimoto, K.; Abe, N.; Tsukamoto, M. Pure copper layer formation on pure copper substrate using multi-beam laser cladding system with blue diode lasers. *Appl Phys A* **2020**, *126*, DOI 10.1007/s00339-020-03559-6. Available online: https://link.springer.com/article/10.1007/s00339-020-03559-6

54. Agarwal, P.; Bajpai, L.; Singh, C.P.; Gupta, K.; Davim, J.P. *Manufacturing and Industrial Engineering: Theoretical and Advanced Technologies,* CRC Press: 2021;.

55. Nowotny, S.; Berger, L.; Spatzier, J. 1.18 - Coatings by Laser Cladding. In *Comprehensive Hard Materials*; Sarin, V.K., Ed.; Elsevier: Oxford, 2014; pp. 507-525.

56. Li, Y.; Steen, W.M.; Sharkey, S.J. Laser remelting of plasma-sprayed coatings on nuclear valves. *SPIE Proceedings* **1993**, DOI 10.1117/12.144180.

57. Schneider, M.F. *Laser Cladding with Powder: Effect of Some Machining Parameters on Clad Properties,* 1998;.

58. Powell, J.; Henry, P.S.; Steen, W.M. Laser Cladding with Preplaced Powder: Analysis of Thermal Cycling and Dilution Effects. *Surface engineering* **1988**, *4*, 141-149, DOI 10.1179/sur.1988.4.2.141. Available online: https://www.tandfonline.com/doi/abs/10.1179/sur.1988.4.2.141

59. Yellup, J.M. Laser cladding using the powder blowing technique. *Surface and Coatings Technology* **1995**, *71*, 121, DOI 10.1016/0257-8972(94)01010-g.

60. Dias da Silva, M.; Partes, K.; Seefeld, T.; Vollertsen, F. Comparison of coaxial and off-axis nozzle configurations in one step process laser cladding on aluminum substrate. *Journal of materials processing technology* **2012**, *212*, 2514-2519, DOI 10.1016/j.jmatprotec.2012.06.011. Available online: https://dx.doi.org/10.1016/j.jmatprotec.2012.06.011

61. Kumar, S.P.; Elangovan, S.; Mohanraj, R.; Srihari, B. Critical review of off-axial nozzle and coaxial nozzle for powder metal deposition. *Materials today : proceedings* **2021**, *46*, 8066-8079, DOI 10.1016/j.matpr.2021.03.037. Available online: https://dx.doi.org/10.1016/j.matpr.2021.03.037

62. Guner, A.; Bidare, P.; Jiménez, A.; Dimov, S.; Essa, K. Nozzle Designs in Powder-Based Direct Laser Deposition: A Review. *Int J Precis Eng Manuf* **123456789**, *23*, 1077, DOI 10.1007/s12541-022-00688-1.

63. Fearon, E.; Watkins, K.G. Optimisation of layer height control in direct laser deposition. *International Congress on Applications of Lasers & Electro-Optics* **2004**, *27*, DOI 10.2351/1.5060232.

64. Anandkumar, R.; Almeida, A.; Vilar, R.; Ocelik, V.; De Hosson, J. Th. M. Influence of powder particle injection velocity on the microstructure of Al-12Si/SiC(p) coatings produced by laser cladding. *Surface & coatings technology* **2009**, *204*, 285-290, DOI 10.1016/j.surfcoat.2009.07.025. Available online: https://search.proquest.com/docview/34785787

65. Lin, J.; Steen, W.M. Citation. *Journal of Laser Applications* **1998**, *10*.

66. Hayhurst, P.; Tuominen, J.; Vuoristo, P.; Mäntylä, T. Coaxial laser cladding nozzle for use with a high power diode laser. *International Congress on Applications of Lasers & Electro-Optics* **2002**, DOI 10.2351/1.5065608.

67. Vuoristo, P. 4.10 - Thermal Spray Coating Processes. In *Comprehensive Materials Processing*; Hashmi, S.; Batalha, G.F.; Van Tyne, C.J.; Yilbas, B., Eds.; Elsevier: Oxford, 2014; pp. 229-276.

68. AnonymousResearchers' Work from University of Science and Technology Beijing Focuses on Tissue Engineering (Porous Ti-10mo Alloy Fabricated By Powder Metallurgy for Promoting Bone Regeneration). *Health & Medicine Week* **2019**, 1701.

69. Liu, H.; Hao, J.B.; Yu, G.; Yang, H.F.; Wang, L.W.; Han, Z.T. A Numerical Study on Metallic Powder Flow in Coaxial Laser Cladding. *JAFM* **2016**, *9*, 2247, DOI 10.18869/acadpub.jafm.68.236.25632.

70. Liu, S.; Zhang, Y.; Kovacevic, R. Numerical Simulation and Experimental Study of Powder Flow Distribution in High Power Direct Diode Laser Cladding Process. *Lasers Manuf Mater Process* **2015**, *2*, 199-218, DOI 10.1007/s40516-015-0015-2. Available online: https://link.springer.com/article/10.1007/s40516-015-0015-2

71. PELLETIER, J.M.; SAHOUR, M.C.; PILLOZ, M.; VANNES, A.B. Influence of processing conditions on geometrical features of laser claddings obtained by powder injection. *Journal of materials science* **1993**, *28*, 5184-5188, DOI 10.1007/BF00570061.

72. Boussaha, E.H.; Aouici, S.; Aouici, H.; Bahloul, A. Study of Powder Particle Size Effect on Microstructural and Geometrical Features of Laser Claddings Using Response Surface Methodology RSM. *Acta Universitatis Sapientiae. Electrical and Mechanical Engineering* **2019**, *11*, 99-116, DOI 10.2478/auseme-2019-0009. Available online: http://www.degruyter.com/doi/10.2478/auseme-2019-0009

73. Kong, Y.; Liu, W.J.; Wang, Y.C. Numerical Simulation of Temperature Field of Direct Laser Metal Deposition Shaping Process of Titanium Alloys. *Advanced materials research* **2011**, *295-297*, 2112-2119, DOI 10.4028/www.scientific.net/AMR.295-297.2112

74. Liu, C.; Lin, J. Thermal processes of a powder particle in coaxial laser cladding. *Optics & Laser Technology* **2003**, *35*, 81, DOI 10.1016/s0030-3992(02)00145-7.

75. Pekkarinen, J.; Salminen, A.; Kujanpää, V.; Ilonen, J.; Lensu, L.; Kälviäinen, H. Powder cloud behavior in laser cladding using scanning optics. *Journal of laser applications* **2016**, *28*, 32007-1, DOI 10.2351/1.4947598. Available online: http://dx.doi.org/10.2351/1.4947598

76. Arrizubieta, J.I.; Tabernero, I.; Ruiz, J.E.; Lamikiz, A.; Martinez, S.; Ukar, E. Continuous Coaxial Nozzle Design for LMD based on Numerical Simulation. *Physics Procedia* **2014**, *56*, 429, DOI 10.1016/j.phpro.2014.08.146.

77. Carroll, P.A.; Pinkerton, A.J.; Allen, J.; Syed, W.U.H.; Sezer, H.K.; Brown, P.; Ng, G.; Scudamore, R.; Li, L. The effect of powder recycling in direct metal laser deposition on powder and manufactured part characteristics. *Cost Effective Manufacture via Net-Shape Processing* **2006**.

78. Renderos, M.; Girot, F.; Lamikiz, A.; Torregaray, A.; Saintier, N. Ni Based Powder Reconditioning and Reuse for LMD Process. *Physics Procedia* **2016**, *83*, 769, DOI 10.1016/j.phpro.2016.08.079.

79. Tobar, M.J.; Amado, J.M.; Montero, J.; Yáñez, A. A Study on the Effects of the Use of Gas or Water Atomized AISI 316L Steel Powder on the Corrosion Resistance of Laser Deposited Material. *Physics Procedia* **2016**, *83*, 606, DOI 10.1016/j.phpro.2016.08.063.

80. Anderson, I.E.; White, E.M.H.; Dehoff, R. Feedstock powder processing research needs for additive manufacturing development. *Current Opinion in Solid State and Materials Science* **2018**, *22*, 8, DOI 10.1016/j.cossms.2018.01.002.

81. Hoeges, S.; Zwiren, A.; Schade, C. Additive manufacturing using water atomized steel powders. *Metal powder report* **2017**, *72*, 111-117, DOI 10.1016/j.mprp.2017.01.004. Available online: https://dx.doi.org/10.1016/j.mprp.2017.01.004

82. Nagy, A.; Kugler, S.; Kreisz, I.; Czitrovszky, A. Characterization of nanoparticle emission during laser cladding with stainless steel powder, IEEE: Nov 02, 2020; , pp. 1.

83. Noskov, A.; El-Khoury, M.; Drobyshev, S.; Kuchaev, E.; Yanbaev, F.; Zhigalina, O.; Khmelenin, D.; Gilmutdinov, A. A microscopy study of nanoparticles emitted during laser additive manufacturing with stainless steel powder. *Materials Letters: X* **2022**, *14*, DOI 10.1016/j.mlblux.2022.100139.

84. Hinse-Stern, A., Burchards, D. & Mordike, B. L. Laser cladding with preheated wires, Proceedings of the European Conference on Laser Treatment of Materials, , Göttingen, Germany,(ECLAT 1992); , pp. 223-228.

85. Moures, F.; Cicală, E.; Sallamand, P.; Grevey, D.; Vannes, B.; Ignat, S. Optimisation of refractory coatings realised with cored wire addition using a high-power diode laser. *Surface and Coatings Technology* **2005**, *200*, 2283, DOI 10.1016/j.surfcoat.2004.10.135.

86. Ding, D.; Pan, Z.; Cuiuri, D.; Li, H. Wire-feed additive manufacturing of metal components: technologies, developments and future interests. *Int J Adv Manuf Technol* **2015**, *81*, 465-481, DOI

10.1007/s00170-015-7077-3. Available online: https://link.springer.com/article/10.1007/s00170-015-7077-3

87. Syed, W.U.H.; Li, L. Effects of wire feeding direction and location in multiple layer diode laser direct metal deposition. *Applied surface science* **2005**, *248*, 518-524, DOI 10.1016/j.apsusc.2005.03.039. Available online: https://dx.doi.org/10.1016/j.apsusc.2005.03.039

88. Tuominen, J.; Kaubisch, M.; Thieme, S.; Näkki, J.; Nowotny, S.; Vuoristo, P. Laser strip cladding for large area metal deposition. *Additive Manufacturing* **2019**, *27*, 208, DOI 10.1016/j.addma.2019.01.008

89. Yelistratov, A. Direct Diode Laser Deposition with Strip Feeding. *Welding design & fabrication* **2006**, *79*, 38 Available online: https://search.proquest.com/docview/29235966

90. Advanced Materials & Processes Technology Information Analysis Center (U.S.) Laser Cladding Refurbishes Navy Ship Components

91. Bambach, M.; Sizova, I.; Silze, F.; Schnick, M. Comparison of laser metal deposition of Inconel 718 from powder, hot and cold wire. *Procedia CIRP* **2018**, *74*, 206, DOI 10.1016/j.procir.2018.08.095

92. Chen, J.; Zhang, Y. Gas Tungsten Arc Welding Using an Arcing Wire. **2017**

93. Bouaifi, B. and Bartzsch, J. Surface protection by laser beam deposition with hot wire addition, Welding and Cutting. **1993**, E70-E72

94. Hinse-Stern, A., Burchards, D. and Mordike, B. L Laser cladding with preheated wires, European Conference on Laser Treatment of Materials, European Conference on Laser Treatment of Materials, ; B.L.Mordike, Ed.; (ECLAT92); , pp. 223-228

95. Wu, T.; Shi, W.; Xie, L.; Gong, M.; Huang, J.; Xie, Y.; He, K. Effect of Preheating Temperature on Geometry and Mechanical Properties of Laser Cladding-Based Stellite 6/WC Coating. *Materials* **2022**, *15*, DOI 10.3390/ma15113952

96. Sadhu, A.; Choudhary, A.; Sarkar, S.; Nair, A.M.; Nayak, P.; Pawar, S.D.; Muvvala, G.; Pal, S.K.; Nath, A.K. A study on the influence of substrate pre-heating on mitigation of cracks in direct metal laser deposition of NiCrSiBC-60%WC ceramic coating on Inconel 718. *Surface & coatings technology* **2020**, *389*, 125646, DOI 10.1016/j.surfcoat.2020.125646. Available online: https://dx.doi.org/10.1016/j.surfcoat.2020.125646

97. Dai, Q.; Luo, C.; You, F. Crack Restraining Methods and their Effects on the Microstructures and Properties of Laser Cladded WC/Fe Coatings. *Materials* **2018**, *11*, DOI 10.3390/ma11122541.

98. Brunner-Schwer, C.; Kersting, R.; Graf, B.; Rethmeier, M. Laser-plasma-cladding as a hybrid metal deposition-technology applying a SLM-produced copper plasma nozzle. *Procedia CIRP* **2018**, *74*, 738, DOI 10.1016/j.procir.2018.08.020

99. Nowotny, S.T.; Scharek, S.; Naumann, T.; Zieris, R.; Beyer, E. Laser based hybrid techniques for surface coating. *International Congress on Applications of Lasers & Electro-Optics* **2002**, DOI 10.2351/1.5066178

100. Suutala, J.; Tuominen, J.; Vuoristo, P. Laser-assisted spraying and laser treatment of thermally sprayed coatings. *Surface & coatings technology* **2006**, *201*, 1981-1987, DOI 10.1016/j.surfcoat.2006.04.042. Available online: https://dx.doi.org/10.1016/j.surfcoat.2006.04.042

101. Lisiecki, A.; Ślizak, D. Hybrid Laser Deposition of Composite WC-Ni Layers with Forced Local Cryogenic Cooling. *Materials* **2021**, *14*, DOI 10.3390/ma14154312

102. Kubisch, F.; Nowotny, S.; Leyens, C.; Beyer, E.; Techel, A. COAXID – omni-directional inner diameter laser cladding optic. *International Congress on Applications of Lasers & Electro-Optics* **2011**, DOI 10.2351/1.5062318

103. Weisheit, A.; Gasser, A.; Backes, G.; Jambor, T.; Pirch, N.; Wissenbach, K. Direct Laser Cladding , Current Status and Future Scope of Application. *Laser-Assisted Fabrication of Materials* **2012**, *161*, 221, DOI 10.1007/978-3-642-28359-8_5

104. Schopphoven, T.; Gasser, A.; Backes, G. EHLA: Extreme High-Speed Laser Material Deposition. *Laser-Technik-Journal* **2017**, *14*, 26-29, DOI 10.1002/latj.201700020. Available online: https://onlinelibrary.wiley.com/doi/abs/10.1002/latj.201700020

105. Yuan, W.; Li, R.; Chen, Z.; Gu, J.; Tian, Y. A comparative study on microstructure and properties of traditional laser cladding and high-speed laser cladding of Ni45 alloy coatings. *Surface & coatings technology* **2021**, *405*, 126582, DOI 10.1016/j.surfcoat.2020.126582. Available online: https://dx.doi.org/10.1016/j.surfcoat.2020.126582

106. Li, T.; Zhang, L.; Bultel, G.G.P.; Schopphoven, T.; Gasser, A.; Schleifenbaum, J.H.; Poprawe, R. Extreme High-Speed Laser Material Deposition (EHLA) of AISI 4340 Steel. *Coatings (Basel)* **2019**, *9*, 778, DOI 10.3390/coatings9120778. Available online: https://search.proquest.com/docview/2548356908

107. Stephan, K.; Holzer, A.; Megahed, S.; Ziegler, S.; Schleifenbaum, J.H.; Schmitz, K. Investigation of the coating of hydrodynamic plain bearing contact surfaces by means of Extreme High-Speed Laser Material Deposition (EHLA). *IOP conference series. Materials Science and Engineering* **2021**, *1097*, 12016,

DOI 10.1088/1757-899X/1097/1/012016. Available online: https://search.proquest.com/docview/2512943317

108. Li, L.; Shen, F.; Zhou, Y.; Tao, W. Comparative study of stainless steel AISI 431 coatings prepared by extreme-high-speed and conventional laser cladding. *Journal of laser applications* **2019**, *31*, 42009, DOI 10.2351/1.5094378. Available online: http://dx.doi.org/10.2351/1.5094378

109. Shen, F.; Tao, W.; Li, L.; Zhou, Y.; Wang, W.; Wang, S. Effect of microstructure on the corrosion resistance of coatings by extreme high speed laser cladding. *Appl Surf Sci* **2020**, *517*, 146085, DOI 10.1016/j.apsusc.2020.146085. Available online: https://www.sciencedirect.com/science/article/pii/S0169433220308412

110. Schopphoven, T.; Pirch, N.; Mann, S.; Poprawe, R.; Häfner, C.L.; Schleifenbaum, J.H. Statistical/Numerical Model of the Powder-Gas Jet for Extreme High-Speed Laser Material Deposition. *Coatings* **2020**, *10*, 416, DOI 10.3390/coatings10040416. Available online: https://search.proquest.com/docview/2395045977

111. Li, T.; Zhang, L.; Chen, G.; Pirch, N.; Schopphoven, T.; Gasser, A.; Poprawe, R. A combined heat source model for the prediction of residual stress post extreme high-speed laser material deposition. *Journal of manufacturing processes* **2022**, *78*, 265-277, DOI 10.1016/j.jmapro.2022.03.055. Available online: https://dx.doi.org/10.1016/j.jmapro.2022.03.055

112. Holzer, A.; Koss, S.; Schleifenbaum, J.H.; Schmitz, K. Extreme High-Speed Laser Material Application-Coated Carbide-Reinforced Control Plates and Conventional Lead-Based Plates in Axial Piston Machines. *Chem Eng & Technol* **2022**, *46*, 110, DOI 10.1002/ceat.202200402

113. Holzer, A.; Koß, S.; Ziegler, S.; Schleifenbaum, J.H.; Schmitz, K. Extreme High-Speed Laser Material Deposition (EHLA) as High-Potential Coating Method for Tribological Contacts in Hydraulic Applications, Enhanced Material, Parts Optimization and Process, , Intensification; Reisgen, U., Drummer, D. and Marschall, H., Eds.; Springer International Publishing: Cham, 2021; , pp. 153-167

114. Schaible, J.; Sayk, L.; Schopphoven, T.; Schleifenbaum, J.H.; Häfner, C. Development of a high-speed laser material deposition process for additive manufacturing. *Journal of Laser Applications* **2021**, *33*, DOI 10.2351/7.0000320

115. What is Extreme High Speed Laser Application (EHLA). Available online: https://www.twi-global.com/technical-knowledge/faqs/what-is-ehla (Accessed on 19/12/ 2022)

116. Preheating of substrate for DED and laser cladding processes. Available online: https://www.cenos-platform.com/post/preheating-of-substrate-for-ded-and-laser-cladding-processes (Accessed on 19/12/ 2022)

117. Trends in the Laser Cladding Technology - part 2. Available online: https://www.linkedin.com/pulse/trends-laser-cladding-technology-part-2-arkadi-zikin/ (Accessed on 26/12/ 2022)

118. Lalas, C.; Tsirbas, K.; Salonitis, K.; Chryssolouris, G. An analytical model of the laser clad geometry. *International journal of advanced manufacturing technology* **2007**, *32*, 34-41, DOI 10.1007/s00170-005-0318-0. Available online: https://search.proquest.com/docview/2262506699

119. Pinkerton, A.J.; Li, L. Multiple-layer cladding of stainless steel using a high-powered diode laser: an experimental investigation of the process characteristics and material properties. *Thin solid films* **2004**, *453-454*, 471-476, DOI 10.1016/j.tsf.2003.11.140. Available online: https://dx.doi.org/10.1016/j.tsf.2003.11.140

120. Ali, N.; Tomesani, L.; Ascari, A.; Fortunato, A. Fabrication of Thin Walls with and without Close Loop Control as a Function of Scan Strategy Via Direct Energy Deposition. *Lasers Manuf Mater Process* **2022**, *9*, 81, DOI 10.1007/s40516-022-00164-8

121. Thompson, S.M.; Bian, L.; Shamsaei, N.; Yadollahi, A. An overview of Direct Laser Deposition for additive manufacturing; Part I: Transport phenomena, modeling and diagnostics. *Additive manufacturing* **2015**, *8*, 36-62, DOI 10.1016/j.addma.2015.07.001. Available online: https://dx.doi.org/10.1016/j.addma.2015.07.001

122. Wang, L.; Felicelli, S. Process Modeling in Laser Deposition of Multilayer SS410 Steel. , DOI 10.1115/1.2738962

123. Han, L.; Liou, F.W. Numerical investigation of the influence of laser beam mode on melt pool. *International journal of heat and mass transfer* **2004**, *47*, 4385-4402, DOI 10.1016/j.ijheatmasstransfer.2004.04.036. Available online: https://dx.doi.org/10.1016/j.ijheatmasstransfer.2004.04.036

124. HOADLEY, A.F.A.; RAPPAZ, M. A Thermal Model of Laser Cladding by Powder Injection. *Metallurgical Transactions B* **1992**, *23*, 631-642, DOI 10.1007/BF02649723. Available online: https://search.proquest.com/docview/25908533

125. Sun, S.; Durandet, Y.; Brandt, M. Correlation between melt pool temperature and clad formation in pulsed and continuous wave Nd:YAG laser cladding of stellite 6. *Pacific International Conference on Applications of Lasers and Optics* **2004**, *11*, DOI 10.2351/1.5056117

126. Srivastava, D.; Chang, I.T.H.; Loretto, M.H. The optimisation of processing parameters and characterisation of microstructure of direct laser fabricated TiAl alloy components. *Materials & Design* **2000**, *21*, 425, DOI 10.1016/s0261-3069(99)00091-6

127. Pinkerton, A.J. 16 - Laser direct metal deposition: theory and applications in manufacturing and maintenance. In *Advances in laser materials processing*Elsevier Ltd: 2010; pp. 461-491

128. Resch, M.; Kaplan, A.F.H.; Schuoecker, D. Laser-assisted generating of three-dimensional parts by the blown powder process. *SPIE Proceedings* **2001**, DOI 10.1117/12.413998

129. Tsipenyuk, Y.M. *PHYSICAL METHODS, INSTRUMENTS AND MEASUREMENTS – Volume IV,* EOLSS Publications: 2009;

130. Hofineisterl, W.H.; Maccahm2, D.O.; Knorovsky, G.A.; Feceiveb 59AX25?7" W%b c VIDEO MONITORING AND CONTROL OF THE LENS PROCESS

131. Beuth, J.L.; Asme, M.; Griffith, M. Aditad Vasinonta Graduate Student Process Maps for Predicting Residual Stress and Melt Pool Size in the Laser-Based Fabrication of Thin-Walled Structures. , DOI 10.1115/1.2335852

132. Beuth, J.; Klingbeil, N. The role of process variables in laser-based direct metal solid freeform fabrication. *JOM* **2001**, *53*, 36-39, DOI 10.1007/s11837-001-0067-y. Available online: https://doi.org/10.1007/s11837-001-0067-y

133. Riveiro, A.; Mejías, A.; Lusquiños, F.; Del Val, J.; Comesaña, R.; Pardo, J.; Pou, J. Optimization of Laser Cladding for Al Coating Production. *Physics Procedia* **2013**, *41*, 327, DOI 10.1016/j.phpro.2013.03.085

134. Zanzarin, S.; Bengtsson, S.; Molinari, A. Study of dilution in laser cladding of a carbon steel substrate with Co alloy powders. *Powder metallurgy* **2016**, *59*, 85-94, DOI 10.1080/00325899.2015.1118842. Available online: https://www.tandfonline.com/doi/abs/10.1080/00325899.2015.1118842

135. Zanzarin Simone, Laser cladding with metallic powder. University of Trento, 2015

136. Zhao, G.; Cho, C.; Kim, J. Application of 3-D finite element method using Lagrangian formulation to dilution control in laser cladding process. *International Journal of Mechanical Sciences* **2003**, *45*, 777, DOI 10.1016/s0020-7403(03)00140-1

137. de Oliveira, U.; Ocelík, V.; De Hosson, J. Th. M. Analysis of coaxial laser cladding processing conditions. *Surface and Coatings Technology* **2005**, *197*, 127-136, DOI https://doi.org/10.1016/j.surfcoat.2004.06.029 Available online: https://www.sciencedirect.com/science/article/pii/S0257897204004803

138. Pacheco, J.T.; da Silva, L.J.; Barbetta, L.D.; Ferreira, H.S.; Veiga, M.T.; Forni, R.; Teixeira, M.F. Laser Cladding of Stellite-6 on AISI 316 L Austenitic Stainless Steel: Empirical-Statistical Modeling and Parameter Optimization. *Lasers in Manufacturing and Materials Processing* **2021**, *8*, 1-14, DOI 10.1007/s40516-020-00132-0 Available online: https://doi.org/10.1007/s40516-020-00132-0

139. , R.O.; Wu, X.; Zhu, B.; Zeng, X.; Hu, X.; Cui, K. HtlI#OLO T Critical state of laser cladding with powder auto-feeding. *Surface and Coatings Technology* **1996**, *79*

140. Davim, J.P.; Oliveira, C.; Cardoso, A. Laser cladding: An experimental study of geometric form and hardness of coating using statistical analysis. *Proceedings of the Institution of Mechanical Engineers. Part B, Journal of engineering manufacture* **2006**, *220*, 1549-1554, DOI 10.1243/09544054JEM641. Available online: https://journals.sagepub.com/doi/full/10.1243/09544054JEM641

141. El Cheikh, H.; Courant, B.; Branchu, S.; Hascoët, J.; Guillén, R. Analysis and prediction of single laser tracks geometrical characteristics in coaxial laser cladding process. *Optics and Lasers in Engineering* **2011**, *50*, 413, DOI 10.1016/j.optlaseng.2011.10.014

142. Sun, Y.; Hao, M. Statistical analysis and optimization of process parameters in Ti6Al4V laser cladding using Nd:YAG laser. *Optics and lasers in engineering* **2012**, *50*, 985-995, DOI 10.1016/j.optlaseng.2012.01.018. Available online: https://dx.doi.org/10.1016/j.optlaseng.2012.01.018

143. Saqib, S.; Urbanic, R.J.; Aggarwal, K. Analysis of Laser Cladding Bead Morphology for Developing Additive Manufacturing Travel Paths. *Procedia CIRP* **2014**, *17*, 824, DOI 10.1016/j.procir.2014.01.098

144. Barekat, M.; Shoja Razavi, R.; Ghasemi, A. Nd:YAG laser cladding of Co–Cr–Mo alloy on γ-TiAl substrate. *Optics and laser technology* **2016**, *80*, 145-152, DOI 10.1016/j.optlastec.2016.01.003 Available online: https://dx.doi.org/10.1016/j.optlastec.2016.01.003

145. Erfanmanesh, M.; Abdollah-Pour, H.; Mohammadian-Semnani, H.; Shoja-Razavi, R. An empirical-statistical model for laser cladding of WC-12Co powder on AISI 321 stainless steel. *Optics and laser*

technology **2017**, *97*, 180-186, DOI 10.1016/j.optlastec.2017.06.026 Available online: https://dx.doi.org/10.1016/j.optlastec.2017.06.026

146. Nabhani, M.; Razavi, R.S.; Barekat, M. An empirical-statistical model for laser cladding of Ti-6Al-4V powder on Ti-6Al-4V substrate. *Optics and laser technology* **2018**, *100*, 265-271, DOI 10.1016/j.optlastec.2017.10.015 Available online: https://dx.doi.org/10.1016/j.optlastec.2017.10.015

147. Bax, B.; Rajput, R.; Kellet, R.; Reisacher, M. Systematic evaluation of process parameter maps for laser cladding and directed energy deposition. *Additive manufacturing* **2018**, *21*, 487-494, DOI 10.1016/j.addma.2018.04.002. Available online: https://dx.doi.org/10.1016/j.addma.2018.04.002

148. Li, Y.; Zhang, P.; Bai, P.; Zhao, Z.; Liu, B. Analysis of Geometrical Characteristics and Properties of Laser Cladding 85 wt.% Ti + 15 wt.% TiBCN Powder on 7075 Aluminum Alloy Substrate. *Materials* **2018**, *11*, DOI 10.3390/ma11091551

149. Aghili, S.E.; Shamanian, M. Investigation of powder fed laser cladding of NiCr-chromium carbides single-tracks on titanium aluminide substrate. *Optics and laser technology* **2019**, *119*, 105652, DOI 10.1016/j.optlastec.2019.105652. Available online: https://dx.doi.org/10.1016/j.optlastec.2019.105652

150. Alizadeh-Sh, M.; Marashi, S.P.H.; Ranjbarnodeh, E.; Shoja-Razavi, R.; Oliveira, J.P. Prediction of solidification cracking by an empirical-statistical analysis for laser cladding of Inconel 718 powder on a non-weldable substrate. *Optics and laser technology* **2020**, *128*, 106244, DOI 10.1016/j.optlastec.2020.106244. Available online: https://dx.doi.org/10.1016/j.optlastec.2020.106244

151. Jelvani, S.; Shoja Razavi, R.; Barekat, M.; Dehnavi, M. Empirical-Statistical Modeling and Prediction of Geometric Characteristics for Laser-Aided Direct Metal Deposition of Inconel 718 Superalloy. *Met Mater Int* **2019**, *26*, 668-681, DOI 10.1007/s12540-019-00355-7. Available online: https://link.springer.com/article/10.1007/s12540-019-00355-7

152. Ali, N.; Ascari, A.; Fortunato, A.; Tomesani, L. An Empirical Statistical Model for Laser Cladding of Aluminium Bronze on S235JR Pipe. *Lasers Manuf Mater Process* **2022**, *9*, 376-391, DOI 10.1007/s40516-022-00184-4. Available online: https://link.springer.com/article/10.1007/s40516-022-00184-4

153. Tuominen, J., Engineering Coatings by Laser Cladding - The Study of Wear and Corrosion Properties. Tampere University of Technology, 2009.

154. Böllinghaus, T.; Herold, H. *Hot Cracking Phenomena in Welds,* Springer Berlin Heidelberg: 2005;.

155. Masubuchi, K.; Hopkins, D.W. *Analysis of Welded Structures: Residual Stresses, Distortion, and Their Consequences,* Elsevier Science: 2013;.

156. Steen, W.M. Laser Surface Cladding. In *Laser Surface Treatment of Metals*; Draper, C.W.; Mazzoldi, P., Eds.; Springer Netherlands: Dordrecht, 1986; pp. 369-387.

157. Ng, G.K.L.; Jarfors, A.E.W.; Bi, G.; Zheng, H.Y. Porosity formation and gas bubble retention in laser metal deposition. *Appl Phys A* **2009**, *97*, 641-649, DOI 10.1007/s00339-009-5266-3. Available online: https://link.springer.com/article/10.1007/s00339-009-5266-3

158. Zeng, C.; Tian, W.; Liao, W.H.; Hua, L. Microstructure and porosity evaluation in laser-cladding deposited Ni-based coatings. *Surface and Coatings Technology* **2016**, *294*, 122-130, DOI https://doi.org/10.1016/j.surfcoat.2016.03.083 Available online: https://www.sciencedirect.com/science/article/pii/S0257897216302134

159. Belmondo, A.; Castagna, M. Wear-resistant coatings by laser processing. *Thin Solid Films* **1979**, *64*, 249-256, DOI https://doi.org/10.1016/0040-6090(79)90517-0. Available online: https://www.sciencedirect.com/science/article/pii/0040609079905170.

160. Tsui, Y.C.; Clyne, T.W. An analytical model for predicting residual stresses in progressively deposited coatings Part 1: Planar geometry. *Thin Solid Films* **1997**, *306*, 23, DOI 10.1016/s0040-6090(97)00199-5.

161. A. F. A. Hoadley, A. Frenk, C. F. Marsden. A Process Overview of Laser Hardfacing. In , 1st ed.Routledge: 1995; pp. 16.

162. Ferreira, M.G.S.; Watkins, K.G.; Steen, W.M.; Vilar, R.; McMahon, M.A.; Green, A. Effect of Residual Stress on the Corrosion Properties of CO2 Laser Surface Melted Alloys. *Materials science forum* **1995**, *192-194*, 789-796, DOI 10.4028/www.scientific.net/MSF.192-194.789 Available online: https://www.scientific.net/MSF.192-194.789

163. AnonymousTemperature field and residual stress distribution for laser metal deposition. **2018**.

164. Köhler, H.; Partes, K.; Kornmeier, J.R.; Vollertsen, F. Residual Stresses in Steel Specimens Induced by Laser Cladding and their Effect on Fatigue Strength. *Physics Procedia* **2012**, *39*, 354, DOI 10.1016/j.phpro.2012.10.048.

165. Anonymous *Corrosion: Understanding the Basics,* 2000: ASM International, 2000; pp. 563.

166. Mcgrann, R.T.R.; Greving, D.J.; Shadley, J.R.; Rybicki, E.F.; Kruecke, T.L.; Bodger, B.E. The effect of coating residual stress on the fatigue life of thermal spray-coated steel and aluminum. *Surface and Coatings Technology* **1998**, *108-109*, 59, DOI 10.1016/s0257-8972(98)00665-3.

167. Kahlen, F.; Kar, A. Tensile Strengths for Laser-Fabricated Parts and Similarity Parameters for Rapid Manufacturing. *J Manuf Sci Eng* **1999**, *123*, 38-44, DOI 10.1115/1.1286472. Available online: https://doi.org/10.1115/1.1286472

168. Kahlen, F.; Kar, A. Residual stresses in laser-deposited metal parts. *International Congress on Applications of Lasers & Electro-Optics* **2001**, *13*, DOI 10.2351/1.5059490.

169. Tuominen, J.; Vuoristo, P.; Mäntylä, T. Residual stresses in HPDL and ND:YAG laser cladded coatings. *International Congress on Applications of Lasers & Electro-Optics* **2005**, DOI 10.2351/1.5060575.

170. Kadolkar, P.B.; Watkins, T.; Dahotre, N. Residual stress characterization of particulate-reinforced composite coating using x-ray diffraction technique. *International Surface Engineering Congress - Proceedings of the 1st Congress* **2003**, 593-602.

171. Tuominen, J.; Näkki, J.; Poutala, J.; Miettinen, J.; Peltola, T.; Vuoristo, P.; Rasehorn, I.; Alam, M.M.; Kaplan, A.F.H. Fatigue behavior of laser clad round steel bars. *Journal of laser applications* **2015**, *27*, 12006, DOI 10.2351/1.4903351. Available online: http://urn.kb.se/resolve?urn=urn:nbn:se:ltu:diva-3912

172. Ding, C.; Cui, X.; Jiao, J.; Zhu, P. Effects of Substrate Preheating Temperatures on the Microstructure, Properties, and Residual Stress of 12CrNi2 Prepared by Laser Cladding Deposition Technique. *Materials* **2018**, *11*, DOI 10.3390/ma11122401.

173. Rangaswamy, P.; Holden, T.M.; Rogge, R.B.; Griffith, M.L. Residual stresses in components formed by the laserengineered net shaping (LENS®) process. *Journal of strain analysis for engineering design* **2003**, *38*, 519-527, DOI 10.1243/030932403770735881. Available online: https://journals.sagepub.com/doi/full/10.1243/030932403770735881

174. Moat, R.J.; Pinkerton, A.J.; Hughes, D.J.; Li, L.; Withers, P.J.; Preuss, M. Stress distributions in multilayer laser deposited Waspaloy parts measured using neutron diffraction. *International Congress on Applications of Lasers & Electro-Optics* **2007**, DOI 10.2351/1.5060984.

175. Doubenskaia, M.; Bertrand, P.; Smurov, I. Optical monitoring of Nd:YAG laser cladding. *Thin solid films* **2004**, *453-454*, 477-485, DOI 10.1016/j.tsf.2003.11.184. Available online: https://dx.doi.org/10.1016/j.tsf.2003.11.184

176. Köhler, H.; Thomy, C.; Vollertsen, F. Contact-less temperature measurement and control with applications to laser cladding. *Weld World* **2016**, *60*, 1-9, DOI 10.1007/s40194-015-0275-7. Available online: https://link.springer.com/article/10.1007/s40194-015-0275-7

177. Thawari, N.; Gullipalli, C.; Chandak, A.; Gupta, T.V.K. Influence of laser cladding parameters on distortion, thermal history and melt pool behaviour in multi-layer deposition of stellite 6: In-situ measurement. *Journal of alloys and compounds* **2021**, *860*, 157894, DOI 10.1016/j.jallcom.2020.157894. Available online: https://dx.doi.org/10.1016/j.jallcom.2020.157894

178. Bi, G.; Gasser, A.; Wissenbach, K.; Drenker, A.; Poprawe, R. Identification and qualification of temperature signal for monitoring and control in laser cladding. *Optics and Lasers in Engineering* **2006**, *44*, 1348, DOI 10.1016/j.optlaseng.2006.01.009.

179. Salehi, D.; Brandt, M. Melt pool temperature control using LabVIEW in Nd:YAG laser blown powder cladding process. *International journal of advanced manufacturing technology* **2006**, *29*, 273-278, DOI 10.1007/s00170-005-2514-3. Available online: https://search.proquest.com/docview/2262523144

180. Pavlov, M.; Novichenko, D.; Doubenskaia, M. Optical Diagnostics of Deposition of Metal Matrix Composites by Laser Cladding. *Physics Procedia* **2011**, *12*, 674, DOI 10.1016/j.phpro.2011.03.084.

181. Lijun Song; Mazumder, J. Feedback Control of Melt Pool Temperature During Laser Cladding Process. *TCST* **2011**, *19*, 1349-1356, DOI 10.1109/TCST.2010.2093901. Available online: https://ieeexplore.ieee.org/document/5675755

182. Smurov, I.; Doubenskaia, M.; Grigoriev, S.; Nazarov, A. Optical Monitoring in Laser Cladding of Ti6Al4V. *J Therm Spray Tech* **2012**, *21*, 1357-1362, DOI 10.1007/s11666-012-9808-4. Available online: https://link.springer.com/article/10.1007/s11666-012-9808-4

183. Hofman, J.T.; Pathiraj, B.; van Dijk, J.; de Lange, D.F.; Meijer, J. A camera based feedback control strategy for the laser cladding process. *Journal of materials processing technology* **2012**, *212*, 2455-2462, DOI 10.1016/j.jmatprotec.2012.06.027. Available online: https://dx.doi.org/10.1016/j.jmatprotec.2012.06.027

184. Colodrón, P.; Fariña, J.; Rodríguez-Andina, J.J.; Vidal, F.; Mato, J.L.; Ángeles Montealegre, M. FPGA-Based Measurement of Melt Pool Size in Laser Cladding Systems.

185. A. Gasser, Oberflächenbehandlung metallischer Werkstoffe mit CO2-Laserstrahlung in der flüssigen Phase. 1993.

186. De Baere, D.; Devesse, W.; De Pauw, B.; Hinderdael, M.; Guillaume, P. Evaluation of the diffuse reflectivity behaviour of the melt pool during the laser metal deposition process. *International Congress on Applications of Lasers & Electro-Optics* **2016**, DOI 10.2351/1.5118584.

187. Wirth, F.; Arpagaus, S.; Wegener, K. Analysis of melt pool dynamics in laser cladding and direct metal deposition by automated high-speed camera image evaluation. *Additive manufacturing* **2018**, *21*, 369-382, DOI 10.1016/j.addma.2018.03.025. Available online: https://dx.doi.org/10.1016/j.addma.2018.03.025

188. Araujol, J.R.; Rodriguez-Andina2, J.J.; Farina2, J.; Vidat, F.; Matol, J.L.; Montealegrel, M.A. FPGA-Based Laser Cladding System with Increased Robustness to Optical Defects.

189. Wang, T.; Chen, J.; Gao, X.; Li, W. Quality Monitoring for Laser Welding Based on High-Speed Photography and Support Vector Machine. *Applied Sciences* **2017**, *7*, DOI 10.3390/app7030299.

190. Asselin, M.; Toyserkani, E.; Iravani-Tabrizipour, M.; Khajepour, A. Development of trinocular CCD-based optical detector for real-time monitoring of laser cladding. *IEEE International Conference Mechatronics and Automation, 2005* **2005**, DOI 10.1109/icma.2005.1626722.

191. Sampson, R.; Lancaster, R.; Sutcliffe, M.; Carswell, D.; Hauser, C.; Barras, J. An improved methodology of melt pool monitoring of direct energy deposition processes. *Optics & Laser Technology* **2020**, *127*, DOI 10.1016/j.optlastec.2020.106194.

192. Prinsloo, F. Tekslinguistiek: van teorie tot praktyk. *Literator* **2017**, *23*, 105, DOI 10.4102/lit.v23i2.333.

193. Fishman, M.; Sherbaum, N.; Zahavi, J. *SPIE Proceedings* **1995**, DOI 10.1117/12.211188.

194. , K.P.; Van, R.C.; , B.H. LASER BASED REFURBISHMENT OF STEEL MILL COMPONENTS.

195. Denney, P.E.; Lowry, R.W. Laser Cladding Refurbishment of Catapult Trough Covers. *Naval engineers journal* **1993**, *105*, 69-75, DOI 10.1111/j.1559-3584.1993.tb02778.x. Available online: https://www.ingentaconnect.com/content/asne/nej/1993/00000105/00000006/art00013

196. Chen, J.; Xue, L. Laser cladding of high-performance CPM tool steels on hardened HI3 hot-work tool steel for automotive tooling applications; Record identifier / Identificateur de l'enregistrement : 9eba2d74-64fa-426c-b054-cfb00327d785. *Supplemental Proceedings: Materials Processing and Interfaces, Volume 1* **2012**, DOI 10.1002/9781118356074.ch2.

197. Torims, T.; Bruckner, F.; Ratkus, A.; Fokejevs, A.; Logins, A. The Application of Laser Cladding to Marine Crankshaft Journal Repair and Renovation. *Volume 1: Applied Mechanics; Automotive Systems;*

Biomedical Biotechnology Engineering; Computational Mechanics; Design; Digital Manufacturing; Education; Marine and Aerospace Applications , DOI 10.1115/esda2014-20001.

198. Torims, T. The application of laser cladding to mechanical component repair, renovation and regeneration. *DAAAM International scientific book* **2013**, 587, DOI 10.2507/daaam.scibook.2013.32.

199. Gorunov, A.I. Complex refurbishment of titanium turbine blades by applying heat-resistant coatings by direct metal deposition. *Engineering failure analysis* **2018**, *86*, 115-130, DOI 10.1016/j.engfailanal.2018.01.001. Available online: https://dx.doi.org/10.1016/j.engfailanal.2018.01.001

200. Chen, C.; Wu, H.C.; Chiang, M.F. Laser cladding in repair of IN738 turbine blades. *International Heat Treatment & Surface Engineering* **2008**, *2*, 140-146, DOI 10.1179/174951508X446484. Available online: https://www.tandfonline.com/doi/abs/10.1179/174951508X446484

201. Meinert, K.C.; Bergan, P. Refurbishment of aluminum alloys by laser cladding. *International Congress on Applications of Lasers & Electro-Optics* **1999**, DOI 10.2351/1.5059284.

202. Aditya, Y.N.; Dharish Srichandra, T.; Tak, M.; Padmanabham, G. To study the laser cladding of ultra high strength AerMet-100 alloy powder on AISI-4340 steel for repair and refurbishment. *Materials today : proceedings* **2021**, *41*, 1146-1155, DOI 10.1016/j.matpr.2020.09.154. Available online: https://dx.doi.org/10.1016/j.matpr.2020.09.154

203. Liu, Q.; Janardhana, M.; Hinton, B.; Brandt, M.; Sharp, K. Laser cladding as a potential repair technology for damaged aircraft components. *International journal of structural integrity* **2011**, *2*, 314-331, DOI 10.1108/17579861111162914. Available online: https://www.emerald.com/insight/content/doi/10.1108/17579861111162914/full/html

204. Thivillon, L.; Bertrand, P.; Laget, B.; Smurov, I. Potential of direct metal deposition technology for manufacturing thick functionally graded coatings and parts for reactors components. *Journal of nuclear materials* **2009**, *385*, 236-241, DOI 10.1016/j.jnucmat.2008.11.023. Available online: https://dx.doi.org/10.1016/j.jnucmat.2008.11.023

205. Wang, S.; Xue, L. Laser cladding of functional coatings for biomedical applications; Record identifier / Identificateur de l'enregistrement : 19bb35e2-e85b-4cf1-9694-b8c573276c25. *TMS Annual Meeting* **2011**, *1*, 569-576.

206. Seo, J.; Kim, J.; Kwon, S.; Jun, H. Effects of Laser Cladding for Repairing and Improving Wear of Rails. *Int J Precis Eng Manuf* **2019**, *20*, 1207-1217, DOI 10.1007/s12541-019-00115-y. Available online: https://link.springer.com/article/10.1007/s12541-019-00115-y

207. Guo, H.; Wang, Q.; Wang, W.; Guo, J.; Liu, Q.; Zhu, M. Investigation on wear and damage performance of laser cladding Co-based alloy on single wheel or rail material. *Wear* **2015**, *328-329*, 329-337, DOI 10.1016/j.wear.2015.03.002. Available online: https://dx.doi.org/10.1016/j.wear.2015.03.002

208. Zhu, Y.; Yang, Y.; Mu, X.; Wang, W.; Yao, Z.; Yang, H. Study on wear and RCF performance of repaired damage railway wheels: Assessing laser cladding to repair local defects on wheels. *Wear* **2019**, *430-431*, 126-136, DOI 10.1016/j.wear.2019.04.028. Available online: https://dx.doi.org/10.1016/j.wear.2019.04.028

209. Clare, A.T.; Oyelola, O.; Abioye, T.E.; Farayibi, P.K. Laser cladding of rail steel with Co-Cr. *Surface engineering* **2013**, *29*, 731-736, DOI 10.1179/1743294412Y.0000000075. Available online: https://www.tandfonline.com/doi/abs/10.1179/1743294412Y.0000000075

210. Wang, W.J.; Hu, J.; Guo, J.; Liu, Q.Y.; Zhu, M.H. Effect of laser cladding on wear and damage behaviors of heavy-haul wheel/rail materials. *Wear* **2014**, *311*, 130-136, DOI 10.1016/j.wear.2014.01.011. Available online: https://dx.doi.org/10.1016/j.wear.2014.01.011

211. Lu, P.; Lewis, S.R.; Fretwell-Smith, S.; Engelberg, D.L.; Fletcher, D.I.; Lewis, R.R. Laser cladding of rail; the effects of depositing material on lower rail grades. *Wear* **2019**, *438-439*, DOI 10.1016/j.wear.2019.203045.

212. Fu, Z.K.; Ding, H.H.; Wang, W.J.; Liu, Q.Y.; Guo, J.; Zhu, M.H. Investigation on microstructure and wear characteristic of laser cladding Fe-based alloy on wheel/rail materials. *Wear* **2015**, *330-331*, 592-599, DOI 10.1016/j.wear.2015.02.053. Available online: https://dx.doi.org/10.1016/j.wear.2015.02.053

213. Lewis, S.R.; Lewis, R.; Fletcher, D.I. Assessment of laser cladding as an option for repairing/enhancing rails. *Wear* **2015**, *330-331*, 581-591, DOI 10.1016/j.wear.2015.02.027. Available online: https://dx.doi.org/10.1016/j.wear.2015.02.027

214. Lewis, S.R.; Fretwell-Smith, S.; Goodwin, P.S.; Smith, L.; Lewis, R.; Aslam, M.; Fletcher, D.I.; Murray, K.; Lambert, R. Improving rail wear and RCF performance using laser cladding. *Wear* **2016**, *366-367*, 268-278, DOI 10.1016/j.wear.2016.05.011. Available online: https://dx.doi.org/10.1016/j.wear.2016.05.011

215. Clare, A.; Oyelola, O.; Folkes, J.; Clare, A.; Oyelola, O.; Folkes, J.; Farayibi, P. Laser cladding. *Journal of Laser Applications* **2012**, *24*.

216. Meng, L.; Zhao, W.; Hou, K.; Kou, D.; Yuan, Z.; Zhang, X.; Xu, J.; Hu, Q.; Wang, D.; Zeng, X. A comparison of microstructure and mechanical properties of laser cladding and laser-induction hybrid cladding coatings on full-scale rail. *Materials Science and Engineering: A* **2019**, *748*, 1-15, DOI 10.1016/j.msea.2019.01.068. Available online: https://www.sciencedirect.com/science/article/pii/S0921509319300978

217. Barbosa, M.; Bischoff, R.; Strauß, W.; Hillig, H.; Nowotny, S.; Leyens, C. Less CO2 and Fine Dust Emissions in Automotive. *PhotonicsViews (Online)* **2020**, *17*, 46-49, DOI 10.1002/phvs.202000031. Available online: https://search.proquest.com/docview/2429632400

218. Olofsson, U.; Lyu, Y.; Åström, A.H.; Wahlström, J.; Dizdar, S.; Nogueira, A.P.G.; Gialanella, S. Laser Cladding Treatment for Refurbishing Disc Brake Rotors: Environmental and Tribological Analysis. *Tribol Lett* **2021**, *69*, DOI 10.1007/s11249-021-01421-1.

219. Maluf, O.; Angeloni, M.; Spinelli, D. Development of materials for automotive disc brakes Friction Stir Welding View project. **2015**.

220. Hamid, M.K.A.; Kaulan, A.M.; Syahrullail, S.; Bakar, A.R.A. Frictional Characteristics under Corroded Brake Discs. *Procedia Engineering* **2013**, *68*, 668-673, DOI 10.1016/j.proeng.2013.12.237. Available online: https://dx.doi.org/10.1016/j.proeng.2013.12.237

221. AnonymousEuropean Commission -Press release Commission proposes new Euro 7 standards to reduce pollutant emissions from vehicles and improve air quality Next Steps. **2022**.

222. Dizdar, S.; Lyu, Y.; Lampa, C.; Olofsson, U. Grey Cast Iron Brake Discs Laser Cladded with Nickel-Tungsten Carbide—Friction, Wear and Airborne Wear Particle Emission. *Atmosphere* **2020**, *11*, 621, DOI 10.3390/atmos11060621. Available online: https://search.proquest.com/docview/2413304786

223. Tonolini, P.; Montesano, L.; Pola, A.; Landriani, E.; Gelfi, M. The effect of laser-cladding on the wear behavior of gray cast iron brake disc. *Procedia Structural Integrity* **2021**, *33*, 1152, DOI 10.1016/j.prostr.2021.10.129.

224. FNC and gas nitriding use in applications where reduced surface friction is a requirement. Available online: https://gearsolutions.com/departments/hot-seat-jack-titus-39/ (Accessed on 21-04- 2023).

225. Kumar, S. Improvement in Wear and Thermal Resistance of Disc Brake Rotors using TiAlN Coating. *International Journal of Science and Research (IJSR)* **2017**, *6*, 366-372, DOI 10.21275/ART20175184.

226. Wank, A.; Schmengler, C.; Krause, A.; Müller-Roden, K.; Wessler, T. Environmentally Friendly Protective Coatings for Brake Disks. *International Thermal Spray Conference* **2022**, DOI 10.31399/asm.cp.itsc2022p0032.

227. HONING & SUPERFINISHING - TECNOLOGY FROM WORLD LEADER . Available online: https://www.nagel.com/ (Accessed on 21-04- 2023).

228. Hard-coated brake discs become a hot topic. Available online: https://www.junker-group.com/header/news/news-detailansicht/news/hard-coated-brake-discs-become-a-hot-topic (Accessed on 21-04- 2023).

229. Fast and effective: Simultaneous coating and mechanical processing with SMaC. Available online: https://www.ilt.fraunhofer.de/en/press/press-releases/2023/4-21-smac-process.html (Accessed on 21-04- 2023).

230. LDF Series - Mobile High Power Diode Laser. Available online: https://www.laserline.com/en-int/ldfseries/ (Accessed on 21-04- 2023).

231. In-Situ Laser Cladding. Available online: https://hardwear.com.au/in-situ-laser-cladding/ (Accessed on 21-04- 2023).

232. AnonymousTRANSLATED USERS MANUAL GTV multi-jet nozzle PN6625 800.6625.

233. AnonymousControl for Laser Additive Manufacturing with Infrared imaging User manual.

234. Olofsson, U.; Olander, L.; Jansson, A. A Study of Airborne Wear Particles Generated From a Sliding Contact. *J Tribol* **2009**, *131*, 044503, DOI 10.1115/1.3176990. Available online: https://doi.org/10.1115/1.3176990 (accessed on 1/9/2023).

235. AnonymousELPI+™ USER MANUAL Ver. 1.12.

236. S. Dizdar New product and use thereof, Patent application, .

237. Pant, P.; Chatterjee, D.; Samanta, S.K.; Nandi, T.; Lohar, A.K. A bottom-up approach to experimentally investigate the deposition of austenitic stainless steel in laser direct metal deposition system. *J Braz Soc Mech Sci Eng* **2020**, *42*, DOI 10.1007/s40430-019-2166-0. Available online: https://link.springer.com/article/10.1007/s40430-019-2166-0

238. Amine, T.; Newkirk, J.W.; Liou, F. An investigation of the effect of direct metal deposition parameters on the characteristics of the deposited layers. *Case Studies in Thermal Engineering* **2014**, *3*, 21, DOI 10.1016/j.csite.2014.02.002.

239. Raghavan, A.; Wei, H.L.; Palmer, T.A.; DebRoy, T. Heat transfer and fluid flow in additive manufacturing. *Journal of laser applications* **2013**, *25*, 52006, DOI 10.2351/1.4817788. Available online: http://dx.doi.org/10.2351/1.4817788

240. Liu, F.Q.; Wei, L.; Shi, S.Q.; Wei, H.L. On the varieties of build features during multi-layer laser directed energy deposition. *Additive manufacturing* **2020**, *36*, 101491, DOI 10.1016/j.addma.2020.101491. Available online: https://dx.doi.org/10.1016/j.addma.2020.101491

241. Saboori, A.; Aversa, A.; Marchese, G.; Biamino, S.; Lombardi, M.; Fino, P. Microstructure and Mechanical Properties of AISI 316L Produced by Directed Energy Deposition-Based Additive Manufacturing: A Review. *Applied Sciences* **2020**, *10*, DOI 10.3390/app10093310.

242. Saboori, A.; Aversa, A.; Bosio, F.; Bassini, E.; Librera, E.; De Chirico, M.; Biamino, S.; Ugues, D.; Fino, P.; Lombardi, M. An investigation on the effect of powder recycling on the microstructure and mechanical properties of AISI 316L produced by Directed Energy Deposition. *Materials Science and Engineering: A* **2019**, *766*, DOI 10.1016/j.msea.2019.138360.

243. El Cheikh, H.; Courant, B.; Branchu, S.; Huang, X.; Hascoët, J.; Guillén, R. Direct Laser Fabrication process with coaxial powder projection of 316L steel. Geometrical characteristics and microstructure characterization of wall structures. *Optics and Lasers in Engineering* **2012**, *50*, 1779, DOI 10.1016/j.optlaseng.2012.07.002.

244. Wang, L.; Felicelli, S.D.; Craig, J.E. ref234-refid. , DOI 10.1115/1.3173952.

245. Pacheco, J.T.; da Silva, L.J.; Barbetta, L.D.; Ferreira, H.S.; Veiga, M.T.; Forni, R.; Teixeira, M.F. Laser Cladding of Stellite-6 on AISI 316 L Austenitic Stainless Steel: Empirical-Statistical Modeling and Parameter Optimization. *Lasers Manuf Mater Process* **2021**, *8*, 1-14, DOI 10.1007/s40516-020-00132-0. Available online: https://link.springer.com/article/10.1007/s40516-020-00132-0

246. Paulo Davim, J.; Oliveira, C.; Cardoso, A. Predicting the geometric form of clad in laser cladding by powder using multiple regression analysis (MRA). *Materials in engineering* **2008**, *29*, 554-557, DOI 10.1016/j.matdes.2007.01.023. Available online: https://dx.doi.org/10.1016/j.matdes.2007.01.023

247. Kumar, S.; Sharma, V.; Choudhary, A.K.S.; Chattopadhyaya, S.; Hloch, S. Determination of layer thickness in direct metal deposition using dimensional analysis. *Int J Adv Manuf Technol* **2013**, *67*, 2681-

2687, DOI 10.1007/s00170-012-4683-1. Available online: https://link.springer.com/article/10.1007/s00170-012-4683-1

248. Colaço, R.; Vilar, R.; Felde, I.; Kálazi, Z.; Réti, T.; Costa, L.; Verő, B. A Simplified Semi-Empirical Method to Select the Processing Parameters for Laser Clad Coatings. *Materials science forum* **2003**, *414-415*, 385-394, DOI 10.4028/www.scientific.net/MSF.414-415.385 Available online: https://www.scientific.net/MSF.414-415.385

249. Bennett, J.L.; Wolff, S.J.; Hyatt, G.; Ehmann, K.; Cao, J. Thermal effect on clad dimension for laser deposited Inconel 718. *Journal of manufacturing processes* **2017**, *28*, 550-557, DOI 10.1016/j.jmapro.2017.04.024. Available online: https://dx.doi.org/10.1016/j.jmapro.2017.04.024

250. Samodurova, M.; Shaburova, N.; Samoilova, O.; Radionova, L.; Zakirov, R.&.; Pashkeev, K.; Myasoedov, V.; Erdakov, I.; Trofimov, E. A Study of Characteristics of Aluminum Bronze Coatings Applied to Steel Using Additive Technologies. *Materials* **2020**, *13*, DOI 10.3390/ma13020461.

251. AnonymousWelding of Cast Irons. *Cast Iron Science and Technology* **2017**, 287, DOI 10.31399/asm.hb.v01a.a0006301.

252. Greenwood, J.A.; Williamson, J.B.P. Contact of Nominally Flat Surfaces. *Proc R Soc Lond A* **1966**, *295*, 300-319, DOI 10.1098/rspa.1966.0242.

253. Olofsson, U. Adhesion and friction modification. *Wheel–Rail Interface Handbook* **2009**, 510, DOI 10.1533/9781845696788.1.510.

254. Harmon, M.; Santa, J.F.; Jaramillo, J.A.; Toro, A.; Beagles, A.; Lewis, R. Evaluation of the coefficient of friction of rail in the field and laboratory using several devices. *Tribology - Materials, Surfaces & Interfaces* **2020**, *14*, 119-129, DOI 10.1080/17515831.2020.1712111. Available online: https://doi.org/10.1080/17515831.2020.1712111

255. Liu, H.; Cha, Y.; Olofsson, U.; Jonsson, L.T.I.; Jönsson, P.G. Effect of the Sliding Velocity on the Size and Amount of Airborne Wear Particles Generated from Dry Sliding Wheel–Rail Contacts. *Tribol Lett* **2016**, *63*, 1-13, DOI 10.1007/s11249-016-0716-5. Available online: https://link.springer.com/article/10.1007/s11249-016-0716-5

256. Lee, H. The effect of water lubricant on reducing the generation of airborne wear particles from wheel–rail contacts under various train velocities. *Tribology international* **2020**, *150*, 106393, DOI 10.1016/j.triboint.2020.106393. Available online: https://dx.doi.org/10.1016/j.triboint.2020.106393

257. Lee, H.; Namgung, H.; Kwon, S. Effect of train velocity on the amount of airborne wear particles generated from wheel–rail contacts. *Wear* **2018**, *414-415*, 296-302, DOI 10.1016/j.wear.2018.08.023. Available online: https://dx.doi.org/10.1016/j.wear.2018.08.023

258. Namgung, H.; Kim, J.; Woo, S.; Park, S.; Kim, M.; Kim, M.; Bae, G.; Park, D.; Kwon, S. Generation of Nanoparticles from Friction between Railway Brake Disks and Pads. *Environ Sci Technol* **2016**, *50*, 3453-3461, DOI 10.1021/acs.est.5b06252. Available online: http://dx.doi.org/10.1021/acs.est.5b06252 http://dx.doi.org/10.1021/acs.est.5b06252